

**UCLA**

**UCLA Electronic Theses and Dissertations**

**Title**

Monitoring Focal Laser Ablation of Prostate Cancer with Interstitial Thermal and Optical Probes

**Permalink**

<https://escholarship.org/uc/item/0sm3k13d>

**Author**

Geoghegan, Rory

**Publication Date**

2019

Peer reviewed|Thesis/dissertation

UNIVERSITY OF CALIFORNIA

Los Angeles

Monitoring Focal Laser Ablation of Prostate Cancer  
with Interstitial Thermal and Optical Probes

A dissertation submitted in partial satisfaction  
of the requirements for the degree  
Doctor of Philosophy in Bioengineering

by

Rory Geoghegan

2019

© Copyright by  
Rory Geoghegan  
2019

# ABSTRACT OF THE DISSERTATION

Monitoring Focal Laser Ablation of Prostate Cancer  
with Interstitial Thermal and Optical Probes

by

Rory Geoghegan

Doctor of Philosophy in Biomedical Engineering

University of California, Los Angeles, 2019

Professor Leonard S. Marks, Co-Chair

Professor Wentai Liu, Co-Chair

Prostate cancer is diagnosed in almost 200,000 men in the U.S. annually. With approximately 30,000 deaths, the mortality to incidence ratio is relatively low in comparison to other common cancers. Moreover, the primary treatment modalities, radical prostatectomy and radiation therapy, are associated with a substantial reduction in quality of life. Consequently, there is a growing interest in focal therapy which aims to treat the target tumor while minimizing damage to surrounding tissue.

Focal laser ablation (FLA) is a form of focal therapy in which a laser fiber is inserted into a target tumor and oncologic control is achieved through thermally induced coagulative necrosis. Many groups have performed FLA using magnetic resonance

imaging (MRI) for laser fiber targeting and real-time feedback. While this approach has shown promise, we contend that the resource intensive nature of MRI will forever preclude widespread adoption of FLA.

This thesis presents a concerted effort to translate FLA from the MRI suite to the urology clinic. To this end we performed a clinical trial using magnetic resonance - ultrasound fusion guidance and interstitial thermal probes for treatment targeting and monitoring respectively. This approach proved to be safe and potentially effective; however, the utility of thermal probes was found to be inherently limited due to the need for empirically derived thermal damage models.

In an effort to provide an improved monitoring modality we developed an interstitial optical monitoring system that directly assesses the state of tissue based on laser-tissue interaction. To correlate the optical signal and the growth of the coagulation zone we created a tissue mimicking phantom which simulates the thermal and optical response of prostatic tissue and facilitates visualization of the coagulation zone on MRI. FLA was performed in the phantom under MRI surveillance with simultaneous interstitial optical monitoring resulting in the development of a real-time feedback algorithm. The algorithm was subsequently tested in ex vivo bovine tissue and was capable of identifying the coagulation border with a mean absolute error of  $0.3\pm 0.1$ mm. Further work is necessary to demonstrate the utility of interstitial optical monitoring in vivo.

The dissertation of Rory Geoghegan is approved.

Shyam Natarajan

Holden H. Wu

Tzung Hsiai

Leonard S. Marks, Committee Co-Chair

Wentai Liu, Committee Co-Chair

University of California, Los Angeles

2019

*Dedicated to all the brilliant minds advancing healthcare for the betterment of mankind*

# Table of Contents

<b>1. Introduction</b>	<b>1</b>
<b>1.1. Overview of Chapters</b>	<b>3</b>
1.1.1. Chapter 2	3
1.1.2. Chapter 3	4
1.1.3. Chapter 4	5
1.1.4. Chapter 5	6
1.1.5. Chapter 6	8
<b>2. Background</b>	<b>10</b>
<b>2.1. Prostate Cancer Management</b>	<b>10</b>
2.1.1. Imaging	10
2.1.2. Biopsy	11
2.1.3. Rational for Focal Therapy	12
<b>2.2. Hyperthermia</b>	<b>14</b>
<b>2.3. Modern Thermal Ablation Modalities</b>	<b>16</b>
2.3.1. High Intensity Focused Ultrasound	16
2.3.2. Radiofrequency Ablation	17
2.3.3. Microwave Ablation	18
2.3.4. Focal Laser Ablation	20
<b>2.4. Thermal Dosimetry</b>	<b>21</b>
2.4.1. Thermography	21
2.4.2. Electrical Probes	23
2.4.3. Fiber-optic Temperature Sensors	24
2.4.4. Radiologic Imaging	27
<b>2.5. Damage Estimation</b>	<b>30</b>
2.5.1. Arrhenius Model	31
2.5.2. Thermal Isoeffect Dose Model	32
2.5.3. Challenges with Traditional Models	33



2.6.	<b>Non-Thermal Feedback Techniques</b> .....	36
2.6.1.	Ultrasound Imaging.....	36
2.6.2.	Elastography .....	39
2.6.3.	Optical Monitoring.....	44
2.7.	<b>Discussion &amp; Conclusions</b> .....	47
<b>3.</b>	<b>Focal Laser Ablation with Interstitial Thermal Probe</b>	
	<b>Monitoring</b> .....	<b>54</b>
3.1.	<b>Introduction</b> .....	54
3.2.	<b>Materials and Methods</b> .....	56
3.2.1.	Treatment Planning.....	57
3.2.2.	Treatment Protocol & Follow-up .....	60
3.3.	<b>Results</b> .....	62
3.4.	<b>Discussion</b> .....	67
3.5.	<b>Retrospective Analysis of Thermal Probe Utility</b> .....	68
3.6.	<b>Conclusion</b> .....	71
<b>4.</b>	<b>Optical Monitoring as a Potential Alternative to Thermal</b>	
	<b>Monitoring</b> .....	<b>73</b>
4.1.	<b>Introduction</b> .....	73
4.2.	<b>Fundamentals of Laser Tissue Interaction</b> .....	75
4.2.1.	Absorption Coefficient .....	76
4.2.2.	Scattering and Reduced Scattering Coefficients.....	77
4.2.3.	Effective Penetration Depth.....	78
4.3.	<b>Laser-Tissue Interaction During FLA</b> .....	78
4.3.1.	Dynamic Optical Properties.....	78
4.3.2.	Hypothesis Generation .....	80
4.4.	<b>Proof of Concept</b> .....	86
4.5.	<b>Conclusion</b> .....	90
<b>5.</b>	<b>A Tissue-Mimicking Prostate Phantom for 980nm Focal Laser</b>	
	<b>Ablation</b> .....	<b>91</b>

<b>5.1. Introduction.....</b>	<b>91</b>
<b>5.2. Methods .....</b>	<b>95</b>
5.2.1. Phantom Construction.....	95
5.2.2. Absorption Coefficient as Function of Naphthol Green B Concentration	97
5.2.3. Method of Measuring the Reduced Scattering Coefficient.....	98
5.2.4. Reduced Scattering Coefficient as a Function of BSA & Intralipid Concentration.....	101
5.2.5. Testing Optimized Phantom .....	102
<b>5.3. Results.....</b>	<b>104</b>
5.3.1. Absorption Coefficient .....	104
5.3.2. Reduced Scattering Coefficient .....	105
5.3.3. Thermal Response .....	109
5.3.4. FLA Induced Coagulation.....	110
<b>5.4. Discussion.....</b>	<b>111</b>
<b>5.5. Conclusion .....</b>	<b>117</b>
<b>6. Development of an Interstitial Optical Monitoring System...119</b>	
<b>6.1. Introduction.....</b>	<b>119</b>
<b>6.2. System Design.....</b>	<b>121</b>
6.2.1. System Requirements .....	121
6.2.2. System Architecture & Optical Probe Design .....	124
6.2.3. FLA Monitoring Software .....	129
<b>6.3. System evaluation: Tissue Mimicking Phantom.....</b>	<b>131</b>
6.3.1. Methods.....	131
6.3.2. Results.....	135
6.3.3. Discussion .....	144
<b>6.4. System Evaluation: Ex Vivo Bovine Muscle .....</b>	<b>150</b>
6.4.1. Methods.....	150
6.4.2. Results.....	153
6.4.3. Discussion .....	158
<b>6.5. Conclusion .....</b>	<b>160</b>
<b>7. Conclusions and Future Directions .....</b>	<b>162</b>

<b>7.1. Summary .....</b>	<b>162</b>
<b>7.2. Conclusions .....</b>	<b>164</b>
7.2.1. Monitoring Focal Laser Ablation with Interstitial Thermal Probes .....	164
7.2.2. Monitoring Focal Laser Ablation with Interstitial Optical Probes .....	166
7.2.3. Impact on Prostate Cancer Management.....	169
<b>7.3. Future work .....</b>	<b>170</b>
7.3.1. Validation Against Histology .....	170
7.3.2. Multi-element Thermal and Optical Probe.....	171
7.3.3. Clinical Implementation.....	172
<b>8. References.....</b>	<b>174</b>

## LIST OF FIGURES

**Figure 1:** The Artemis MRI-US fusion biopsy platform (Eigen, Grass Valley, CA) ..... 12

**Figure 2:** Comparison of MR thermometry and interstitial thermal probe measurement during FLA for the treatment of prostate cancer. Motion artifact is responsible for the noise evident in the MR data [73]. ..... 29

**Figure 3:** CEUS of uterine fibroid before(A), during (B) and after HIFU treatment (C) [150] ..... 38

**Figure 4:** Shear wave elasticity map (Top) and B-mode image (bottom) obtained after creation of a thermal lesion in porcine liver [172]. SWE identifies the lesion as a region of increased stiffness..... 42

**Figure 5:** MR elastograms obtained before (A) and after (B) a 15 W laser application for 2min in porcine liver. The change in stiffness along a profile through the ablation zone (C) [181]..... 44

**Figure 6:** Optical ablation ratio in liver parenchyma (a) and liver metastases (b) before and after RF ablation. Data acquired from 8 patients. Figure adapted from Tanis et al. [187]. ..... 46

**Figure 7:** Key hardware used in MR-US fusion guided FLA: A) Visualase system, B) Nobulus ultrasound system C) Artemis MRI-US fusion system, D) Luxtron Fiber Optic Thermometry system, E) Needle guide ..... 57

**Figure 8:** A) Luxtron system with one of four fluoro optic probes attached. B) Fluoro optic technology - thermal measurement is based on the decay rate of a phosphor element embedded at tip of the probe ..... 57

**Figure 9:** Ablation zone used for treatment planning. Red arrows indicate light emission from the diffuser ..... 58

**Figure 10:** A) MRI derived ROI fused with biopsy data to create patient specific treatment plan. B) Treatment plan showing the requisite laser fiber trajectory ..... 59

**Figure 11:**A) Setup for MR-US fusion guided focal laser ablation. Treatment is monitored with one transrectal thermal probe (i) and up to three transperineally inserted thermal probes (ii-iv). B) Detailed view of transrectal ultrasound probe with needle guide, laser fiber and thermal probe. The laser fiber is housed in dual lumen catheter that flows saline around the fiber to prevent charring. The thermal probe consists of a single Luxtron fluoroptic probe housed in a 15Ga flexi-needle. .... 60

**Figure 12:** A) Illustration depicting the insertion of transperineal thermal probes under US guidance. B) Probe positioning on transverse imaging plane. Note the rectal monitor highlighted in red. C) Rectal monitor location in sagittal imaging plane..... 62

**Figure 13:** A) Temperature recorded by interstitial thermal probes during two consecutive laser activations. Note the laser tip exceeds 60°C while the rectal experiences negligible heating B) Non-perfused zone observed on MRI immediately after FLA. Note the that probe 4 lies on the edge of the ablation zone and the rectal wall remains intact. .... 63

**Figure 14:** Contrast enhanced MRI acquired immediately after receiving FLA. In all 10 patients a distinct zone of non-perfused tissue is observed within the prostate capsule. .... 64

**Figure 15:** Imaging histologic findings in a patient successfully treated with MR-US fusion guided focal laser ablation. The top row shows the MR-visible tumor with positive biopsy cores (Gleason 7) within the ROI. Six months after receiving FLA, no tumor was visible on MRI and biopsy cores identifying coagulative necrosis within the ablation zone and no cancer outside the ablation zone..... 65

<b>Figure 16:</b> Estimated cell death during FLA of a patient based on the Arrhenius model and interstitial thermal probe data (Kinetic parameters: Jacques et al).....	70
<b>Figure 17:</b> Optimal exposure duration for select laser activations (Kinetic parameters: Jacques et al) Note: all patients received multiple ablations but the dataset was limited to those in previously untreated tissue. Mean =145.8 standard deviation = 37.2s. ....	70
<b>Figure 18:</b> Comparison of optimal exposure duration estimated using the Arrhenius model with kinetic parameters from the literature.....	71
<b>Figure 19:</b> Laser-tissue interactions [196] .....	76
<b>Figure 20:</b> Absorption coefficient as a function of wavelength for typical chromophores in tissue[196] .....	77
<b>Figure 21:</b> Mie and Rayleigh scattering .....	78
<b>Figure 22:</b> Thought experiment with ballistic optical sensor .....	84
<b>Figure 23:</b> Thought experiment with backscatter optical sensor .....	85
<b>Figure 24:</b> Experimental setup - 1) Ex vivo bovine muscle sample holder with laser fiber, thermal probe and optical probe, 2) Photodiode, 3) FOT lab kit, 4) Voltage divider, 5) Voltage divider, 6) Microcontroller, 7) Dedicated PC and 8) Custom built software for data visualization and recording .....	87
<b>Figure 25:</b> Temperature and photovoltage during FLA.....	88
<b>Figure 26:</b> Temperature and predicted cell death during FLA .....	89
<b>Figure 27:</b> Ex vivo bovine muscle after FLA treatment. Note the extensive char visible along the length of the laser fiber .....	89
<b>Figure 28:</b> Apparatus used to quantify $\mu_s'$ . Phantoms were cast in 70mm x 70mm x 40mm thin walled (1mm) containers with holes for the source and dosimetry probes.	

During testing the container holding the phantom is placed in the measurement chamber before inserting the probes ..... 99

**Figure 29:** Design of the isotropic point source/detector probes. .... 99

**Figure 30:** 1-Fluence box apparatus, 2 - Amplified photodetector, 3 - voltage divider, 4 - Arduino Leonardo, 5 - PC and 6 - Custom-built software..... 100

**Figure 31:** A) Clinical setup during MR-US fusion guided FLA for the treatment of prostate cancer. FLA was performed in the region of interest (ROI) for 3 min. at 13.75W with a 980nm laser. A thermal probe was used to record temperature. B) Experimental setup mimicking clinical conditions. The phantom was heated to 37°C in a water bath prior to being placed in the insulated box. FLA was performed using the same equipment and configuration used clinically..... 104

**Figure 32:** The effect of photobleaching in Naphthol Green B/water solutions at 980nm. No change was observed as a result of laser exposure ..... 105

**Figure 33:**  $\mu_a$  as function of Naphthol Green B concentration at 980nm in polyacrylamide gel.  $\mu_a$  was determined by a spectrophotometer at 24, 48 and 72 hours. No further bleaching was observed after 48 hours. By interpolation (dashed black line), a 0.144% concentration of Naphthol Green B was found to provide the desired  $\mu_a$  of 0.66cm<sup>-1</sup>. ..... 105

**Figure 34:** A) Normalized  $\ln(V \cdot r)$  vs r for a single set of phantoms doped with 12.5%, 25% and 37.5% BSA and 0.144% Naphthol Green B. B) The effect of BSA concentration on  $\mu_s'$  before and after coagulation measured in 3 sets of phantoms. Given the desired coagulation-induced change in  $\mu_s'$  of 8.1cm<sup>-1</sup>, the requisite concentration of BSA was found to be 31.4%. Error bars represent one standard deviation and are not visible at all points..... 106

**Figure 35:** A) Normalized  $\ln(V \cdot r)$  vs  $r$  for a single set of phantoms doped with 0%, 5% and 10% Intralipid (IL), 0.144% Naphthol Green B and 31.4% BSA. B) The effect of Intralipid and BSA concentration on  $us'$  before and after coagulation measured in 3 sets of phantoms. By interpolation, the requisite concentration of Intralipid was found to be 8.06%. Error bars represent one standard deviation and are not visible at all points. 107

**Figure 36:** Normalized  $\ln(V \cdot r)$  vs  $r$  for a single optimized phantom before and after coagulation. A total of five phantoms were tested and one standard deviation was used to quantify the uncertainty in the measured optical properties shown in Table 10. 108

**Figure 37:** Temperature at a radial distance of 8mm from the laser as measured in a patient and three phantoms. 109

**Figure 38:** Absolute temperature ( $^{\circ}\text{C}$ ) during FLA of the optimized phantom as determined by MRT at 0 (A), 90 (B) and 180 (C) seconds after laser activation. The location of the laser fiber (dashed red line) and thermal probe (dashed black line) are marked. 110

**Figure 39:** A) Zone of coagulative necrosis in a patient as indicated by non-perfused tissue. The scan was acquired immediately after the patient received FLA for 3 min. at 13.75W. Further information can be found in Natarajan et al (2017)1. B) Phantom coagulation zone under T2-weighted MRI showing major and minor axes (white arrows). Note that the catheters in the center and on the right contain the laser fiber and thermal probe respectively. C) Phantom coagulation zone under direct visualization showing major and minor axes (white arrows). Note the needle tracks in the center and to the right. 111

**Figure 40:** A - Components of the optical monitoring system: 1) Interstitial optical probe, 2) Photodiode, 3) Voltage divider, 4) Microcontroller, 5) Computer and 6) Custom built



software. B - Detailed view of interstitial optical probe with a defined cone of acceptance. C - Detailed view of tip of interstitial probe with spherical acceptance. D - Detailed view of tip of interstitial probe with radial acceptance. .... 128

**Figure 41:** Custom built FLA monitoring software..... 129

**Figure 42:** Feedback algorithm - A 2nd order polynomial is fit to the most recent 10s of data and the instantaneous rate of change ( $m$ ) at the most recent data point is quantified. We hypothesize that a steady state ( $m=0$ ) indicates complete coagulation of all tissue between the probe and the laser fiber..... 131

**Figure 43:** A) Clinical setup during FLA. B) Experimental setup designed to match clinical conditions with an optical probe used instead a thermal probe..... 132

**Figure 44:** Detailed view of the testing rig with one wall rendered transparent to highlight the location of the water fiducials. Note that there are 2 fiducials as each phantom is used for two tests; one in the top section and one in the bottom section. An O-ring and thumb screws are used to seal the lid in place to minimize heat loss to the surroundings. Thumb screws are also used to secure the optical probes in place. .... 134

**Figure 45:** A) Block diagram of experimental setup using MRI to monitor laser ablation in the tissue mimicking phantom. B) Photograph of testing rig (inset) on the scanner table prior to placement at isocenter..... 135

**Figure 46:** A) Transverse image acquired by the MRI localizer. The cross-sections of the fiducials are clearly visible (red arrows). Note that there are two sets of fiducials as each phantom is used for two tests. In this case the test is being performed in the top section of the phantom where the dual lumen catheter (black arrow) and optical probes are visible. B) PRE scan used to confirm alignment. The fiducials (red arrows), dual lumen

catheter (black arrow) and one optical probe can be seen. The second optical probe is not in the imaging plane. .... 136

**Figure 47:** Photovoltage recorded using ‘Ballistic’ optical probe placed at 5mm for the laser fiber and corresponding MR images. The orange line in the MR images is the coagulation boundary derived using the edge detection algorithm. The green line denotes the location of the laser fiber..... 137

**Figure 48:** Coagulation radius as a function of time as determined by the edge detection algorithm using both the CINE and POST scan data. .... 141

**Figure 49:** Normalized photovoltage and instantaneous rate of change (slope) as a function of coagulation radius for each interstitial optical probe. Arrows identify the signal plateau/inflection point for each probe..... 143

**Figure 50:** Comparison of the feedback algorithm coagulation radius and the true coagulation radius derived from the MRI data. .... 144

**Figure 51:** Ex vivo bovine tissue sample holder. The image on the right is orientated in the direction of the black arrow and the top section of the sample holder is rendered transparent..... 150

**Figure 52:** A) Cold tissue sample in tissue holder. B) Sample holder in testing rig after being preheated to 37°C. C) Sample holder with top section ..... 152

**Figure 53:** A: Setup for acquiring photograph of sample ablation zone. To ensure consistent lighting a professional lightbox was used. B) Sample image showing ruler which will be used to scale the acquired photograph. Photographs used for analysis were taken with greater magnification..... 152

**Figure 54:** Photovoltage recorded during FLA experiments in ex vivo bovine muscle (Top row), photographs of the ablation zone after FLA (middle row) and profile lines used to

determine the coagulation radius (bottom row). Note that 'r' indicates the distance between the probe and the laser fiber. For r=5, fat obscures the left edge and is seen as signal spike on the profile line (yellow star). In this case the radius is measured from the center of the dual lumen catheter. .... 155

**Figure 55:** Comparison of the measured damage radius (from analysis of the ablation zone) against the target damage radius (position of the probe relative to the laser fiber). Error bars signify one standard deviation. Mean absolute error =  $0.3 \pm 0.1$  ..... 156

**Figure 56:** Laser (980nm) exposure duration at 13.75W required to achieve predefined coagulation radii in ex vivo bovine muscle, tissue mimicking phantom and in vivo human prostate. \*P<0.01 (Wilcoxon rank-sum) ..... 157

**Figure 57:** Proposed multi-element dual thermal and optical interstitial probe..... 172

## LIST OF TABLES

<b>Table 1:</b> Kinetic Parameters and Percentage Surviving Cells after 4 Minutes Exposure at 55°C .....	35
<b>Table 2:</b> Methods for monitoring ablation based on temperature measurement including current clinical application and limitations of each method .....	49
<b>Table 3:</b> Methods for monitoring ablation that do not require temperature measurement including current clinical application and primary limitations of each method.....	52
<b>Table 4:</b> Summary of clinical trial patient characteristics. No serious adverse events were reported. ....	65
<b>Table 5:</b> Comparison of key metrics between UCLA’s MR-guided and US-MR fusion guided clinical trials.....	66
<b>Table 6:</b> Kinetic parameters used in modelling thermally induced coagulative necrosis in the prostate .....	69
<b>Table 7:</b> Optical Properties of Prostatic Tissue in the Native and Coagulated State.....	80
<b>Table 8:</b> Phantom recipe prior to altering optical properties (1L).....	97
<b>Table 9:</b> Tissue-mimicking phantom recipe (1L).....	108
<b>Table 10:</b> Optical properties of tissue-mimicking phantom .....	108
<b>Table 11:</b> Tissue mimicking prostate phantom vs ex vivo tissue .....	117
<b>Table 12:</b> MRI Sequence Parameters .....	134
<b>Table 13:</b> Absolute error (mean $\pm$ one standard deviation) for each optical probe .....	144

## LIST OF ABBREVIATIONS

CaP	Prostate Cancer
ARFI	Acoustic Radiation Force Impulse
BSA	Bovine Serum Albumin
CEUS	Contrast Enhanced Ultrasound
CT	Computed Tomography
DTS	Distributed Temperature Sensing
FBG	Fiber Bragg Grating
FLA	Focal Laser Ablation
GUI	Graphical User Interface
IL	Intralipid
mpMRI	Multi-Parametric Magnetic Resonance Imaging
MRE	Magnetic Resonance Elastography
MRI	Magnetic Resonance Imaging
MRT	Magnetic Resonance Thermometry
MR-US	Magnetic Resonance - Ultrasound
PET	Positron Emission Tomography
PSA	Prostate Specific Antigen
ROI	Region of Interest
SNR	Signal-to-Noise Ratio
SSI	Supersonic Shear Imaging
SWEI	Shear Wave Elasticity Imaging
TCM	Tissue Change Monitoring
TDM	Time-Division Multiplexing
TE	Time to Echo
TID	Thermal Isoeffect Dose
TR	Time to Repeat
TRUS	Transrectal Ultrasound
US	Ultrasound
VA	Vibroacoustography
WDM	Wavelength-Division Multiplexing

## ACKNOWLEDGMENTS

My success can be attributed to the generous support provided by my advisors, thank you, Drs. Warren Grundfest, Leonard Marks and Shyam Natarajan. This work only materialized due to your constant guidance, encouragement and support. You were all open and receptive to my ideas and for that I am grateful. I wish also to thank my other committee members, Drs. Holden Wu, Tzung Hsiai and Wentai Liu for your insight and helpful feedback. In particular, I would like to extend my appreciation to Dr Liu for agreeing to join under difficult circumstances.

I wish also to extend my deepest thanks to my colleagues and collaborators who helped to bring this work to fruition, Drs. Alan Priester, Alvaro Santamaria and Le Zhang. Your contributions to this work ensured its success and I am deeply grateful for your help.

Thank you to all of my labmates who helped me to thrive in the CASIT dungeon, Ashkan, Ahmad, Meg, Zach, Jim, York, Neha, Shijun, Will, Nathan, Harrison and Jake.

A special thanks to Jessica for her unwavering support throughout this convoluted journey. You were always there to celebrate the good days and provide motivation and insight on the many, many days when frustration and failure threatened to lead me astray. I will be forever in your debt.

Lastly, I would like thank my family who remained supportive throughout, despite initial incredulity that I would sacrifice my fledgling career for a minimum wage student position on the far side of the world.

Funding for this work was provided by the National Institutes of Health (NIH) under award number 1R01CA158627-1 and Jean Perkins Foundation. Supporting industry partners included Hitachi Aloka Medical Ltd. and Medtronic Plc.

## VITA

2010	<b>B.E. Mechanical Engineering</b> University College Dublin
2011	<b>M.Sc. Biomedical Engineering</b> Imperial College London
2011-2014	<b>Orthopaedic Implant Design Engineer</b> Stanmore Implants Worldwide (Stryker)
2018	<b>M.S. Bioengineering</b> University of California, Los Angeles
2014-present	<b>Graduate Student Researcher</b> Center for Advanced Surgical & Interventional Technology University of California, Los Angeles

## PUBLICATIONS & PRESENTATIONS

**Geoghegan R**, Santamaria A, Priester A, Zhang L, Wu H, Grundfest W, Marks L, Natarajan S. A Tissue-Mimicking Prostate Phantom for 980nm Laser Interstitial Thermal Therapy. *International Journal of Hyperthermia*, 2019 (In press)

**Geoghegan R**, Song J, Singh A, Le T, Abiri A, Mendelsohn A. Development of a Transoral Robotic Surgery Training Platform. 2019 41st Annual International Conference of the IEEE Engineering in Medicine and Biology Society (EMBC). IEEE, 2019. (In press)

**Geoghegan R**, Priester A, Zhang L, Wu H, Grundfest W, Marks L, Natarajan S. An optical monitoring system for laser interstitial thermal therapy in the treatment of prostate cancer. (In progress)

**Geoghegan R**, Grundfest W, Marks L, Natarajan S. Thermal Ablation in Cancer Treatment: A Review of Feedback and Planning Techniques (In progress)

**Geoghegan R**, Natarajan S, Priester A, Marks L, Grundfest W. Optical Device, System and Method of Monitoring Thermal Therapy in Soft Tissue. PCT/US19/42291; PCT Application, 2019

**Geoghegan R**, Mendelsohn A. Training Platform and Method for Transoral Robotic Surgery. US# 62/687,979; Provisional Application, 2018

Elkhoury F, Natarajan S, Priester A, Jones T, **Geoghegan R**, Delfin M, Felker E, Sisk A, Raman S, Pantuck A, Grundfest W, Marks L. MRI-Guided Biopsy Following Focal Laser Ablation of Prostate Cancer: Subsequent outcomes of 2 clinical Trials. J Urol, 199 (4), e375, 2018

**Geoghegan R**, Priester A, Santamaria A, et al., An Optical Monitoring System for Laser Interstitial Thermal Therapy. 40th International Conference of the IEEE Engineering in Medicine & Biology Conference (2018)

**Geoghegan R**, Priester A, Santamaria A, et al., Development of a Tissue Mimicking Phantom for Laser Ablation. Proc. of the 26th Annual Meeting of ISMRM, Paris, France (2018)

**Geoghegan R**, Natarajan S, Priester A, Marks L, Grundfest W. A Phantom Tissue and Method of Making Thereof. US# 62/686,192; Provisional Application, 2018.

Natarajan S, Jones T, Priester A, **Geoghegan R**, Lieu P, Delfin M, Felker E, Margolis D, Sisk A, Pantuck A, Grundfest W, Marks L. Focal Laser Ablation of Prostate Cancer: Feasibility of Magnetic Resonance Imaging-Ultrasound Fusion for Guidance. J Urol, 198 (4), 839-847, 2017

Natarajan S, Priester AM, **Geoghegan R**, Garritano J, Marks L, Grundfest W. System for out-of-bore focal laser therapy. US# 62/287,105; Provisional Application, 2016.

Natarajan S, Priester A, **Geoghegan R**, Lieu P, Macairan ML, Margolis D, Grundfest W, Pantuck A, Marks L. Initial results of phase I trial of office-based focal laser ablation. American Urological Association; Engineering and Urology Society 2016.

Priester A, **Geoghegan R**, Haber L, Garritano J, Lipiz J, Margolis D, Raman S, Grundfest W, Marks L, Natarajan S. Optimizing damage estimation for prostate thermal therapy. American Urological Association; Engineering and Urology Society 2016

**Geoghegan R**, Priester A, Lieu P, Macairan ML, Pantuck A, Grundfest W, Marks L, Natarajan S. Determining optimal exposure duration for focal laser ablation. American Urological Association; Engineering and Urology Society 2016.

Klufas M, Hubschmann JP, **Geoghegan R**. Surgical Device for Ab-Externo Sub-Retinal Fluid Drainage. US# 62/398,778; Provisional Application, 2016



# CHAPTER 1

## Introduction

Prostate cancer (CaP) is the second most common cancer and the most common in males with an estimated 175,000 new cases and 32,000 deaths in 2019 [1]. The unusual disparity between diagnosis and mortality is clear when compared with the 116,000 new cases and 77,000 deaths associated with the second most common cancer in men, lung and bronchus. This situation has arisen largely due to the widespread adoption of prostate specific antigen (PSA) screening which has resulted in detection of many smaller, lower stage and clinically insignificant cancers. As diagnosis and treatment are tightly coupled, there has been a corresponding trend of overtreatment [2].

Overtreatment of prostate cancer is of particular concern as traditional interventions such as radical prostatectomy and radiation therapy are associated with decreased quality of life due to high rates of incontinence and impotence [3]. Many patients are faced with the decision to elect for either radical intervention or active surveillance and choose the former due to the fear of living with cancer. While radical intervention significantly reduces mortality rates, many patients who choose active surveillance never require intervention [4]. Indeed, much of what is diagnosed as ‘cancer’ is essentially benign as it is insufficiently aggressive to threaten the patient’s life. For example, it has been found that men over 70 years old with favorable risk CaP are 18.6 times more likely to die from a non-CaP related condition [5]. Consequently, there is a need to develop a treatment modality capable of oncologic control without negatively impacting quality of life.

Focal therapy represents a promising minimally invasive treatment for CaP that may prove to be both effective and free from long-term complications such as incontinence and impotence. The goal of focal therapy is to treat only the cancerous tissue while sparing surrounding healthy tissue. It has been demonstrated clinically with technologies such as focal laser ablation (FLA) [6], high intensity focused ultrasound [7] and irreversible electroporation [8]. This thesis focuses on FLA which consists of inserting a laser fiber into the target tumor and inducing hyperthermic conditions sufficient to cause cell death through a process known as coagulative necrosis. FLA has been performed by many groups using magnetic resonance imaging to both guide the laser fiber to the target and monitor the treatment progress via magnetic resonance thermometry (MRT) [6], [9]-[11]. While these studies have shown promising results, we contend that the critical barrier to the adoption of FLA will be the requirement for real-time MRI.

At UCLA we have substantial experience performing targeted biopsies with magnetic resonance - ultrasound (MR-US) fusion guidance. This technique fuses existing MRI data with real-time ultrasound (US) imaging facilitating targeted biopsies in a clinic setting rather than an MRI suite. Given that a biopsy needle can be directed to a target tumor using MR-US fusion guidance, there is little reason to believe that a laser fiber cannot be targeted in the same manner. A greater challenge lies in ensuring both safety and efficacy without using MRT. In this thesis, we describe our efforts to translate FLA from the MRI suite to the clinic with the central hypothesis that interstitial probes can be used to monitor treatment progress in real-time.

## **1.1. Overview of Chapters**

Chapter 2 outlines potential focal therapy modalities and provides an extensive review of methods of monitoring focal therapy. Chapter 3 presents a clinical trial in which FLA was performed using MR-US fusion guidance and interstitial thermal probes for targeting and monitoring respectively. Chapter 4 introduces an alternative method of monitoring FLA based on the underlying principles of laser-tissue interaction. To demonstrate the feasibility of this method a tissue mimicking phantom was developed as outlined in Chapter 5. Finally, the development and evaluation of an interstitial optical monitoring system is described in Chapter 6. A brief summary of each chapter can be found below.

### **1.1.1. Chapter 2**

This chapter begins with a brief introduction to CaP diagnostic methods and outlines the rationale for focal therapy. The second section summarizes the origins, mechanism of action and clinical application of hyperthermia based focal therapy modalities including FLA, microwave ablation MWA, radiofrequency ablation RFA and high intensity focused ultrasound HIFU. The various methods of monitoring these procedures are outlined in the remaining sections. As coagulative necrosis is induced via hyperthermia, the most common feedback modalities rely on thermal dosimetry. Interstitial probes (thermocouples, thermistors, fluoroptic probes, fiber Bragg grating) and radiologic imaging (acoustic thermometry, MRT, and computed tomography (CT) thermometry) represent the most promising approaches to thermal dosimetry. While focal therapy safety may be assured based on raw thermal data, efficacy requires the use of thermal

models to predict the extent of coagulative necrosis. The most commonly used model is the Arrhenius thermal damage model, the application and limitations of which are discussed at length. Finally, alternative techniques that do not rely on thermal dosimetry are discussed. These include advanced ultrasound techniques (contrast enhanced ultrasound and Nakagami imaging), elastography (vibroacoustography, acoustic radiation force impulse imaging, supersonic shear wave imaging, harmonic motion imaging, magnetic resonance elastography) and optical monitoring (diffuse optical spectroscopy, interstitial point optical measurements).

### **1.1.2. Chapter 3**

FLA is performed by many groups using MRI for both targeting and monitoring; however, the direct costs involved will likely limit widespread adoption of this emerging technology. In this chapter we outline a clinic trial undertaken to demonstrate that FLA can be performed safely and effectively using MR-US fusion guidance and interstitial thermal probes for targeting and monitoring respectively. The key aspect of interest in this thesis was the utility of the interstitial thermal probes. 10 men with intermediate risk CaP were recruited and treated with MR-US fusion guided FLA. During the procedure, temperature was monitored with interstitial thermal probes placed at key locations including the laser tip and the rectal wall. The probe at the laser tip was positioned at a radial distance of 8mm with goal of inducing coagulative necrosis throughout the volume between the laser fiber and thermal probe. In all patients the temperature recorded by this probe exceeded 55°C while the rectal wall remained at approximately body temperature. As no long-term serious adverse events were reported, the trial

provides substantial evidence suggesting that MR-US fusion guided FLA with interstitial thermal can be performed safely.

Oncologic control was assessed over a 9-month period. In the first four patients, minimal PSA decline was observed and residual clinically significant cancer was detected via biopsy. The final 6 patients were treated using a refined protocol in which an echogenic biopsy needle was used to improve laser fiber placement. This cohort of patients exhibited PSA decline similar to a previous MR-guided FLA trial. Moreover, on follow-up biopsy no evidence of CaP was seen in 3 patients while only small volumes of clinically insignificant cancer were seen in the other 3 patients. Finally, the thermal data collected in the trial was used to perform retrospective analysis of the utility of interstitial optical probes. The optimal exposure duration was quantified using the Arrhenius damage model calibrated with kinetic parameters determined in various studies. Due to wildly conflicting estimates of these parameters, significantly different estimates of the optimal exposure duration were calculated. Consequently, we conclude that the utility of interstitial thermal probes is inherently limited due to inaccurate thermal damage models.

### **1.1.3. Chapter 4**

Chapter 4 introduces the concept of interstitial optical monitoring, reviews the fundamentals of laser-tissue interaction and presents a preliminary proof of concept study. The propagation of light in tissue is governed by the absorption coefficient and reduced scattering coefficient. The inverse of each coefficient is the mean free path between absorption and scattering events respectively. The effective penetration depth is a function of both coefficients and is defined as the mean free path between

attenuation events. In tissues with long penetration depth, light is distributed over a large volume while the opposite occurs if the penetration depth is short.

During focal laser ablation photons travel through the tissue until they are absorbed by a chromophore. The deposited energy causes an increase in temperature which eventually leads to tissue coagulation which is characterized by an increase in the reduced scattering coefficient and a corresponding decrease in the optical penetration depth. We therefore hypothesize that the signal recorded by an interstitial optical probe at fixed location is a function of both the optical penetration depth and the size of the coagulation zone.

A preliminary proof of concept study is described in which FLA is performed on ex vivo bovine muscle while being monitored by thermal and optical probes. The optical signal decreases as the coagulation boundary grows and reaches a steady state which may correlate to the moment in which the coagulation boundary reaches the probe. In contrast, the thermal probe exhibits an almost constant increase that is not correlated to the propagation of the coagulation boundary.

The key limitation of this study is the inability to visualize the growth of the coagulation zone and hence correlate it with the optical signal. A material must be developed that possesses similar optical and thermal properties to prostatic tissue while also facilitating quantification of the coagulation zone as a function of time.

#### **1.1.4. Chapter 5**

In this chapter we present the development of a tissue-mimicking phantom with optical and thermal properties matched to human prostate. This phantom provides a platform for the development and characterization of the optical monitoring system outlined in

chapter 6. The phantom should also find utility in the testing of FLA instrumentation, validation of FLA simulations and the development of MRT sequences.

The phantom consists of a polyacrylamide gel doped with Naphthol Green B, Intralipid, and Bovine Serum Albumin (BSA). The necessary concentration of each ingredient was determined by measuring the optical properties via fluence measurements and light diffusion theory. FLA was then performed under the same conditions as a previous clinical trial in which temperature was monitored via a thermal probe. The thermal data and induced coagulation zone were compared to clinical data to illustrate the similarity between the phantom and patient. FLA was also performed under magnetic resonance thermometry (MRT).

The requisite concentrations of Naphthol Green B, Intralipid and BSA were found to be 0.144% (w/v), 8.06% (v/v) and 31.4% (v/v) respectively. In the native state, the absorption coefficient and reduced scattering coefficient ( $\mu'_s$ ) were  $0.66 \pm 0.06 \text{ cm}^{-1}$  and  $8.27 \pm 0.50 \text{ cm}^{-1}$  respectively, with  $\mu'_s$  increasing to  $17.63 \pm 1.41 \text{ cm}^{-1}$  after coagulation. The thermal response of the phantom was similar to that observed clinically with maximum thermal probe measurements of  $64.2^\circ\text{C}$  and  $66.9^\circ\text{C}$  respectively. The shape of the induced coagulation zone was qualitatively and quantitatively similar to the MRT zone of elevated temperature and the coagulation zone observed clinically.

In conclusion, in this chapter a phantom which simulates optical and thermal response to 980nm FLA was constructed and demonstrated to be similar to human prostate.

### 1.1.5. Chapter 6

In this chapter an optical monitoring system is developed and evaluated in both the tissue mimicking phantom and ex vivo bovine muscle. The primary components of the system are an interstitial optical probe, a photodiode, a microcontroller and a PC running custom developed software capable of real-time analysis and feedback.

The system is based on the hypothesis that the optical intensity at a fixed point can be correlated to the growth of the coagulation boundary. To demonstrate this, four optical probe prototypes were tested in the tissue mimicking phantom using MRI to track the coagulation boundary over time. The tissue mimicking phantom was designed specifically to facilitate contrast between the coagulated and native states and thus facilitate this novel experiment. A correlation between the recorded optical signal and the growth of the coagulation zone was clearly demonstrated. As hypothesized, the optical signal decreases as the coagulation boundary propagates towards the optical probe and reaches an inflection point at the moment of contact. Despite different designs, the 4 interstitial optical probes exhibited similar performance with mean absolute error ranging from 0.25mm to 0.39mm.

The chosen optical probe, termed 'Ballistic', is designed to preferentially detect ballistic and snake photons i.e. photons that travel directly from the laser fiber to the optical probe. This probe was tested in ex vivo bovine muscle with the goal of achieving predefined coagulation zones based on feedback from the custom developed software platform. A total of 20 samples were tested with target coagulation radii ranging from 4-7mm. The mean absolute error between the target coagulation radius and the measured radius was  $0.3 \pm 0.1$ mm. These promising results suggest that interstitial optical monitoring can be used as a feedback modality for FLA. The primary advantage



of this approach over interstitial thermal probes is that inaccurate thermal damage models are not required.

# CHAPTER 2

## Background

### 2.1. Prostate Cancer Management

#### 2.1.1. Imaging

In contrast to breast cancer, conventional imaging techniques such as US, x-ray, computed tomography (CT) and positron emission tomography (PET) have limited utility in CaP diagnosis. The diagnostic accuracy of transrectal ultrasound is similar to a digital rectal exam as some cancers are visible while some are not; therefore, it has minimal value in cancer detection [12]-[14]. Similarly CT scans fail to differentiate intraprostatic anatomy and play no role in CaP detection or staging [15]. PET is useful for localization of biochemically recurrent CaP but suffers from low specificity resulting in difficulty differentiating between benign and malignant prostatic tissue [16].

Unlike conventional imaging modalities, multiparametric magnetic resonance imaging (mpMRI) has high sensitivity for detecting clinically significant CaP [17]. The region of interest (ROI) identified by mpMRI is quantified based on  $T_2$ -weighted, diffusion weighted and dynamic contrast-enhanced images. While mpMRI has demonstrated high sensitivity for CaP, the  $T_2$ -weighted image used to define the ROI volume has been found to underestimate the extent of the cancerous lesion [18].

### **2.1.2. Biopsy**

Transrectal ultrasound (TRUS) guided biopsy is a diagnostic standard for men with suspected cancer on the basis of elevated PSA or abnormal digital rectal exam. A systematic biopsy usually involves the acquisition of 10-12 cores via a template to ensure sampling throughout the gland. Minor bleeding and urinary symptoms are frequently observed after biopsy but usually do not require intervention [19]. There is also an increasing risk of infection which must be promptly treated with antibiotics. The advent of mpMRI lead to the adoption of MRI guided biopsies in which the suspicious ROI is directly sampled. The value of this approach is illustrated in a study where CaP was found in >50% of men with a previous negative TRUS biopsy and elevated PSA [20]. Widespread adoption of MRI guided biopsy is hindered due to the associated high costs and long procedure times. Consequently, magnetic resonance - ultrasound fusion (MR-US) biopsy was developed. This technique combines the previously acquired mpMRI derived ROI with real-time ultrasound via a fusion biopsy platform (Figure 1). The ROI from the MRI scan is imported by the fusion platform and registered with the real-time ultrasound image allowing the ROI to be displayed and targeted.



Figure 1: The Artemis MRI-US fusion biopsy platform (Eigen, Grass Valley, CA)

In comparison to standard TRUS biopsy, MR-US fusion biopsy provides increased detection of high-risk prostate cancer and also decreased detection of low-risk CaP. In one study MR-US fusion biopsy detected 30% more high high-risk CaP and 17% fewer low-risk CaP than standard biopsy [21]. As the procedure can be performed in a clinic, the cost and procedure time is dramatically lower than MRI guided biopsy while still offering the ability to sample tissue from suspicious regions. In addition, a systematic biopsy can also be taken in the same session without a substantial increase in procedure time.

### **2.1.3. Rational for Focal Therapy**

Men diagnosed with CaP are usually offered three options: 1) radical prostatectomy, 2) radiation therapy and 3) active surveillance. Radical prostatectomy is a surgical procedure in which the prostate and surrounding tissue is excised. The procedure is commonly undertaken using a minimally invasive approach with the Da Vinci Surgical

System (Intuitive Surgical Inc., Sunnyvale, CA). In contrast, radiation therapy achieves oncologic control without removing tissue. This is undertaken either with external beam radiation or brachytherapy. The final option, active surveillance, is not a treatment but rather a strategy to assess the progression of CaP and only intervene when deemed appropriate. Active surveillance consists of PSA blood tests, digital rectal exams and repeat biopsies at regular intervals. Men with life expectancy >10yr and low-risk CaP are ideal candidates for AS; however, 30% of these men will eventually need radical intervention [5].

There is a low incidence of disease progression for both radical prostatectomy and radiation therapy [22]; however, these procedures are associated with high rates of side-effects such as erectile dysfunction and urinary incontinence [3]. It is therefore desirable to either delay RP as long as possible or to forego the procedure entirely when it is not necessary. The patient is often faced with a difficult decision whether to opt for intervention and live with the ensuing reduction in quality of life or choose active surveillance. The conundrum in choosing treatment is illustrated in a study in which 347 men received RP and 348 underwent active surveillance. At 23.2 years follow-up it was noted that RP significantly reduced mortality; however, a large proportion of the active surveillance group did not require any palliative treatment [4]. Many patients elect for intervention due to the fear of living with cancer; therefore, overtreatment has become a concern. This trend for overtreatment is exacerbated by the widespread adoption of PSA and biopsy which has resulted in detection of many smaller, lower stage and clinically insignificant cancers.

Active surveillance and intervention are the obvious choice for low-risk and high-risk CaP respectively. However, the choice of treatment is particularly difficult for men

diagnosed with intermediate risk CaP. For this reason, there is a growing interest in focal therapy, the goal of which is to treat the cancerous tissue while minimizing damage to surrounding structures. There are a number of competing approaches under investigation including cryotherapy, irreversible electroporation and hyperthermia, the latter of which is the focus of this thesis. All of these procedures offer a minimally invasive method of treating tissue and can be targeted to the correct location due to improved diagnostic techniques. In particular, mpMRI and targeted biopsy have facilitated localization of the cancerous lesion within the prostate.

## **2.2. Hyperthermia**

Hyperthermia as a form of treatment consists of raising tissue temperature to elicit a cellular response, which may include death. It dates back to 2600BC when the Egyptian polymath Imhotep reportedly used ‘fire drills’ to treat breast cancer [23]. Despite this ancient origin, widespread adoption of hyperthermia in cancer treatment has always been hampered due to difficulty administering thermal energy in the desired location with the appropriate magnitude and exposure duration. While ‘fire drills’ have been consigned to history, treatment planning and control techniques remain rather primitive.

Today, hyperthermia is employed both as an adjuvant treatment modality to chemotherapy and radiotherapy as well as in isolation via thermal ablation. This chapter focuses on the latter in which high temperatures are used to induce cellular damage via conformational changes of molecules, bond destruction and membrane alterations. At 50°C, enzyme activity is inhibited leading to reduced energy transfer within the cell and the disruption of repair mechanisms. Coagulation cellular necrosis occurs at

approximately 60°C due to denaturation of proteins and collagen. At temperatures above 80°C, membranes become increasingly permeable and thus fail to maintain equilibrium chemical concentrations. Vaporization of water molecules arises at 100°C. The resulting gas bubbles can cause mechanical ruptures and thermal decomposition of tissue fragments. Tissue carbonization occurs after vaporization and at extreme temperature, above 300°C, tissue can even melt [24]. In general, tumor cells are more sensitive to hyperthermia than normal cells [25]-[28]. With appropriate dosimetry, cancer control can therefore be achieved while minimizing damage to surrounding healthy tissue. This has been demonstrated clinically in many organs, including the prostate [29], breast [30], pancreas [31], kidney [32] and liver [33].

This thesis focuses on thermal ablation which has many advantages over traditional cancer control techniques including a lower cost [34], minimal morbidity [35], less invasive [34] and in many cases can be undertaken as an outpatient procedure [36]. Energy delivery to the target has evolved considerably since the pioneering work undertaken by Westermarck [37] and Coley [38] who induced hyperthermic conditions via circulating hot water and toxin induced fever respectively. Today the primary modalities are high intensity focused ultrasound (HIFU), radiofrequency ablation (RFA), microwave ablation (MWA) and focal laser ablation (FLA). These technologies have largely solved the historic technical difficulties associated with delivering energy to targets deep within the body. In contrast, feedback mechanisms have progressed at a slower rate.

The remainder of this chapter presents the state of the art in methods of monitoring thermal ablation and is divided into sections. The first section outlines the origin, mechanism of action, advantages and disadvantages of HIFU, RFA, MWA and FLA. The current approaches to monitoring the induced temperature change are outlined in

the second section. Examples of clinical application are provided where possible. Methods of modelling tissue damage based on thermal data are discussed in third section. Due to the limitations of these models, there is a growing interest in developing alternative techniques to assess thermal damage. Progress in this area is discussed in the fourth section. In the final section we discuss the need for real-time feedback and the barriers to clinical deployment of the most promising feedback technologies.

## **2.3. Modern Thermal Ablation Modalities**

### **2.3.1. High Intensity Focused Ultrasound**

HIFU was initially used by Fry et al. [39] in 1954 to produce destructive lesions in the brain for neurological studies. It did not become popular until the 1980s when Coleman et al. [40] utilized the technology to treat glaucoma. This work led to the development of the first FDA approved HIFU device, the Sonocare CST-100 Therapeutic Ultrasound System (Sonocare Inc., NJ, USA) [41]. In 1989 Harr et al. [42] explored the possibility of using HIFU to treat liver tumors. Over 100,000 cases have since been treated including solid malignant tumors in the pancreas, liver, prostate and breast [34].

HIFU relies on two mechanisms to cause tissue destruction: (1) conversion of mechanical energy into heat, and (2) acoustic cavitation. Mechanical energy propagates harmlessly through the tissue as a sound wave. Upon reaching a focal point its intensity is of sufficient magnitude to cause tissue necrosis. The first method, conversion of mechanical energy to heat, occurs because ultrasonic waves cause vibration and rotation of molecules resulting in the production of frictional heat. The second method of tissue destruction, acoustic cavitation, arises due to compression and rarefaction caused by



ultrasonic waves. If of sufficient magnitude the negative pressure created by rarefaction draws gas out of the tissues to form bubbles. These bubbles collapse violently resulting in mechanical damage to the surrounding tissue [43].

The primary advantage of HIFU is that it is non-invasive and utilizes non-ionizing radiation. From a clinical perspective this reduces cost, recovery time and risk of infection while the absence of scarring is cosmetically preferable. HIFU does have some drawbacks including longer treatment times, limited depth of penetration and the need for an excellent acoustic window [34]. It also struggles to target moving tissue and is therefore more suitable in stationary organs such as the kidney and prostate [44]. The liver for example is not an ideal organ given that it is subject to both respiratory motion and sonic shadowing caused by the ribs [43]. Skin-burn can result in the event of poor acoustic coupling between the therapeutic window and the skin. Damage can also be caused by US reflecting off hard surfaces such as bone or from gas-containing regions such as the bowel [43]. Reliable thermometry and feedback of lesion growth remain significant problems with HIFU. Although no technique has been perfected, sonographic thermometry [45] and elastography [34] may prove useful.

### **2.3.2. Radiofrequency Ablation**

RFA was pioneered by French physicist Jacques-Arsene d'Arsonval in the late 19<sup>th</sup> century. He treated 75 patients for various conditions by placing them in large induction solenoids. The technique became known as "Arsonvalisation" [23]. In the early 20<sup>th</sup> century, diathermy, the heating of tissue by high frequency electrical currents, was introduced by the German physician Karl Franz Nagelschmidt [23]. Modern percutaneous RF ablation was successfully demonstrated independently by McGahan et

al. [46] and Rossi et al. [47] in 1990. This technique involves inserting insulated electrodes through the skin with the distal end exposed. Three years later RF ablation was successfully demonstrated in human liver tumors [48]. Today RF ablation is commonly used for primary hepatocellular carcinoma, neuroendocrine hepatic metastases, esophageal dysplastic lesions, primary and secondary liver malignancies [28].

In RFA, heat is generated in the tissue via ionic agitation [49]. A complete electric circuit is required between the electrodes and the grounding pads or between two or more electrodes. Current passes through tissue due to the presence of ionic fluid. The alternating current causes ions to oscillate back and forth rapidly resulting in the production of frictional heat. Thermal conduction enables heat to transfer to areas of the tissue that are not along the electrical path.

As with all the techniques discussed here RFA is less invasive than traditional surgical approaches which results in lower cost, less risk of infection and faster recovery times. Of all of these techniques RFA is the most widely used [50]. In particular it is now the standard of care for surgical management of primary and secondary liver malignancies [28]. Disadvantages of RFA include the need for grounding pads which can cause skin burns and the necessity for tissue with good thermal and electrical conductivity [51].

### **2.3.3. Microwave Ablation**

Development of MWA applicators for tumor treatment began in the 1970s [52]. Numerous studies have since demonstrated that MWA therapy is capable of providing sufficient energy to control tumors via hyperthermia alone [53], [54] and significantly

increase the effectiveness of chemotherapy and radiotherapy [55]-[59]. The initial designs consisted of a single antenna; however, arrays were subsequently developed to increase the ablation volume and enable conformity to irregular tumor volumes [52]. Clinical trials have demonstrated the use of MWA for tumor treatment in the liver [60], lung [61], kidney [62], bone [63], pancreas [64], adrenal glands [63], brain [53], [55] and prostate [54], [65].

Electromagnetic radiation can be visualized as a wave oscillating from a positive to negative electric charge. Water molecules are polar with the hydrogen side of the atom having a positive charge, while the oxygen side has a negative charge. The interaction between electromagnetic radiation and water thus causes the water molecule to flip as the sign of the electromagnetic radiation oscillates from positive to negative. The interaction is maximized as microwaves are tuned to the natural frequency of water molecules. The net result is that the molecules flip back and forth 2-5 billion times per second. Heat is created through friction and if of sufficient magnitude and duration will cause cellular death via coagulation necrosis [66].

In contrast to RFA, MWA produces higher tissue temperatures, larger ablation volumes, shorter ablation times and an improved convective profile [66]. In addition, MWA does not require grounding pads, which have been known to cause burns. MWA is also more effective than RFA in tissue with large heat sinks (kidney and liver) and tissues with poor electrical and thermal conductivity (lung and bone) [51]. While MWA has been identified as a possible replacement for RFA, there are some limitations that have prevented this from becoming a reality. Microwave power is more difficult to generate and deliver than that used in RFA or FLA as coaxial cables must be used. These cables are much thicker than those used in RFA and FLA and the cable itself is susceptible to

heating which causes energy delivery to surrounding healthy tissue. In addition MWA probes tend to be large and the resulting ablation zone tends to be long thin and difficult to predict [67]. Cooled-shaft antennas have recently been developed which allow higher power outputs while minimizing skin burns and undesirable heating from the cable [68].

### 2.3.4. Focal Laser Ablation

In the 1980s the neodymium-doped yttrium-aluminum garnet (Nd:YAG) laser was used as a precise method of surgical dissection to treat head and neck tumors [44]. FLA was soon utilized to treat liver tumors with significant work being undertaken in the late 1980s and early 1990s by Hashimoto [69], Hahl et al. [70] and Dowlatshahi et al. [71]. The results of a clinical trial by Nolsoe et al. [72] in 1993 successfully demonstrated that the procedure was both efficacious and safe. Since then FLA has found utility in the treatment of tumors in many organs including prostate [11], [29], [73], breast [74], liver [75], lung [76] and brain [77].

FLA causes temperature elevation due to the transfer of photon energy to kinetic energy. This process consists of two steps; absorption and deactivation. In the absorption step the target molecule (A) absorbs a photon of light with energy  $h\nu$  and is promoted to an excited state ( $A^*$ ):  $A + h\nu \rightarrow A^*$ . By colliding with a neighboring molecule (M) the target molecule becomes deactivated and the photon energy increases the kinetic energy of M:  $A^* + M(E_{kin}) \rightarrow A + M(E_{kin} + \Delta E_{kin})$ . Ultimately this increase in kinetic energy results in tissue destruction [24].

Due to its minimally invasive nature, FLA has the same advantages as the other techniques in terms of cost, length of hospital stay, and chance of infection. In addition, the optical fibers used in FLA are of smaller diameter than probes used by MW and RF.

This makes FLA ideal for small organs such as the prostate. However, in FLA, high temperatures immediately adjacent to the laser fiber can cause carbonization. The resulting charring severely limits optical penetration and thus prevents further lesion growth. In other modalities such as MWA, charring does not prevent energy transfer. Another limitation is the small ablation zone, typically 10-15mm in diameter. To create larger ablation zones multiple ablations can be undertaken by moving the fiber or by using a beam spitting multiple fiber system [78].

## **2.4. Thermal Dosimetry**

Achieving accurate thermal dosimetry is a necessary prerequisite to estimating damage using traditional approaches such as the Arrhenius model. There are many methods available to record temperature, most of which have been adapted from various industrial applications. Thermal dosimetry can be divided into four groups: thermography, electrical probes, optical fiber probes and radiologic imaging.

### **2.4.1. Thermography**

Thermography enables the recording of temperature over a 2D area using noninvasive techniques. There are three common types: liquid crystal, infrared and microwave.

#### **Liquid crystal**

Liquid crystals are organic compounds such as cholesterol derivatives. They reflect light in a temperature dependent manner as the wavelength reflected decreases with rising temperature. The sensor must contact the material whose temperature is being

examined. Thermochromic liquid crystals are particularly useful for determining thermal profiles when developing complex ablative techniques [79], [80]. Clinically they were once considered to have some limited utility in breast cancer detection [81]. Thermochromic liquid crystals must be sprayed onto the location of interest and thus are not suitable for interstitial use; hence, the scarcity of reports on clinical utilization.

### **Infrared**

This technique uses an infrared (IR) camera to record electromagnetic radiation emitted from the target surface. The sensor is either a crystal of mercury-cadmium-telluride or indium-antimonide, both of which change electrical conductivity depending on the radiant power received [82]. IR cameras have been used in the development of ablative techniques [83]–[86] but not in a clinical setting. This is likely due to the requirement for a direct line of sight which is difficult to achieve in minimally invasive treatment.

### **Microwave**

Microwave signals are detected using a radiometer which consists of an antenna and receiver. The radiometer can either be in contact or at a distance from the target. In contrast to the aforementioned techniques, microwave thermography can detect signal from subsurface tissues. The depth of penetration decreases with increasing frequency while the opposite is true for spatial resolution, hence, a balance must be struck between these two desirable characteristics. It is possible to undertake interstitial monitoring of ablative therapies [87]; however, adoption of this technique has been limited due to poor spatial and temporal resolution. In addition, ablation tends to form air bubbles within

the target which scatters microwaves and thus interferes with temperature estimation [88].

## **2.4.2. Electrical Probes**

An alternative to 2D thermographic mapping is 1D point measurements via interstitial electrical probes.

### **Thermistors**

Thermistors work on the semiconductor property that electrical resistance decreases as temperature increases [89]. They can be manufactured with very small dimensions; outer diameters of 1mm are attainable. In addition they possess fast response times on the order of one second [82]. Self-heating and conduction can cause significant errors. Self-heating occurs when the probe absorbs energy at a faster rate than the surrounding tissue. Such a scenario would arise if a probe was placed within two optical penetration depths of a laser during FLA. Furthermore, the thermal conductivity of metals can be up to 1000 times greater than soft tissue. As a result conduction error can occur when the probe is placed in a high temperature gradient [82]. Metals also possess a density 3-10 times greater than soft tissue. This becomes a problem in HIFU procedures. Due to the density mismatch the ultrasound wave induces relative motion between the tissue and wire. Friction leads to a heating affect called 'viscous heating' which artificially inflates the temperature measurement [90]. Nevertheless thermistors have been used to monitor temperature during MWA [68], RF ablation [91] and FLA [74].

## **Thermocouples**

Thermocouple sensors are based on the Seebeck effect which states that an electrical potential difference occurs between two points in an electrically conducting material if they are simultaneously at different temperatures. Junctions are required to make an effective sensor as unlike thermistors, thermocouples are relative sensors. One conductor must be at a known temperature as the voltage produced depends on the temperature difference between the two conductors [92]. Advantages include low cost, versatility and ability to measure temperature over a wide range [82]. In contrast to thermistors, thermocouples come in a very small form factor with micro-thermocouples having outer diameters well below 1mm.

Rapid response times of 0.1s are also advantageous [82]. Micro-thermocouples have been used to monitor temperature at the tumor boundary during laser induced hyperthermia [93]. Thermocouples are manufactured from metal and suffer from self-heating and conduction errors as described for thermistors. Thermocouples are frequently incorporated into the design of RF electrodes to enable temperature monitoring at the tip of the electrode [94], [95]. Thermocouples have also been used to monitor MWA [96], [97] and FLA [98], [99].

### **2.4.3. Fiber-optic Temperature Sensors**

The primary advantage of fiber-optic temperature sensors is that they contain no metallic components and as such are suitable for environments containing electrical and magnetic fields. This is a major advantage as many thermal ablation procedures are carried out under MR guidance. There are two types of fiber-optic temperature sensors suitable for monitoring ablation procedures: fluoroptic probes and fiber Bragg Grating



(FBG) sensors. Both of these sensors are invasive as they require thermal coupling with the tissue.

### **Fluoroptic Probes**

Fluoroptic probes consist of a sensor composed of phosphor and a pulsed light source such as a xenon flash lamp. The phosphor sensor is placed at the end of an optical fiber. The light source causes the phosphor to fluoresce. Its decay is temperature dependent; therefore, temperature can be derived by recording the decay time [92]. Both excitation and emission occur along a single optical fiber which can be interstitially placed to provide a point measurement. This technology was pioneered by Lumasense Technologies (Santa Clara, Ca, USA) in the 1970s. These probes can achieve an accuracy of 0.5°C and a range of -100°C to +330°C with a measurement rate of up to 4Hz. Probe diameter can be as small as 0.25mm with a response time of 200ms.

A disadvantage of this system is artifact induced during FLA. FLA is frequently performed using light at a wavelength of 980nm. This lies within the spectrum used by the fluoroptic temperature measurement system. As a result, considerable measurement error can occur if probes are placed too close to the laser fiber. This artifact can be mitigated by coating the probe with an optically opaque material or blocking the offending wavelength with a filter. Self-heating can also occur due to absorption of light by the probe coating [100]. Fluoroptic probes have been used in clinical trials for the treatment of prostate cancer using FLA [29], [73] and MWA[65] as well as RFA for breast cancer [101].

## Fiber Bragg Grating Sensors

In contrast to fluoroptic probes, FBG sensors are capable of measuring temperature at multiple positions in the same optical fiber. FBG sensors use an optical fiber with a periodic variation in refractive index. Light travelling down the fiber is then reflected in a wavelength specific manner. Most of the reflected light causes destructive interference but at a narrow range of wavelengths constructive interference allows light to travel back up the fiber. The maximum reflectivity occurs at the Bragg wavelength given by:

$$\lambda_b = 2\eta_{eff}\Lambda$$

where  $\eta_{eff}$  is the refractive index and  $\Lambda$  is the FBG period. A shift in wavelength occurs when either a change in strain or temperature is applied. For this reason, if used as an interstitial temperature sensor the fiber must be protected by a rigid support. By removing the strain dependence, the shift in wavelength can be used to determine temperature [102].

Using multiple FBGs in the same fiber enables distributed temperature sensing (DTS) along the length of the fiber. The two most common approaches for DTS are Wavelength-Division Multiplexing (WDM) and Time-Division Multiplexing (TDM). In WDM many different FBGs with unique Bragg wavelengths are distributed along the fiber. A tunable swept-wavelength light source is used to emit light at wavelengths matching the Bragg wavelengths of the FBGs. In this way the location of the reflected wave is determined by its wavelength. The width of the FBG reflections and the light source limits the number of sensors in a given channel to approximately 100. The alternative approach, TDM, utilizes a pulsed broadband light source. Sensor location is determined by the time it takes to receive the reflected light. Sensor spacing must be sufficient to differentiate pulses from adjacent sensors. There is no tunable laser in this system, thus

it is considerably less expensive than the WDM approach [102]. A major advantage of FBG sensors is that multiple FBGs can be incorporated into a single fiber. Submillimeter resolution with an accuracy of  $\pm 0.5^{\circ}\text{C}$  has been demonstrated during *ex vivo* monitoring of RF ablation [103]. Adoption of this technology for medical applications has been hindered by the relatively high equipment costs [104].

## 2.4.4. Radiologic Imaging

### Acoustic Temperature Sensors

There are numerous ultrasound parameters that exhibit temperature dependence including frequency-dependent attenuation and back scattered power but the shift in ultrasound frequency signal appears the most promising. The shift in signal occurs due to thermal expansion and a change of the speed of sound in the medium with temperature elevation. Thermal expansion has only a minor effect in comparison to the temperature dependence of the speed of sound. The primary limitation is that the speed of sound increases only in non-fatty tissues and only up to  $50^{\circ}\text{C}$  [105], thus, this technique is inappropriate for hyperthermia at high temperatures.

Acoustic temperature sensing is used commercially in the Sonablate®500 HIFU system which provides a package called ‘Tissue Change Monitoring’ (TCM). TCM uses spectral analysis of RF backscattered ultrasound signals to estimate tissue temperature. The reliability of this technique remains to be proven. Focus Surgery, the developer of the Sonablate system, performed an *in vivo* study to assess the accuracy of the TCM system [106]. 5 men with histologically confirmed prostate cancer received HIFU treatment. Temperature within the target zone was monitored via thermocouples and TCM. The average temperature found was  $84^{\circ}\text{C}$  and  $91^{\circ}\text{C}$  for the thermocouples and TCM

software respectively. While the study clearly demonstrates a correlation between TCM readings and temperature, the accuracy of the system deteriorates above 50°C. The authors speculate that this may be due to tissue expansion and cavitation/microbubbles.

### **Magnetic Resonance Thermometry**

Magnetic resonance thermometry (MRT) provides a non-invasive method for monitoring thermotherapy. MR parameters such as  $T_1$  relaxation [107],  $T_2$  relaxation [108] and water diffusion [109] are temperature dependent; however, proton resonance frequency (PRF) shift is the dominant approach [110] for MRT. The PRF method takes advantage of the linear correlation between temperature and the frequency shift of protons. The frequency shift is determined by measuring the difference in phase acquired by two gradient echo scans. The change in temperature between the scans ( $\Delta T$ ) is given by:

$$\Delta T = \frac{\varphi - \varphi_{ref}}{\gamma \cdot \alpha \cdot B_0 \cdot TE}$$

where  $\alpha$  is the PRF change coefficient, TE is the time to echo of a gradient echo pulse sequence,  $\varphi$  is the phase of the acquired signal,  $\varphi_{ref}$  is the phase of the reference signal,  $\gamma$  is the gyromagnetic ratio and  $B_0$  is the magnetic field strength of the MR scanner.

The need for a baseline phase image renders this technique inherently vulnerable to motion artifact (Figure 2). Clinically, these artifacts can arise due to cardiac, respiratory, peristaltic or bulk motion. In an effort to mitigate this limitation a referenceless approach was developed in which the reference phase is acquired from a region outside the thermotherapy zone instead of the baseline scan [111]. This approach has been successfully demonstrated *in vivo* for monitoring ablation of the liver via FLA [112] and HIFU [113]. Regardless of the approach used the reference signal must be acquired from a region of known temperature. This is generally assumed to be 37°C;

however, this assumption is not always valid. Bitton et al. found that residual heat from successive ablations during HIFU could result in a baseline temperature as high as 50°C resulting in a 91% underestimate of the induced damage zone [114]. The PRF approach suffers from many other sources of error including perfusion-based phase changes, ablation induced structural changes and magnetic susceptibility variations. These issues are covered in greater details in an excellent review article by Winter et al. [115].

A further limitation of MRT is the inability to use ferromagnetic materials, which necessitates the development of specialized tools. Poor temporal resolution and spatial averaging can also limit utility. The temperature measured by MRI is averaged for each voxel and has been shown to be up to 30% less than the peak value within the voxel [116]. Nevertheless, PRF shift thermometry is a promising non-invasive technique and has been used clinically to monitor FLA [29], RFA [117] and HIFU [118] and MWA [65].

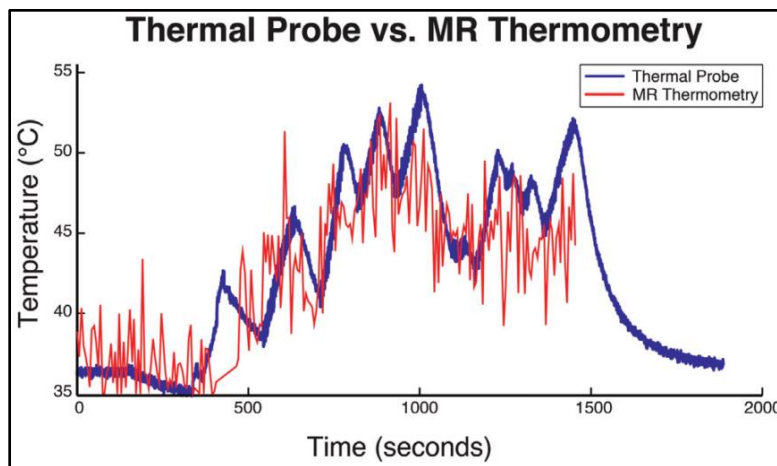


Figure 2: Comparison of MR thermometry and interstitial thermal probe measurement during FLA for the treatment of prostate cancer. Motion artifact is responsible for the noise evident in the MR data [73].

## CT Thermometry

X-ray attenuation depends on the interaction between the x-ray and the intervening tissue which is primarily Compton scattering. Compton scattering is influenced by temperature and although it is beyond the scope of this review paper to discuss the physics in further detail it can be shown that the relationship between temperature and received x-ray intensity is given by:

$$\Delta CT \approx -[1000 + CT(T_0)] \cdot \alpha \cdot \Delta T$$

where  $\Delta CT$  is the change in CT number due to a change in temperature,  $CT(T_0)$  is the initial temperature,  $\alpha$  is the volumetric expansion coefficient and  $\Delta T$  is the change in temperature [104]. This technique is rarely used as CT scans subject patients to excessive ionizing radiation. Nevertheless experimental work has demonstrated that it can be used to monitor both FLA [119] and RFA [120]. Further information on this topic can be found in a recent review article by Fani et al. [121].

## 2.5. Damage Estimation

In oncology, the goal of thermal ablation is to destroy cancerous cells while minimizing damage to surrounding structures. This may be achieved using thermal data in conjunction with damage estimation models such as the Arrhenius model and the Thermal Isoeffect Dose model.

### 2.5.1. Arrhenius Model

The Arrhenius model was developed by Swedish chemist Svante Arrhenius (1859-1927) to demonstrate the relationship between temperature and the rate constant of a chemical reaction:

$$k = Ae^{-\frac{E_a}{RT}}$$

where  $k$  is the chemical reaction rate constant ( $s^{-1}$ ),  $A$  is the pre-exponential/frequency factor [ $s^{-1}$ ],  $E_a$  is the activation energy barrier [ $J \text{ mole}^{-1}$ ],  $R$  is the universal gas constant ( $1.987 \times 10^{-3} \text{ Kcal/mole}\cdot\text{K}$ ), and  $T$  is the temperature (K). Arrhenius' equation demonstrates that lower activation energies and higher temperatures increase the rate constant of a given reaction. The exponential part quantifies the fraction of reactant molecules with sufficient energy to react in accordance with the Maxwell-Boltzmann law. The pre-exponential factor is the product of the rate at which molecules come into contact, the frequency/collision factor ( $Z$ ), and the relative orientation of those molecules called the steric factor ( $\rho$ ) i.e.  $A = Z\rho$ .

This first order rate process model was first applied to hyperthermia by Moritz and Henriques in 1947[122]-[125]. In their work, damage was quantified using a single parameter ( $\Omega$ ) as shown below:

$$\ln\left(\frac{C(0)}{C(t)}\right) = A \int_0^t e^{-\frac{E_a}{RT(t)}} dt = \Omega(t)$$

where  $C(0)$  is the concentration of viable cells before the procedure and  $C(t)$  is the concentration at time= $t$ . The fraction of surviving cells is thus given by:

$$C(t) = 100e^{-\Omega} (\%)$$

In practice the kinetic parameters ( $A$  and  $E_a$ ) must be determined *a priori*. This can be done experimentally by assuming the tissue becomes non-viable at a certain fraction of remaining cells. This value is often assumed to be 36.8% which implies that  $\Omega = 1$ .

## 2.5.2. Thermal Isoeffect Dose Model

Thermal damage is a function of the magnitude in the change of temperature ( $\Delta T$ ) and the duration of said change; therefore, the  $^{\circ}\text{C}\cdot\text{min}$  may seem an appropriate metric. However, this metric fails to account for variation in the rate of cell death. For example, if temperature was raised from  $37^{\circ}\text{C}$  to  $42^{\circ}\text{C}$  and held for 10 minutes one would get  $50^{\circ}\text{min}$ . An elevation from  $37^{\circ}\text{C}$  to  $62^{\circ}\text{C}$  for 2 minutes also results in  $50^{\circ}\text{min}$ . The latter results in far greater cell death than the former; therefore, the  $^{\circ}\text{C}\cdot\text{min}$  unit cannot be used as a measure of thermal damage [126]. Similarly, analysis based on energy input using a unit of Joules is also biologically meaningless as it fails to consider the duration of time at the elevated temperature. Moreover, in traditional hyperthermic treatment the tissue in question is gradually heated and thus time at desired elevated temperature is less than total exposure duration. To solve these issues the thermal isoeffect dose (TID) model was introduced by Sapareto and Dewey [127]. The TID model converts thermal history into cumulative equivalent minutes at  $43^{\circ}\text{C}$  ( $\text{CEM}_{43}$ ) and is calculated as follows [128]:

$$\text{CEM}_{43} = \sum_{i=1}^N t \times R^{43-T_i}$$

Where  $\text{CEM}_{43}$  is the cumulative number of equivalent minutes at  $43^{\circ}\text{C}$ ,  $t$  is the time interval (min),  $T$  is the average temperature during the time interval  $t$  and  $R$  is the number of minutes needed to compensate for a  $1^{\circ}\text{C}$  temperature change to an isoeffect



of thermal injury. The parameter  $R$  is dependent on temperature and the activation energy:  $R = e^{-E_a/(R_g T(T+1))}$  where  $R_g$  is the gas constant. Further details on both models can be found in an excellent review article by Dewhirst et al. [128].

### 2.5.3. Challenges with Traditional Models

The TID model is derived from the Arrhenius model; however, due to some assumptions and simplifications the results are not necessarily identical. The TID and Arrhenius models provide similar results below 50°C ; however, the TID model tends to underpredict thermal injury for temperatures exceeding 50°C [129]. Many studies have set  $R$  to a constant value of 0.5 for traditional hyperthermia techniques which utilize temperatures below 50°C. While appropriate for such conditions this assumption provides erroneous results for hyperthermia techniques above 50°C which is commonly observed during ablation procedures. Instead  $R$  should be calculated as a function of temperature and activation energy [129].

A major limitation of both models is the requirement for a priori knowledge of the kinetic parameters. Bhowmick et al. conducted a study to determine these parameters for the prostate [130]. In that study, 1mm thick slices of prostatic tissue were placed on a temperature-controlled copper block. Tissue response for various temperature-time combinations was assessed via histology and dye uptake assays. Table 1 shows the empirically derived kinetic parameters found by Bhowmick et al. as well as many other authors. The difficulty obtaining reliable values is elucidated by the conflicting results of the dye uptake and histology study in the Bhowmick study alone [130]. Furthermore, throughout the literature many different values have been derived for the same tissue. Some of the difficulty is attributed to the fact that the kinetic

parameters depend on the cell or tissue type analyzed, the injury assay (clonogenics, dye uptake, histology) used and the time permitted post thermal therapy to allow for injury manifestation [129]. An inability to ensure isothermal heating is also an issue with errors occurring due to either temperature gradients existing in the tissue or damage incurred during the ramping up and down of temperature to the desired magnitude. The general trend is that dye uptake assays for cell injury provide a lower activation energy and higher thermal threshold than clonogenics assays and similar results to histology [129]. Recently, MacLellan et al. demonstrated a method of deriving the thermal dose parameters using a combination of thermal data gathered in real-time via MRT and post-treatment T1-weighted MRI [131]. The technique requires only retrospective analysis of clinically acquired data; thus, it greatly simplifies the acquisition of the model parameters in comparison to traditional laboratory experiments. Perhaps this technique will lead to improved quantification of the thermal dose parameters and facilitate widespread implementation of the Arrhenius model.

There is considerable uncertainty involved in finding accurate kinetic parameters and relatively minor differences in these parameters can have a major impact on predicted damage volume. In Table 1 we have calculated the percentage of surviving cells for various kinetic parameters using the Arrhenius model with an exposure duration of 4 minutes and a temperature of 55°C. This is an idealized scenario but it demonstrates a number of important points that need to be considered when designing a treatment monitoring system. Firstly, kinetic parameters are organ-specific. In this case, if the parameters for skin were used for the kidney or prostate the treatment monitoring system would incorrectly indicate a survival of less than 3%. Secondly, even if organ specific kinetic parameters are used, the reliability of the Arrhenius model for

oncologic control remains unclear. For example, in prostate the parameters from the Rylander study indicate a cell survival under 5% in this scenario. In contrast the kinetic parameters found by Bhowmick et al. suggest approximately 60% of the cells will survive. The Arrhenius model is currently utilized clinically by the Visualase system (Medtronic, Dublin, Ireland) for monitoring FLA. A recent study found that the Visualase system overestimates the volume of tissue damage when compared to histopathology [132]. This may have occurred due to the utilization of inaccurate kinetic parameters. Alternatively, erroneous thermal data could have been responsible as the Visualase system relies on MRT which is susceptible to numerous sources of error including motion artifacts. Nevertheless, the Arrhenius and TID models represent promising solutions for damage estimation based on thermal data. In the next section, methods of monitoring ablation that do not rely on thermal data will be discussed.

Table 1: Kinetic Parameters and Percentage Surviving Cells after 4 Minutes Exposure at 55°C

	$E_a$ (kJ mole <sup>-1</sup> )	A (s <sup>-1</sup> )	Survival (%)
<b>Prostate</b>			
Bhowmick (dye uptake) [130]	167.8	$1.10 \times 10^{24}$	59.78
Bhowmick (histology) [130]	160.7	$7.78 \times 10^{22}$	61.20
Rylander [133]	124	$7.00 \times 10^{17}$	4.64
<b>Kidney</b>			
He (cell suspended) [134]	287.49	$4.36 \times 10^{43}$	16.39
He (cell attached) [134]	314.89	$3.15 \times 10^{47}$	56.65
Walsh [135]	202.6	$1.29 \times 10^{29}$	84.01
<b>Skin</b>			
Henriques [122]	630	$3.10 \times 10^{98}$	2.07
Weaver [136]	327	$1.82 \times 10^{51}$	~0
Takata [137]	669	$9.39 \times 10^{104}$	0.07

## **2.6. Non-Thermal Feedback Techniques**

Numerous methods of damage estimation exist which do not rely on thermal data and damage models. Techniques based on ultrasound, MRI and thermally induced changes in optical properties have been demonstrated; however, in many cases the clinical utility of the technology remains to be seen. This section is divided into the following categories: 1) Ultrasound Imaging, 2) Elastography and 3) Optical Monitoring.

### **2.6.1. Ultrasound Imaging**

#### **B-mode imaging**

In conventional B-mode images the induced lesion appears as a hyperechoic region. This is caused by the formation of acoustically or thermally generated bubbles which scatter more incident ultrasound than normal tissue [105]. While this method can identify the lesion, the margin remains poorly identified making it difficult to differentiate coagulated from healthy tissue. Nevertheless, B-mode imaging has been used with HIFU [138] and MWA in China [139]. B-mode imaging has also been used clinically to monitor RFA of hepatic tumors but was found to result in significantly fewer complete ablations in comparison to contrast enhanced ultrasound ( $p=0.043$ ) [140]. FLA for liver metastases has also been monitored via B-mode imaging; however, the authors noted that the margins were 'irregular and poorly defined' and insufficient for assessing the true extent of the ablation zone [141].

## **Nakagami Imaging**

Nakagami imaging utilizes a statistical model to calculate the Nakagami parameter from the backscattered ultrasound signal [142]. Like B-mode imaging, contrast is generated due to the formation of bubbles in the ablation zone. In a recent study by Zhang et al. the Nakagami parameter was found to increase from 0.47 to 0.82 during MW ablation of *ex vivo* porcine liver [143]. In addition, Nakagami imaging exhibited a superior contrast-to-noise than conventional B-mode imaging. Similar results were found by the same group during HIFU in tissue-mimicking phantoms [142]. Experiments in porcine liver have also demonstrated the potential for RFA monitoring [144]. Interestingly, in the same study Nakagami imaging was found to be unsuitable for monitoring RFA in muscle tissue. It was hypothesized that muscle fibers act as strong scatterers thus limiting the effect of increased scatter from bubble formation. Additionally, there may be greater bubble formation in liver tissue as hepatic cells contain more intercellular fluids than muscle fibers. Motion and tissue inhomogeneity can also degrade parameter estimation. The use of Nakagami imaging in monitoring thermal ablation is a relatively recent development and further *in vivo* studies are required to fully demonstrate its potential.

## **Contrast Enhanced Ultrasound**

Contrast enhanced ultrasound (CEUS) was developed to assess perfusion and has been used to detect tumors as tumors generally possess increased microvessel density. The technique involves injecting US contrast agents, which consist of small encapsulated gas bubbles into the vasculature. This increases the sensitivity of Doppler imaging thus enabling assessment of perfusion [145]. Thermal ablation results in a nonperfused lesion which appears as a hypoechoic region on CEUS images [29]. This has been

successfully demonstrated for lesions induced by FLA [146], HIFU [147], MWA [148] and RFA [149].

In 2015 Peng et al. [150] used intraprocedural CEUS to monitor HIFU treatment of uterine fibroids. Figure 3 clearly shows the development of an ablated zone as treatment progresses. In many studies the ablated volume is defined as the non-perfused region observed on post-treatment contrast enhanced MRI. In the study by Peng et al. there was no statistical difference between the non-perfused volume determined by CEUS immediately post-treatment and that found using MRI the following day. In an earlier study by Kennedy et al. [151] the ablated region identified by CEUS was confirmed via histologic analysis. CEUS has also been shown to perform at least as well as MRI and CT in the follow-up of patients treated for liver tumors by RFA [152]. Intraoperative CEUS offers a simple, effective, low cost method of monitoring thermal ablation. In comparison to temperature-based methods, it does not rely on the Arrhenius model. The advantage of CEUS was demonstrated by Solbiati et al. who noted that the introduction of CEUS resulted in a drop in the rate of partially ablated liver tumors from 16.1% to 5.9% [149].

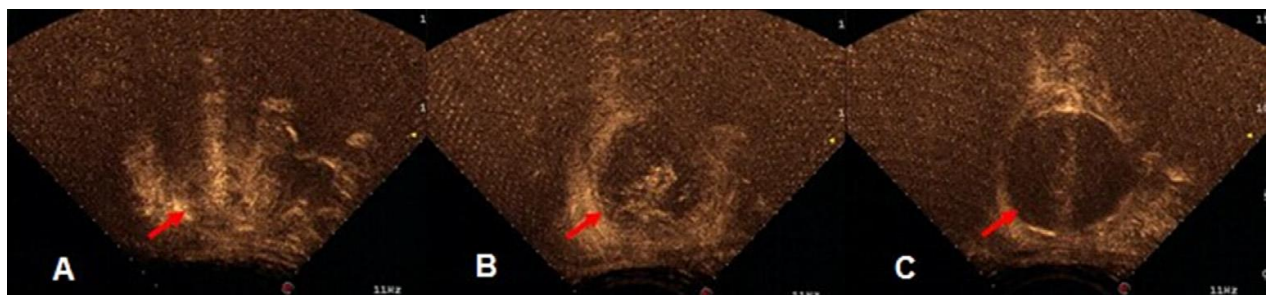


Figure 3: CEUS of uterine fibroid before(A), during (B) and after HIFU treatment (C) [150]

## 2.6.2. Elastography

Elastographic techniques aim to map a tissue's Young's modulus ( $E$ ), analogous to the palpation techniques long employed by clinicians when diagnosing tumors. Ablated tissue tends to be stiffer thus elastography can estimate the extent of ablation [105], [153], [154]. Ultrasound and MRI based elastography have been developed.

Ultrasound elastography can be divided into two categories: static methods and dynamic methods. In static elastography a constant stress is applied to the tissue and resulting displacement is recorded. Strain can then be calculated; thus, providing a strain map called an elastogram. The Young's modulus cannot be found as the applied stress is unknown.

In dynamic methods either ultrasound radiation pressure or an electro-mechanical actuator is used to induce shear waves in the tissue. By measuring the speed of propagation of these waves one can calculate the shear modulus ( $\mu$ ) which is directly related to the Young's modulus ( $E = 3\mu$ ) [155]. Dynamic methods suffer due to the presence of both compressive and shear waves within the imaged medium. To combat this transient elastography was developed which naturally separates these waves by tracking the shear waves induced by a short high intensity pulse [155].

### Vibroacoustography

Vibroacoustography (VA) is a dynamic elastography method which was introduced by Fatemi and Greenleaf in 1998 [156], [157]. It uses two confocal beams with slightly different center frequencies to cause a target to vibrate at a specified frequency. Mechanical properties of the target, including stiffness, can be determined by listening to the resulting sound. An image can be created by sweeping the focal spot across the

region of interest. Sweeping leads to an extended acquisition time which may prove problematic for *in vivo* applications, particularly where real-time imaging is required [155].

VA has been shown to be capable of quantifying lesion size post HIFU in an *ex vivo* animal study [158]. It has also been successful in identifying the frozen tissue induced during *ex vivo* prostate cryotherapy [159]. Although it has not been clinically demonstrated, evidence in the literature suggests that transrectal vibroacoustography is capable of delineating structures and anatomical zones within the prostate [160].

### **Acoustic Radiation Force Impulse Imaging**

In contrast to vibroacoustography, acoustic radiation force impulse imaging (ARFI) is a transient elastographic technique. It was developed by Nightingale et al. in 2001 [161], [162]. ARFI uses a single focalized ultrasound beam to cause tissue displacement via a short duration (<1ms) high intensity acoustic pulse. The transducer then switches to imaging mode to detect displacements of the focal spot. Like VA, a 2D image can be acquired by sweeping the focal point across the ROI. Although this technique is safe, it has been shown to induce localized tissue heating [163]. Young's modulus is not directly quantified, instead it is estimated by measuring parameters such as displacement and relaxation times [155].

Fahey et al. demonstrated that ARFI can be used to monitor ablation in real time [164]. In that study RFA was performed *in vivo* on ovine myocardial tissue under ARFI surveillance. It was found that ARFI is capable of determining lesion location, shape and size during the procedure. In a follow up study by Eyerly et al. it was found that ARFI can visualize RFA induced lesion dimensions with less than 2mm error [165]. Bing et al



demonstrated that HIFU and ARFI imaging can be accomplished with the same ultrasound transducer [166]. Custom beam sequences were used to identify the target, induce hyperthermia and monitor the formation of the resulting ablation lesion. Fahey et al demonstrated ARFI during liver RF ablation in 5 patients [167]. Kwon et al. performed a similar study in 38 patients [168]. ARFI has been commercialized by Siemens Medical Solutions and is available on their ACUSON S2000™ in the Virtual Touch™ tissue Imaging tool.

### **Supersonic Shear Imaging**

Supersonic shear imaging (SSI) was pioneered by Bercoff et al. in 2004 [169] The technique builds on pioneering work by Armen Sarvazyan who previously developed shear wave elasticity imaging (SWEI) [170]. SSI uses focused ultrasound beams to produce sources of mechanical vibration within tissue. These sources emit low frequency shear waves. By moving the source at speeds greater than the speed of sound, two intense plane shear waves are created via constructive interference. This is analogous to the “sonic boom” created by supersonic aircraft. The propagation of these waves is recorded using an ultrafast scanner which can acquire images at 5000 frames/s. Inversion algorithms are then used to create a shear wave elasticity (SWE) map of the analyzed medium [169], [171].

Mariani et al. demonstrated the use of SSI for monitoring RFA [172]. 29 *in vivo* thermal lesions were induced in porcine liver. The liver mean elasticity increased from  $6.4 \pm 0.3$  kPa before RFA to  $38.1 \pm 2.5$  kPa post-ablation. Using a threshold of 20 kPa this technique correctly identified necrosis with a positive predictive value of 0.83 and a sensitivity of 0.8. In contrast, an expert radiologist failed to clearly delineate the induced

thermal lesion in 70% of cases using B-mode guidance. The contrast between the two methods is clearly elucidated in Figure 4 below. SSI is now available on the Aixplorer® system by SuperSonic Imagine but does not appear to have been used clinically for monitoring ablative therapy.

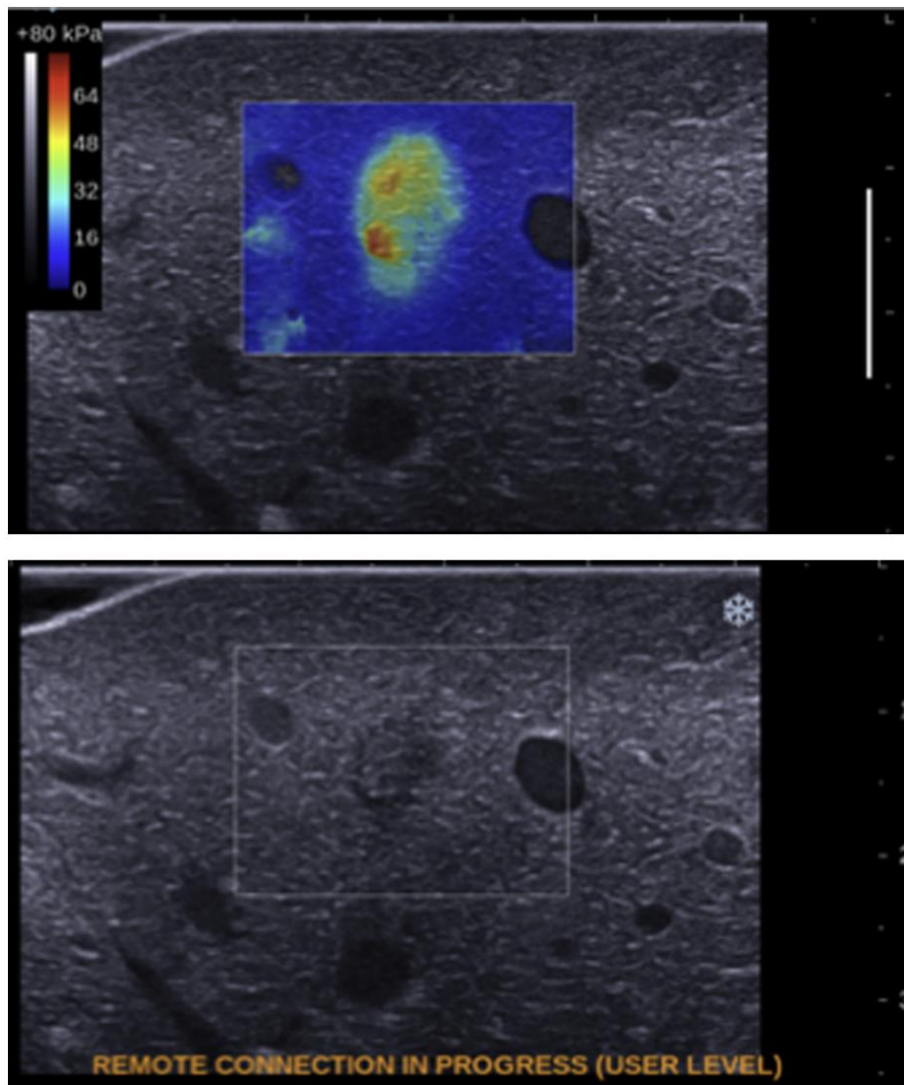


Figure 4: Shear wave elasticity map (Top) and B-mode image (bottom) obtained after creation of a thermal lesion in porcine liver [172]. SWE identifies the lesion as a region of increased stiffness.

## Harmonic Motion Imaging

In contrast to other elasticity imaging techniques Harmonic Motion Imaging (HMI) induces a spatially invariant internal vibration within the target via an amplitude-modulated waveform. Tissue mechanical properties can then be derived by analyzing the dynamic tissue response [173]. Harmonic Motion Imaging for Focused Ultrasound (HMIFU) combines this technique with HIFU providing real-time synchronous monitoring of temperature-induced alteration of tissue mechanical properties [174]. This technique was successfully demonstrated in *ex vivo* porcine liver where the onset of coagulation was found to coincide with irreversible change in tissue mechanical properties [175]. A post-ablation increase in tissue stiffness was observed as has been described in previous works [153].

Similar results were found in an *in vivo* study using rabbit muscle [176]. In this study the ability to linearly scan a target region to identify the extent of coagulation was demonstrated. This technique has also been successfully demonstrated *in vivo* in transgenic breast cancer mouse [177]. Moreover, a recent *in vitro* study by Han et al. found good agreement between the depth ( $r^2 = 0.81$ ), width ( $r^2 = 0.85$ ) and area ( $r^2 = 0.75$ ), quantified via HMI and gross pathology [178]. The study was performed using HIFU on a canine liver. While existing literature focuses on the combination of HMI with HIFU, the technique could potentially be used with any ablation modality.

## Magnetic Resonance Elastography (MRE)

MRE has been shown to provide accurate measurements of lesion size when compared to pathology. MRE involves applying a known force to the tissue and imaging the

resulting shear waves as they propagate through the tissue [179]. Moreover, It is feasible to measure temperature and stiffness simultaneously using MRE techniques [180].

Chen et al. demonstrated that MRE is capable of measuring stiffness changes induced by FLA [181]. In that study FLA was performed *in vivo* on porcine liver. A novel inertial acoustic driver was used to induce mechanical waves enabling tissue stiffness to be determined before, during and after FLA. Figure 5 shows elastograms obtained before (a) and after (b) FLA was performed for 2min at 15 W. The increase in tissue stiffness is clearly depicted in Figure 5 (C) along a profile through the ablation zone. As yet MRE has not been used clinically to monitor ablation.

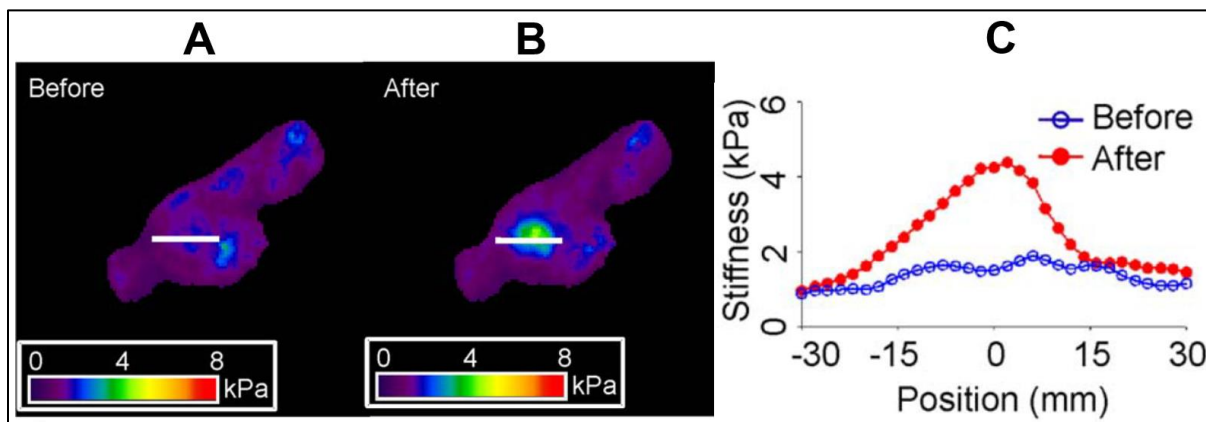


Figure 5: MR elastograms obtained before (A) and after (B) a 15 W laser application for 2min in porcine liver. The change in stiffness along a profile through the ablation zone (C) [181].

### 2.6.3. Optical Monitoring

The techniques outlined in this section take advantage of thermally induced changes in tissue optical properties. While these techniques may appear complex in nature, the underlying principle is akin to visualizing the difference between raw and cooked meat. In contrast to the previous techniques in this section, optical monitoring requires line-of-sight access and therefore interstitial probes must be used.

## **Diffuse Optical Spectroscopy**

Diffuse Optical Spectroscopy requires an interstitial fiber optic needle which is used to emit a spectral band of light and record the diffuse reflectance or fluorescence. Thermal ablation has been shown to increase reflectance intensity and decrease fluorescence intensity. Anderson et al. monitored both fluorescence and diffuse reflectance during canine hepatic RFA and demonstrated a correlation between thermal damage and the absolute magnitude of spectral change [182]. Similar results were reported by Buttemere et al. [183] and Hsu et al. [184]. In contrast to thermal monitoring, spectral changes persist after cooling thus margins can be interrogated both during treatment and immediately afterwards.

Spliethhoff et al. argued that the absolute spectral intensities are sensitive to needle positioning, pooling of coagulated blood and instrument calibration [185]. In an effort to create a more robust method they proposed the use of an optical ablation ratio (OAR). The OAR is based on a first-order derivative analysis of the diffuse reflectance signal. In a follow-up study by the same group, 8 patients received RF ablation for the treatment of unresectable liver metastases [186]. Spectra were acquired using two different source-detector separation distances denoted long distance (LD) and short distance (SD). As shown in Figure 6, there was a significant increase in the OAR value between native and ablated tissue for both configurations ( $p < 0.01$ ).

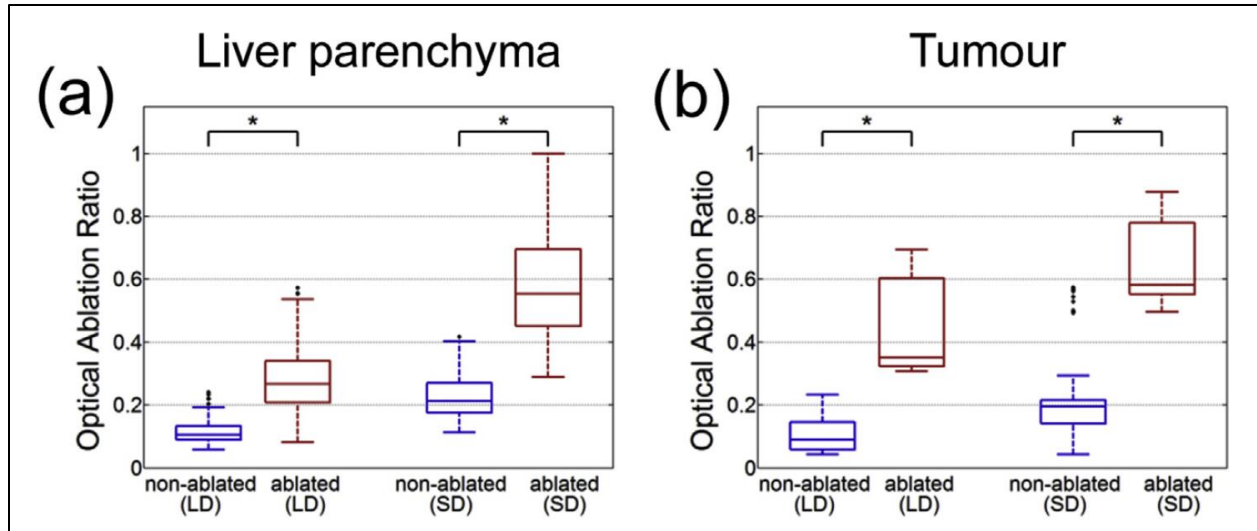


Figure 6: Optical ablation ratio in liver parenchyma (a) and liver metastases (b) before and after RF ablation. Data acquired from 8 patients. Figure adapted from Tanis et al. [187].

### Interstitial Point Optical Measurements

Whelan et al. demonstrated a method of monitoring FLA by placing an interstitial fiber optic sensor at a distance from a source fiber and recording the optical intensity during laser activation [188]. A 49% decrease in optical intensity was observed by an optical detection fiber placed 5mm from the source during FLA of *in vivo* porcine kidney. Similar results were observed for *ex vivo* bovine tissue where the optical intensity decreased by up to 83%. The decrease in optical intensity is attributed to an increase in the reduced scattering coefficient as a result of tissue coagulation. Further work by the same group supports this approach [189]-[191]; however, as yet the correlation between the optical signal and thermal damage has not been verified using histologic analysis of the induced thermal damage. While this technique is being investigated for use with FLA, it may be possible to monitor RFA and MWA by incorporating a low power light source into the ablation probe.

Assessment of the interaction between light and tissue requires an unimpeded line-of-sight; therefore, interstitial probes are a necessity. As with interstitial thermal probes, multiple probes are required to monitor ablation throughout a volume. Both of these requirements leave optical monitoring at an inherent disadvantage to techniques previously outlined in this section which rely on ultrasound and MRI. Further research is necessary to demonstrate the clinical utility of optical methods of monitoring ablation. If successful, this approach is likely to offer a lower cost solution than both ultrasound and MR elastography. Moreover, optical techniques can be implemented in a similar manner to interstitial thermal probes and have two potential advantages. Firstly, the change in optical signal persists after cooling thus allowing for confirmation of the coagulation zone immediately after ablation. Secondly, optical techniques do not require damage estimation models such as the Arrhenius and TID model.

## **2.7. Discussion & Conclusions**

HIFU, RFA, MWA and FLA have all been demonstrated as effective methods of inducing coagulative necrosis within target tumors. While the technology for energy delivery has advanced in recent years, there is a growing need for improved thermal ablation. This is illustrated in a clinical trial in which 27 men received FLA for the treatment of prostate cancer [192]. A 12-month follow-up biopsy found cancer in 10 patients, 3 of which had cancer within the ablation zone. Similar results were found by our group, where a 6-month biopsy identified cancer within the ablation zone of 3 of the 8 treated patients [73]. Cancer was also found immediately outside the treated zone in 6 patients. These results demonstrate that FLA can successfully induce coagulative necrosis within the target. However, in the absence of accurate real time monitoring it is difficult to ensure

that thermal necrosis has been induced throughout the entire target while minimizing damage to surrounding structures.

In this review paper we have outlined possible methods of controlling treatment to ensure efficacy. These methods can be divided into 2 categories: (1) thermal dosimetry and damage estimation, (2) non-thermal feedback techniques. Table 2 summarizes the available approaches to thermal dosimetry. Interstitial electric probes (thermistors and thermocouples) and optical probes (fluoroptic probes and fiber Bragg grating) appear to be the most promising invasive temperature-based feedback systems due to their small size, high accuracy and fast response. While thermocouples are widely used, particularly in RFA, these sensors suffer from self-heating and conduction errors. Furthermore ‘viscous heating’ artificially inflates temperature measurement when used with HIFU. They are also not MR-safe which can be a major disadvantage given that many ablation procedures are performed under MR surveillance. Thermocouples are often integrated into RFA and MWA applicators and can also be placed interstitially via catheters to provide efficacy feedback and to monitor critical structures. Thermistors suffer from similar issues but are not available in such a small form factor and thus are less popular than thermocouples. Interstitial electric probes have found clinical utility in MWA, RFA and FLA. Unsurprisingly, these probes have not been utilized clinically with HIFU as they negate one of the key advantages of HIFU i.e. its non-invasive nature.

Fiber-optic probes are similar to electric probes with the advantage that they are inherently MR safe. MR safety is an important characteristic as many ablation procedures rely on MRI for probe guidance. Unfortunately, fiber optic probes are expensive which compounds the already high cost associated with MRI. Fluoroptic probes have been used in many studies; however, like electrical probes they only provide a ‘point’ measurement.



When used to monitor FLA, self-heating and artifacts from laser light entering the fiber can degrade temperature recording. FBG sensors have the potential to solve all three of these issues. FBGs are capable of distributed sensing in a single fiber and are not susceptible to artifacts as they do not use the same wavelength as lasers used in FLA. High equipment cost and to a lesser extent the need to prevent strain have thus far limited the use of FBGs in a clinical setting.

Table 2: Methods for monitoring ablation based on temperature measurement including current clinical application and limitations of each method

Method	HIFU	MWA	RFA	FLA	Primary Limitations
<b>Thermography</b>					
Liquid Crystals					Surface measurement only
Infrared Imaging					Surface measurement only
Microwave					Poor spatial & temporal resolution
<b>Electrical Probes</b>					
Thermistors		✓	✓	✓	Interstitial point measurement, large size
Thermocouples		✓	✓	✓	Interstitial point measurement
<b>Fiber-optic Temperature Sensors</b>					
Fluoroptic Probes		✓	✓	✓	Interstitial point measurement
Fiber Bragg Grating					Interstitial point measurements, strain corrupts measurement, high cost
<b>Radiologic Imaging</b>					
Acoustic Thermometry	✓				Inaccurate above 50°C
Magnetic Resonance Thermometry	✓	✓	✓	✓	High cost, motion artifact
CT Thermometry					Ionizing Radiation

PRF shift based MR thermometry represents the most promising non-invasive method of recording temperature. It has been successfully utilized in numerous studies; however, it presents several weaknesses. The most important of which are the need for MR-safe equipment and a motionless target. It also suffers from poor temporal resolution as well as greatly increasing the cost of ablative therapy.

Given that ablation induces cellular destruction via temperature elevation, it is unsurprising that traditional monitoring systems are based on temperature measurement. This approach appears sufficient when the goal is to ensure safety by ceasing therapy if the temperature of sensitive structures outside the target approaches lethal levels. When optimizing efficacy, such methods may be insufficient as the relationship between thermal history and cellular destruction remains somewhat ill-defined. The Arrhenius model has been widely used for this purpose. It relies upon knowledge of two elusive parameters: the pre-exponential factor and the activation energy. Parameters from the literature provide wildly different estimates of cellular destruction for the same thermal history. For this reason, non-thermal feedback techniques may have greater utility. Moreover, it should be noted that HIFU induces cellular damage through both heat and cavitation, the latter of which is not accounted for in the Arrhenius model.

Table 3 summarizes the current methods of monitoring ablation without recording temperature. The three approaches in this category are: ultrasound imaging, elastography and optical monitoring. In conventional B-mode ultrasound imaging the ablation zone appears as a hyperechoic region. This has been observed clinically for all forms of ablative therapy; however, due to poor margin identification, B-mode imaging is insufficient as a monitoring method. Nakagami imaging has been shown to improve

margin estimation using the same conventional ultrasound systems as B-mode imaging. Nakagami imaging is a very recent development and its clinical utility has not yet been demonstrated. CEUS is another effort to improve visualization of the ablation zone without changing the ultrasound system. It involves the injection of microbubbles into the vasculature to enable assessment of perfusion via Doppler ultrasonography. CEUS is capable of identifying lesions that are characterized by increased perfusion. In addition, it can be used to monitor the growth of the ablation zone as the ablation process involves the destruction of vasculature within the target, thus decreasing perfusion. CEUS is simple, low cost and results show that the estimated damage zone corresponds to estimates acquired via histology and MRI; however, it cannot be used for continuous real-time monitoring.

Elastography offers an alternative approach to conventional ultrasound. Physicians have long identified tumors via manual palpation as tumors are often associated with unusual mechanical properties, in particular increased stiffness. In addition, ablation induced coagulative necrosis results in an increase in stiffness. Elastography aims to quantify a tissue's Young's modulus and can thus be used to both identify the tumor and monitor the ablation process. This change in mechanical properties can be quantified using US elastography or magnetic resonance elastography. To date, clinical application of elastography is very limited. ARFI and SSI have been commercialized by Siemens Medical solutions and SuperSonic Imagine respectively; however, only the former has been clinically demonstrated as a method for monitoring ablation. A general disadvantage of all elastographic techniques is the requirement for the development of specialized equipment. Consequently, the barrier to clinical entry is higher for these techniques in comparison to Nakagami Imaging and CEUS. Widespread

clinical application of these techniques will not occur until the clinical benefits are proven to outweigh the additional cost. Magnetic resonance elastography is at a particular disadvantage due to the high costs associated with MRI.

Table 3: Methods for monitoring ablation that do not require temperature measurement including current clinical application and primary limitations of each method

<b>Method</b>	<b>HIFU</b>	<b>MWA</b>	<b>RFA</b>	<b>FLA</b>	<b>Primary Limitations</b>
<b>Ultrasound Imaging</b>					
B-mode imaging	✓	✓	✓	✓	Poor margin identification
Nakagami Imaging					Unproven
Contrast Enhanced Ultrasound	✓	✓	✓	✓	Not real time
<b>Elastography</b>					
Vibroacoustography					Requires specialized equipment, long acquisition time
Acoustic Radiation Force Impulse Imaging			✓		Requires specialized equipment
Supersonic Shear Imaging					Requires specialized equipment
Harmonic Motion Imaging					Requires specialized equipment
Magnetic Resonance Elastography					High cost
<b>Optical Monitoring</b>					
Diffuse Optical Spectroscopy			✓		Interstitial point measurement
Interstitial Point Optical Measurements					Interstitial point measurement

Optical monitoring aims to differentiate coagulated tissue from native tissue based on thermally induced changes in tissue optical properties. The technique requires the insertion of fiber optic probes into an area of interest such as the intended ablation margin. The contrast mechanisms for Diffuse Optical Spectroscopy are an increase in

reflectance intensity and a decrease in fluorescence intensity, both of which occur as a result of thermal coagulation. This approach has been demonstrated clinically for monitoring RFA of liver metastases. In contrast Interstitial Point Optical Measurements identify thermal coagulation due to an increase in scatter which results in a decrease in optical intensity measured by a probe placed at distance from the light source. This technique is particularly useful for monitoring FLA but could be used for RFA or MWA by integrating a light source into the respective probes. Development of optical monitoring techniques is very much in its infancy; hence, the dearth of clinical utilization.

In conclusion, accurately controlling ablation procedures remains challenging. Temperature measurement is the most widespread approach for real-time monitoring of ablative therapy; however alternative approaches are under development. The increasing popularity of HIFU is likely to lead to increased efforts to develop US elastography. Likewise, the desire for minimally invasive interventions to replace traditionally invasive procedures, such as radical prostatectomy, may provide the impetus for further development of interstitial probes. Finally, while MRI is capable of both guiding interstitial probes and monitoring thermal damage (MRT and MRE), the high associated cost is likely to prohibit large scale adoption. Regardless of ablative modality, it is clear that future ablation techniques must include a method of feedback and confirmation to ensure reproducible clinical success.

# CHAPTER 3

## Focal Laser Ablation with Interstitial Thermal Probe Monitoring

### 3.1. Introduction

Focal laser ablation is a promising minimally invasive approach for the treatment of prostate cancer. Many groups have successfully performed FLA under MRI surveillance [6], [9]-[11]. For example, Walser et al reported a significant decrease in PSA score ( $P < 0.01$ ) in 120 patients that received FLA for low- to intermediate-risk prostate cancer [6]. The total procedure time ranged from 60-250 minutes with a median of 122 minutes while laser ablation time ranged from 2.5-40 minutes with a median of 12.6 minutes. Over 24 months follow-up, clinically significant disease was found via biopsy in 15% of patients. The most common adverse events were hematuria (7.4%), erectile dysfunction (5.0%) and urinary retention (4.1%) with one patient experiencing a grade three adverse event (urinary tract infection). Similar results were found in our own in-bore clinical trial: PSA decrease ( $P < 0.01$ ), no grade three adverse events, clinically significant cancer in the treated area in 3 of 8 men, mean procedure time 4.9 hours [73]. This experience led us to identify the need for MRI surveillance as a critical barrier to the widespread adoption of FLA. MRI is inherently expensive and the reduced access to the patients exacerbates the already cumbersome nature of FLA leading to lengthy procedure times.

MRI performs two key functions: 1) to guide the laser fiber to the target, and 2) to monitor treatment progress via MR thermometry. We hypothesized that MR-US fusion guidance and interstitial thermal probes could be used for guidance and treatment monitoring respectively. MR-US fusion guidance facilitates targeting by co-registering regions of interest acquired via MRI with real-time ultrasound imaging. Consequently, the both the procedure cost and complexity are substantially decreased as it can be performed in a urology clinic rather than an MRI suite. In addition, the number of personnel is reduced as the procedure does not require an MR technologist or a radiologist. MR-US fusion biopsies are routinely performed at UCLA with procedure times less than 30 minutes. Given the ease with which a biopsy needle can be guided to ROIs defined by MRI, it is reasonable to assume that a laser fiber could be guided to an ROI defined by both MRI and biopsy data. By using a needle guide, interstitial thermal probes could be placed at known location to both monitor treatment progress and ensure safety. In contrast, to MR thermometry, thermal probes are not adversely affected by patient motion which was found to substantially impact thermal dosimetry in our in-bore trial.

MR-US fusion guidance and interstitial thermal probes were previously used for monitoring FLA by Lindner et al. [193]. In that study, 12 patients received FLA for low-grade CaP. The laser fiber and thermal probes were inserted transperineally and treatment was verified with microbubble contrast. At 6-month follow-up biopsy, 67% of patients were cancer free in the treated zone. In this chapter, we will outline our clinical trial which represents the first clinical experience of MR-US fusion guided transrectal FLA monitored solely via interstitial thermal probes. Given the novel nature of this trial, we applied for and received an Investigational Device Exception from the FDA. The

primary goal of the trial was to demonstrate the feasibility and safety of MR-US fusion guided FLA monitored via interstitial thermal probes. In this chapter, we will summarize the clinical trial, compare results against our in-bore clinical trial and critically analyze the utility of interstitial thermal probes as a modality for monitoring FLA.

## 3.2. Materials and Methods

The clinical trial required the use of a diverse range of hardware:

**Laser Ablation system** (Visualase, Medtronic) - The Visualase system (Figure 7A) is an FDA approved laser ablation system consisting of a peristaltic pump (K-pump, Kolster Methods), a 980nm laser (PhoTex15, Biotex) and dual lumen catheter (Medtronic). This is the same system that was used by many groups including ours for MR-guided FLA.

**Ultrasound System** (Nobulus, Hitachi) - The Nobulus ultrasound system (Figure 7) with the C41V transrectal ultrasound probe provide real-time prostate and applicator visualization.

**MR-US Fusion Device** (Artemis, Eigen, CA) - The Artemis system (Figure 7C) performs non-rigid registration of MRI data with real-time ultrasound.

**Fiber Optic Thermometry System** (Luxtron, Lumasense) - The Luxtron system (Figure 7D) is an FDA approved temperature measurement system capable of measuring temperature using Fluoroptic technology (Figure 8). The temperature measurement is based on the decay rate of a phosphor element embedded at the tip of an optical fiber.

**Custom Needle Guide:** The needle guide (Figure 7D) contains a central 13GA channel and 15Ga channel for the dual lumen catheter and a single interstitial thermal probe respectively. The two channels are parallel and 8mm apart.



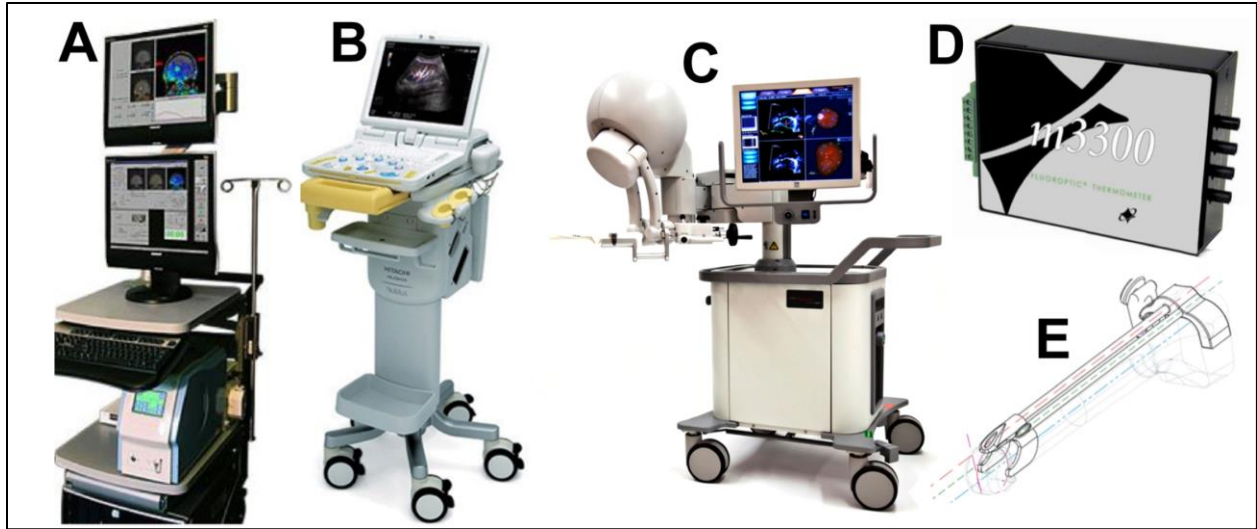


Figure 7: Key hardware used in MR-US fusion guided FLA: A) Visualase system, B) Nobulus ultrasound system C) Artemis MRI-US fusion system, D) Luxtron Fiber Optic Thermometry system, E) Needle guide

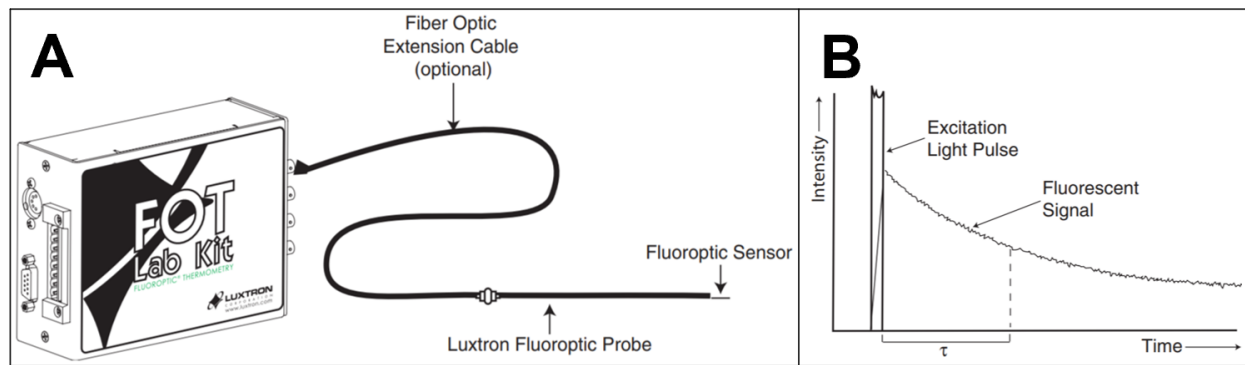


Figure 8: A) Luxtron system with one of four fluoroptic probes attached. B) Fluoroptic technology – thermal measurement is based on the decay rate of a phosphor element embedded at tip of the probe

### 3.2.1. Treatment Planning

The size of the ablation is dependent on multiple factors such as the laser wavelength, exposure duration, power and diffuser size. The wavelength and diffuser size are fixed at 980nm and 15mm respectively due to the equipment provided with the Visualase system. The power and exposure duration were set to 13.75W and 3 minutes based on prior clinical experience. Finally, the location of the diffuser within the dual lumen

catheter can also alter the ablation zone; therefore, this was fixed as shown in Figure 9. Note that the laser fiber cannot be inserted to the end of the dual lumen catheter as to do so would impede the flow of saline necessary to cool the fiber. Based on preclinical testing in ex vivo bovine muscle, it was assumed that each laser activation would result in an elliptical ablation zone with major and minor axes of 24mm and 17mm respectively (Figure 9). The major axis is greater than the length of the diffuser as light is emitted both radially and longitudinally.

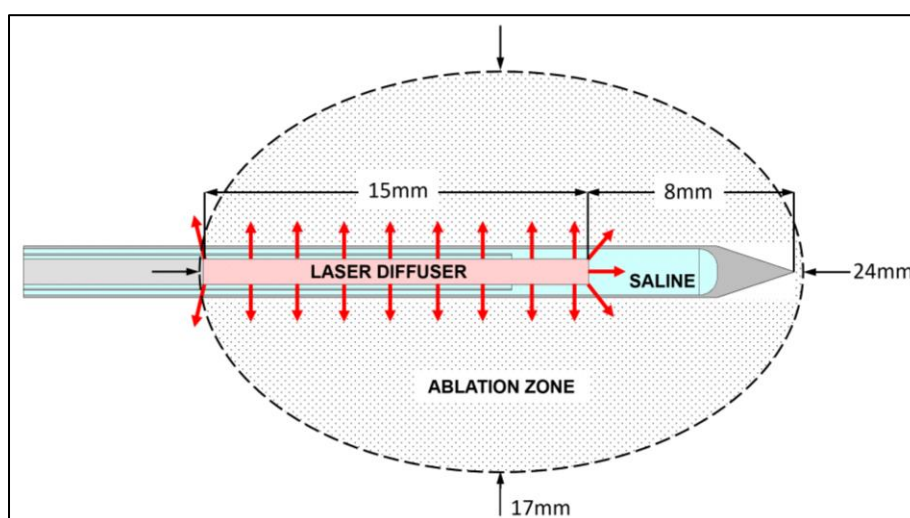


Figure 9: Ablation zone used for treatment planning. Red arrows indicate light emission from the diffuser

Patient specific treatment plans were created based on diagnostic MRI and biopsy. During biopsy procedures performed at UCLA, the location of each ROI and biopsy core are stored in 3D on the fusion device. This data was then combined with the MRI derived ROI to ascertain the size and location of the requisite ablation zone (Figure 10A). To ensure treatment throughout the entire zone, ablation zones from individual laser activations were superimposed onto this prostate model. The final plan contains the number and location of each laser activation including the fiber trajectory and orientation. The laser

fiber is inserted through a needle guide which contains a parallel channel for a thermal probe. As a result, the orientation of the fiber must be set to optimize the position of the thermal probe. During consecutive overlapping laser activations, it is preferable to position the thermal probe in previously untreated tissue. This is necessary as laser-tissue interaction changes considerably between native and coagulated tissue; therefore, the thermal response in a previously treated zone does not reflect that in the untreated zone.

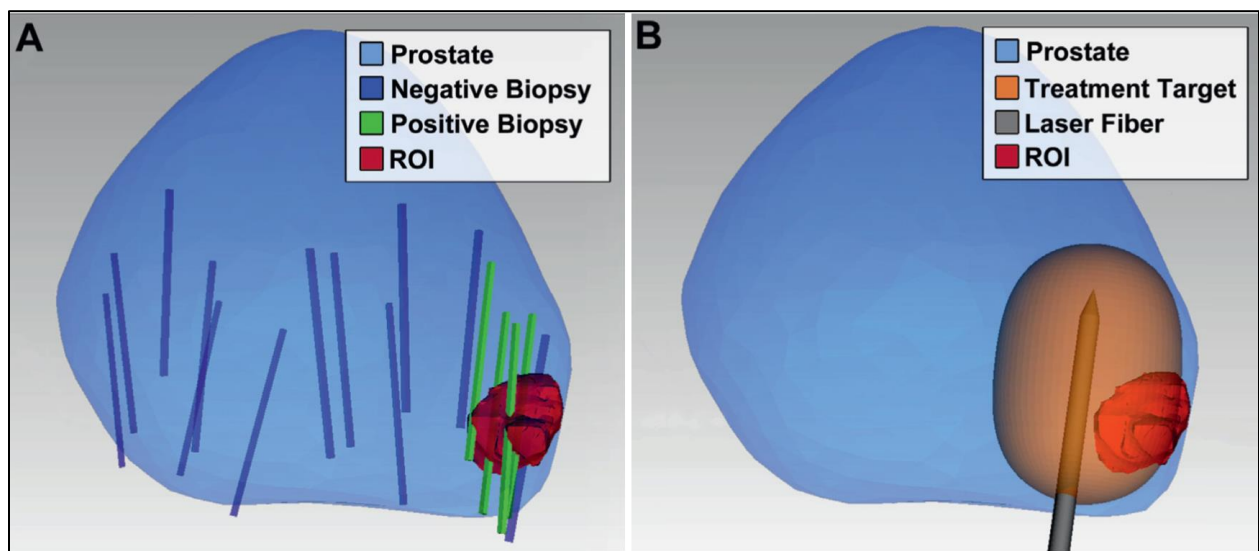


Figure 10: A) MRI derived ROI fused with biopsy data to create patient specific treatment plan. B) Treatment plan showing the requisite laser fiber trajectory

The final setup is shown in Figure 11A which also includes three transperineally inserted interstitial thermal probes (ii-iv). These probes consist of a 15Ga flexi-needle containing a single fluoroptic probe. One of these probes, designated 'rectal monitor', was always located between the laser fiber and the rectal wall to preserve this sensitive structure and prevent a rectal fistula which is classified as a serious adverse event. The other two probes were inserted at the physician's discretion and were typically placed

next to the lateral capsule and the urethra. The interstitial thermal probe, designated 'efficacy probe', was inserted through the needle guide and positioned level with the laser fiber tip and at a radial distance of 8mm (Figure 11B). The orientation of the ultrasound probe was defined in the treatment plan to ensure that this probe always lies within the prostate and where possible in untreated tissue when performing overlapping ablations.

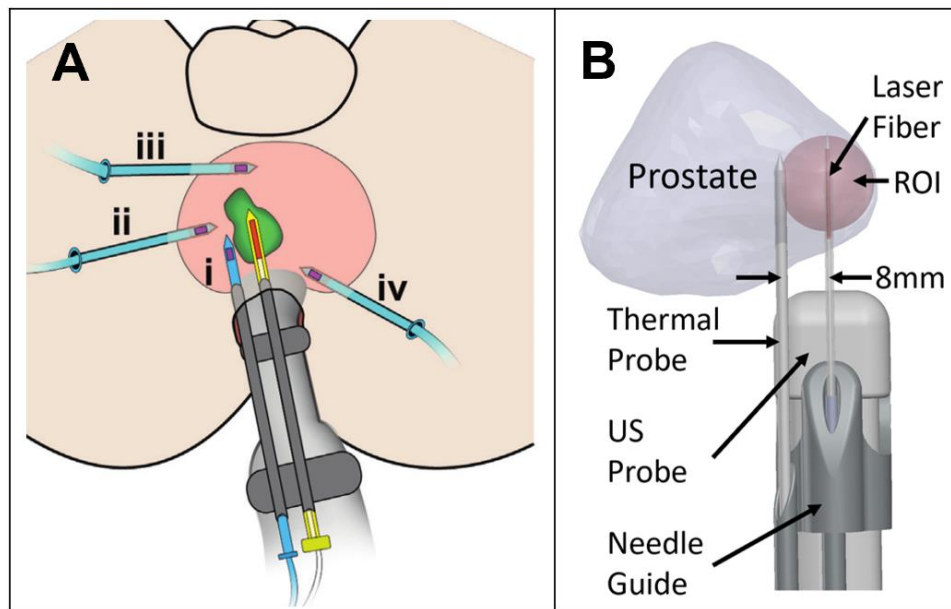


Figure 11:A) Setup for MR-US fusion guided focal laser ablation. Treatment is monitored with one transrectal thermal probe (i) and up to three transperineally inserted thermal probes (ii-iv). B) Detailed view of transrectal ultrasound probe with needle guide, laser fiber and thermal probe. The laser fiber is housed in dual lumen catheter that flows saline around the fiber to prevent charring. The thermal probe consists of a single Luxtron fluoro optic probe housed in a 15Ga flexi-needle.

### 3.2.2. Treatment Protocol & Follow-up

To minimize pain and discomfort patients were sedated with ketorolac (30mg) and midazolam (4mg) and a periprostatic nerve block consisting of a 50-50 mixture of bupivacaine and 1% lidocaine was administered with the patient in the left lateral

decubitus position. Patients then transitioned to the lithotomy position for transperineal insertion of interstitial thermal probes, including the rectal monitor. Probe insertion was verified using a side firing transrectal ultrasound probe. The patient was subsequently returned to the lateral decubitus position and a 3D ultrasound scan was performed with an end-fire transrectal ultrasound probe and the fusion device. The treatment plan was then imported and fused with the real-time ultrasound image by the fusion device.

The ultrasound probe was then aligned to the trajectory defined in the treatment plan to facilitate insertion of the laser fiber through the main channel of the needle guide. A 13Ga open ended catheter was inserted using a biopsy needle as a trocar. Advancement of the needle was monitored via ultrasound in an effort to ensure that it was positioned at the correct depth. The needle was then removed and the dual lumen catheter was advanced through the 13Ga catheter with laser fiber ultimately positioned 5mm shallow of the catheter tip. Finally, the efficacy probe was advanced through the secondary channel in the needle guide and aligned with the tip of the laser fiber. Over time the procedure evolved with the introduction of an echogenic biopsy needle greatly enhancing visualization resulting in improved positioning of the dual lumen catheter.

Each laser activation was performed at 13.7W for up to 3 minutes under active cooling from the peristaltic pump. Laser activation was terminated prematurely if the rectal monitor indicated rapid temperature rise or if it exceeded 42°C. This protocol was followed to prevent damage to the rectal wall which may lead to a rectal fistula which is defined as a serious adverse event.

Following treatment, patients were transferred to an MRI suite and underwent multiparametric MRI. Dynamic contrast enhanced MRI was performed to facilitate identification of the ablation zone as a region of non-perfused tissue. Patients were then

discharged with follow-up PSA tests and questionnaires at 3 months. In addition, multiparametric MRI and biopsies were performed at 6 and 12 months to assess treatment efficacy.

### 3.3. Results

A total of 11 men were enrolled in the study, one of whom did not receive FLA due to difficulties encountered during flexi-needle insertion. The mechanical properties of the prostate were compromised by a prior transurethral resection resulting in the inability to correctly anchor flexi-needles at the correct location. For the first 4 men, the dual lumen catheter was placed using a standard biopsy needle which proved to be difficult to monitor via the end-fire transrectal ultrasound probe. Consequently, it was replaced with a biopsy needle containing an echogenic tip which was easily tracked on ultrasound. Interestingly, this problem did not arise when visualizing the transperineal thermal probes (Figure 12) due to their angle of insertion relative to the imaging plane.

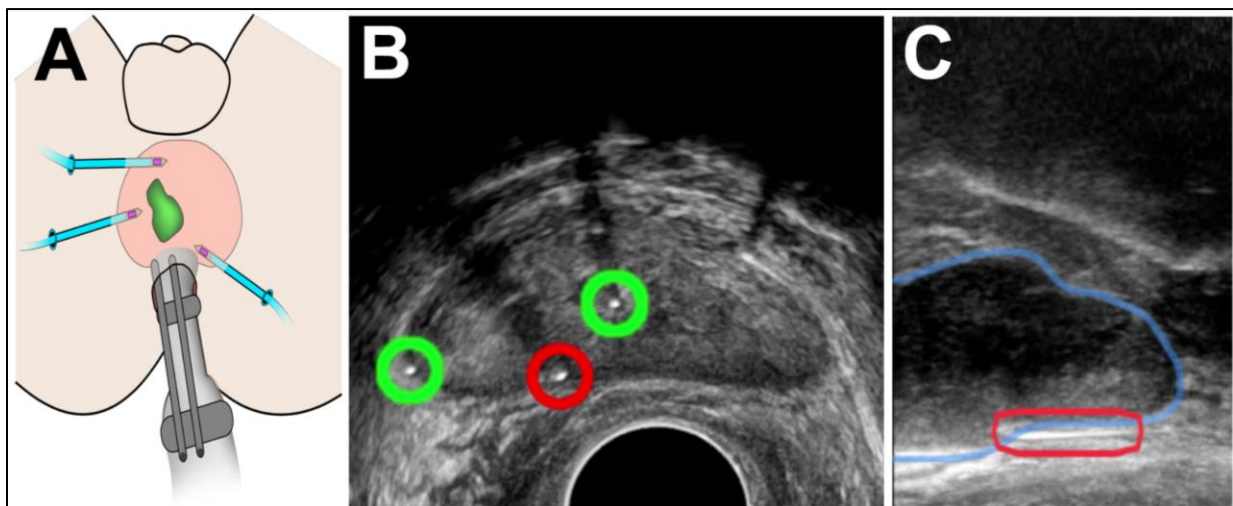


Figure 12: A) Illustration depicting the insertion of transperineal thermal probes under US guidance. B) Probe positioning on transverse imaging plane. Note the rectal monitor highlighted in red. C) Rectal monitor location in sagittal imaging plane.

In the 10 treated patients the laser was activated a 13.75W for an average of 144 seconds and mean total procedure time of 95 minutes (range 71-105). Figure 13 shows an example of the data from the thermal probes and the corresponding ablation zone. In this patient, the laser was activated twice with high temperatures recorded by the ‘efficacy probe’ (probe 4) while the rectal monitor (probe 1) remains at approximately body temperature. As expected, the ablation zone identified on MRI extends as far as the efficacy probe while the rectal wall appears intact. Similar results were seen in all 10 patients with the ablation zone consistently confined within the prostate capsule leaving the rectal wall intact (Figure 14). A total of 38 grade 1 and 6 grade 2 adverse events were recorded with short term hematuria the most frequently reported.

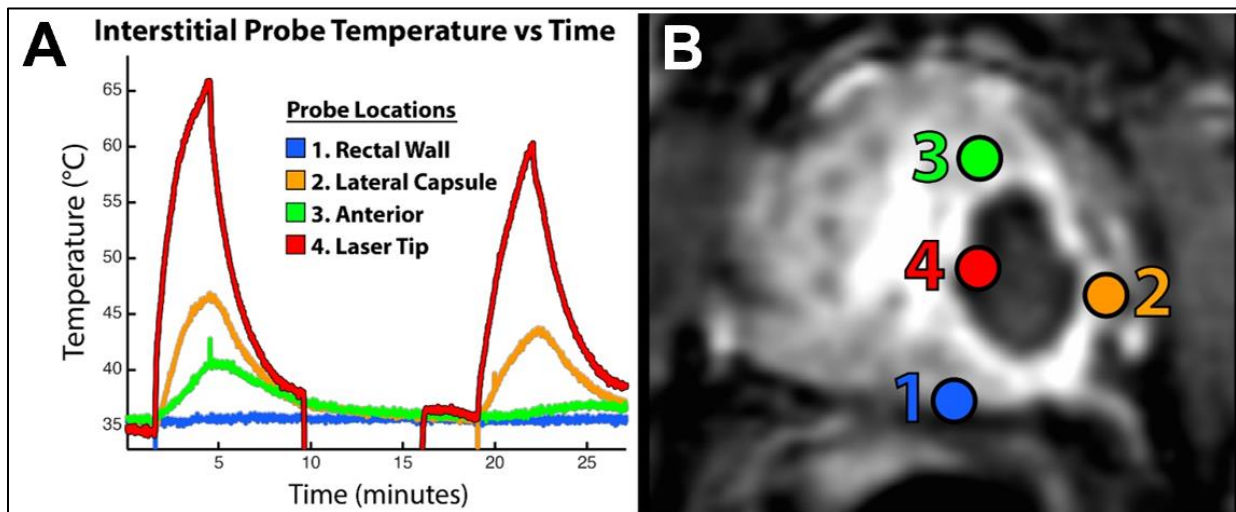


Figure 13: A) Temperature recorded by interstitial thermal probes during two consecutive laser activations. Note the laser tip exceeds 60°C while the rectal experiences negligible heating B) Non-perfused zone observed on MRI immediately after FLA. Note the that probe 4 lies on the edge of the ablation zone and the rectal wall remains intact.

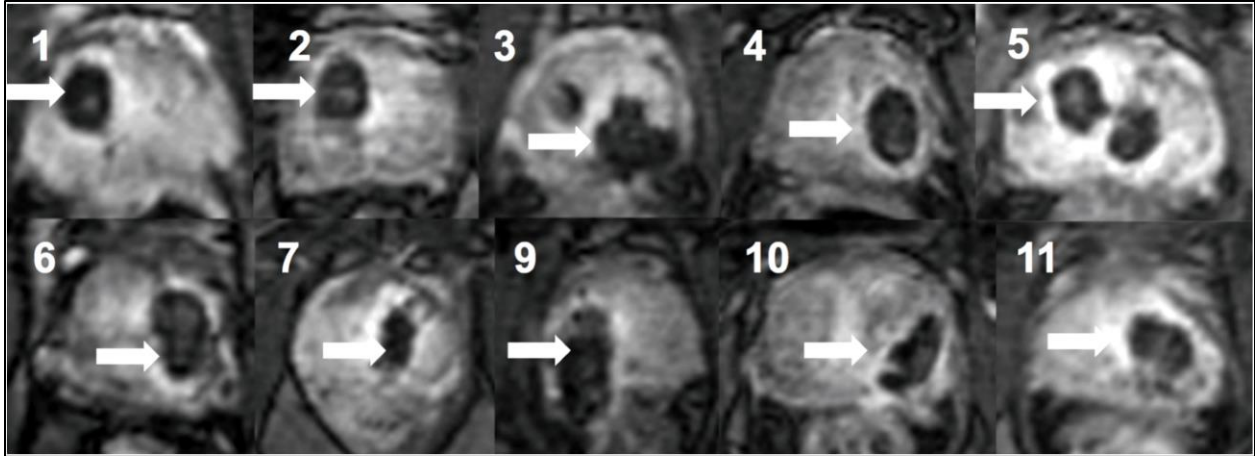


Figure 14: Contrast enhanced MRI acquired immediately after receiving FLA. In all 10 patients a distinct zone of non-perfused tissue is observed within the prostate capsule.

Median PSA decreased from 7.35 ng/ml at baseline to 2.55 ng/ml at 6 months follow-up (Wilcoxon signed rank test  $p = 0.28$ ). The procedure was found to be tolerable with patients reporting a median maximum pain score of 5 (medium). Six-month biopsy results found clinically significant disease in the treatment zone and margin of the first 4 patients. Microfocal Gleason 3+3 was observed in 3 patients with 3 more cancer free. Figure 15 shows the MRI and biopsy cores before and six months after treatment for one of the successful procedures. Before treatment, a tumor is visible on MRI and found to be Gleason 7 via MR-US fusion biopsy. Six months after treatment no cancer was detected by MRI or biopsy.



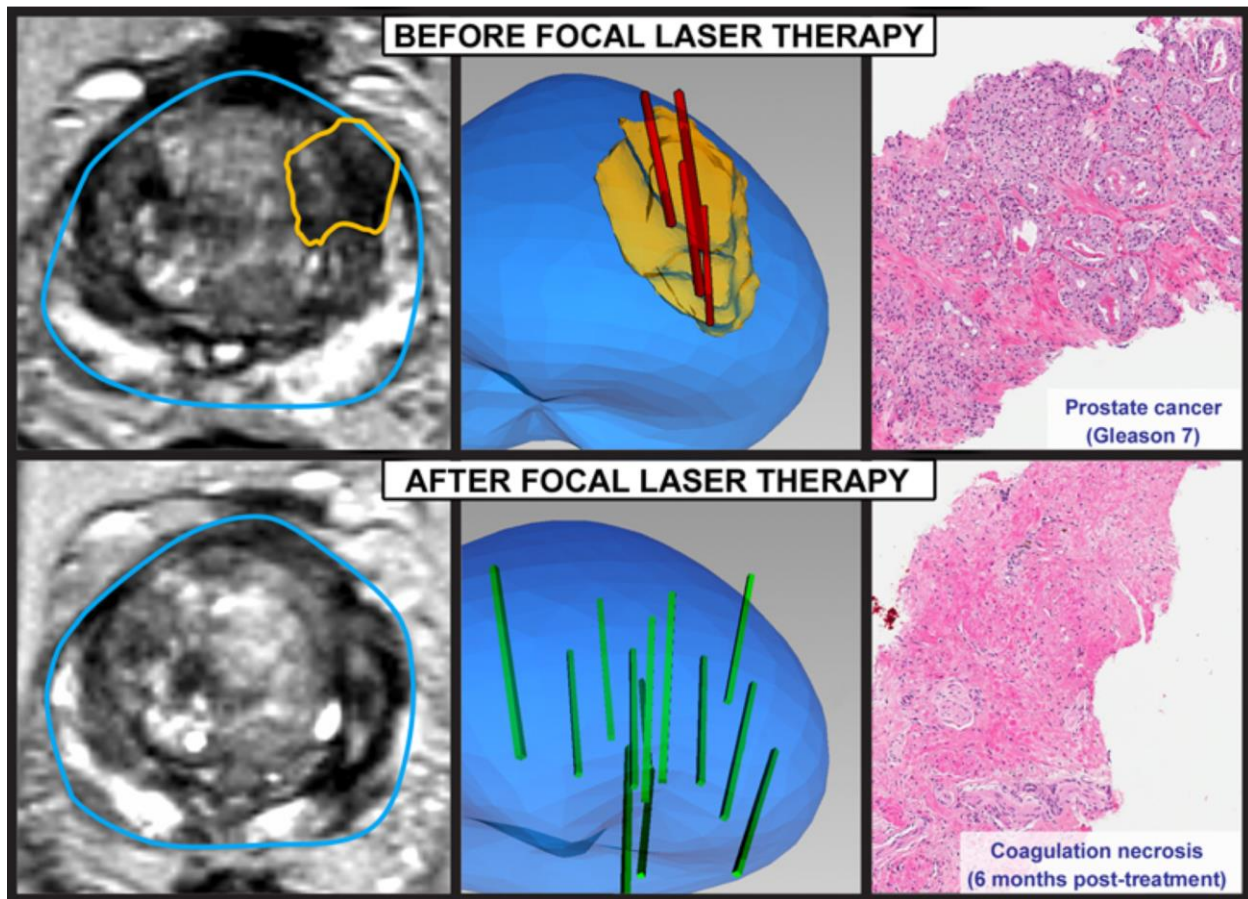


Figure 15: Imaging histologic findings in a patient successfully treated with MR-US fusion guided focal laser ablation. The top row shows the MR-visible tumor with positive biopsy cores (Gleason 7) within the ROI. Six months after receiving FLA, no tumor was visible on MRI and biopsy cores identifying coagulative necrosis within the ablation zone and no cancer outside the ablation zone.

Table 4: Summary of clinical trial patient characteristics. No serious adverse events were reported.

Patient No.	Age	Prostate Vol. (cc)	Treated Vol. (DCE, cc)	Procedure Time (min)	Burns $\geq 90s$	Adverse Events	Residual Gleason $\geq 7$	Residual Gleason 6
1	72	29.4	2.8	90	2	5	YES	NO
2	55	39.1	4.8	100	2	6	YES	NO
3	73	20.6	5.7	100	3	5	YES	NO
4	73	51.1	5.3	91	2	2	YES	NO
5	64	26.8	6.0	98	1	4	NO	YES
6	75	32.9	4.8	96	3	3	NO	NO
7	58	22.9	3.4	93	2	1	NO	YES
9	53	27.6	4.5	83	2	2	NO	NO
10	68	62.9	4.7	71	3	4	NO	NO
11	60	26.1	3.4	105	2	1	NO	YES

MR-guided FLA is the current state of the art and is under investigation at multiple centers. We contend that FLA can be performed under MR-US guidance with substantially reduced resource requirements, similar clinical outcomes and improved patient experience. While it is too early to draw definitive conclusions, we can compare key metrics between the MR-guided and MR-US fusion guided FLA trials performed at UCLA (Table 5). The MR-US guided trial exhibited greater ablation volume with an overall treatment time approximately 70% shorter than the MR-guided trial. The overall results also indicate fewer adverse events and improved oncologic outcomes in the US-guided trial. IT should be noted that the PSA score was only comparable the MRI-guided trial after the introduction of amended treatment protocol for the last six patients. Finally, the US-guided trial proved to be inherently less resource intensive as it can be performed in a urology clinic rather than an MR suite and requires two fewer critical personnel.

Table 5: Comparison of key metrics between UCLA's MR-guided and US-MR fusion guided clinical trials

	MR-Guided	US-Guided (All)	US-Guided (Last 6)
Mean Burn (cc)	4.1	4.7	4.8
Mean Time (hours)	4.9	1.5	1.5
Mean Adverse Event Count	3.6	3.4	2.3
Mean 9-Month $\Delta$ PSA (ng/mL)	-4.2	-1.8	-4.3
Residual Gleason 3 CaP	7 of 8 (88%)	7 of 10 (70%)	3 of 6 (50%)
Residual Gleason 4 CaP	5 of 8 (63%)	4 of 10 (40%)	0 (0%)
Critical Personnel	6	4	4
Facilities	Interventional MR Suite	Clinic Exam Room	Clinic Exam Room
Anesthesia	Versed and Fentanyl	Midazolam	Midazolam
Plan Registration	Cognitive	Fusion	Fusion

### 3.4. Discussion

The goal of this study was to demonstrate that MR-US fusion guided FLA is both feasible and safe. FLA for the treatment of prostate cancer has previously been demonstrated by multiple groups using MRI for both targeting and monitoring [6], [9]-[11]. In contrast, in this study we successfully performed FLA using MR-US fusion guidance and interstitial thermal probes for guidance and monitoring respectively. Although the procedure was technically feasible, numerous difficulties were encountered due to the lack of specialized instrumentation. In particular, MR-US fusion guidance was sufficient for ensuring catheter trajectory adhered to the treatment plan; however, achieving the correct depth required visualization of the trocar on ultrasound. This proved to be difficult until the introduction of the echogenic biopsy needle used on the last six patients. Other issues encountered include: catheter deflection, catheter movement after placement and thermal probe movement relative to the catheter tip. It is anticipated that all of these issues can be resolved with the development of appropriate instrumentation.

In general, the procedure was found to be safe with overall number of adverse events similar to that observed in the UCLA MR-guided trial (mean of 3.4 vs 3.6). Additionally, only 2.3 adverse events were seen in the group of patients treated after the introduction of the echogenic biopsy needle. Similarly, at 9-month biopsy, the overall PSA response was somewhat disappointing compared to the MR-guided trial (-1.8 ng/ml vs -4.2 ng/ml) but improved substantially in the last 6 patients (-4.3 ng/ml). On the 9-month biopsy the overall incidence of Gleason 3 and Gleason 4 were 70% and 40% which compares favorably to the MR-guided trial result of 88% and 63%. Moreover, in the last 6 patients these figures drop to 50% and 0% as a result of improved catheter visualization. While the sample sizes are too small to draw statistically valid conclusions,

the evidence strongly suggests that MR-US fusion guided FLA is at least as safe and effective as direct MR-guided FLA. Given that it also inherently less resource intensive, it may help to accelerate widespread adoption of FLA for the treatment of prostate cancer.

### 3.5. Retrospective Analysis of Thermal Probe Utility

FLA achieves cancer control via thermally induced coagulative necrosis. This process is a function of both temperature and time. Many groups have attempted to estimate the extent of cell death based on the Arrhenius model introduced by Moritz and Henriques in 1947 [122]-[125]. Indeed, the Visualase system which is used in the majority of MR-guided clinical trials, relies on this model to create damage maps based on MR thermometry data. The damage maps quantify the extent of the ablation in real-time and inform the decision to deactivate the laser. Damage is quantified using a single parameter ( $\Omega$ ) as shown below:

$$\ln\left(\frac{C(0)}{C(t)}\right) = A \int_0^{\tau} e^{-\frac{E_a}{RT(t)}} dt = \Omega(t)$$

where  $C(0)$  is the concentration of viable cells before the procedure,  $C(\tau)$  is the concentration at time= $\tau$ ,  $A$  is the pre-exponential/frequency factor [s<sup>-1</sup>],  $E_a$  is the activation energy barrier (J mole<sup>-1</sup>),  $R$  is the universal gas constant (1.987 x 10<sup>-3</sup> Kcal/mole·K, and  $T$  is the temperature (K).

The fraction of surviving cells is thus given by:

$$C(\tau) = 100e^{-\Omega} (\%)$$

The model requires a priori knowledge of the tissue specific kinetic parameters  $E_a$  and  $A$ . Many authors have empirically determined these values for prostate as shown in Table 6. The values determined by Henriques et al were found based on analysis of skin burns; however, these are the values used by the commercially available Visualase system.

Table 6: Kinetic parameters used in modelling thermally induced coagulative necrosis in the prostate

	<b>Bhowmick</b>	<b>Henriques</b>	<b>Jacques</b>	<b>Skinner</b>
	[130]	[122]	[194]	[195]
<b><math>E_a</math> (kJ/mol)</b>	160.7	630	186.6	385
<b><math>A</math> (s<sup>-1</sup>)</b>	7.78x10 <sup>22</sup>	3.1x10 <sup>98</sup>	2.08x10 <sup>27</sup>	3.8x10 <sup>57</sup>

To assess the utility of the Arrhenius damage model, we applied it to the thermal data acquired by the efficacy probe in the clinical trial and calculated the optimal exposure duration (the minimum exposure duration required to cause coagulative necrosis at the location of the probe i.e. 8mm from the laser fiber). Figure 16 shows the resulting estimated cell death as function of time for a single burn. Laser activation causes a steady increase in temperature with rapid cooling observed after laser deactivation. Consequently, the majority of cell death occurs during laser activation. It is generally assumed that 63% cell death is sufficient to render the tissue non-viable. Under this assumption, 7 laser activations from the clinical trial produced ablation zones that matched or exceeded the target radius of 8mm. This does not include laser activations that may overlap existing ablation zones. For these 7 laser activations, 93% (mean) of total cellular death occurred during laser activation with 7% during the cooling phase. The optimal exposure duration was therefore defined as the exposure duration necessary to achieve 59% cell death during laser activation. The optimal exposure

duration was found for a further 5 laser activations via extrapolation giving a total dataset of 12 laser activations (Figure 17). The average optimal exposure duration was determined for these laser activations using each of the kinetic parameters shown in Table 6 (Figure 18). Using a one-way ANOVA, a statistically significant difference was found between the estimates ( $p < 0.01$ ). A post-hoc analysis (Tukeys HSD) shows that there is no statistically significant difference between the estimates provided by Skinner et al and Jacques et al.

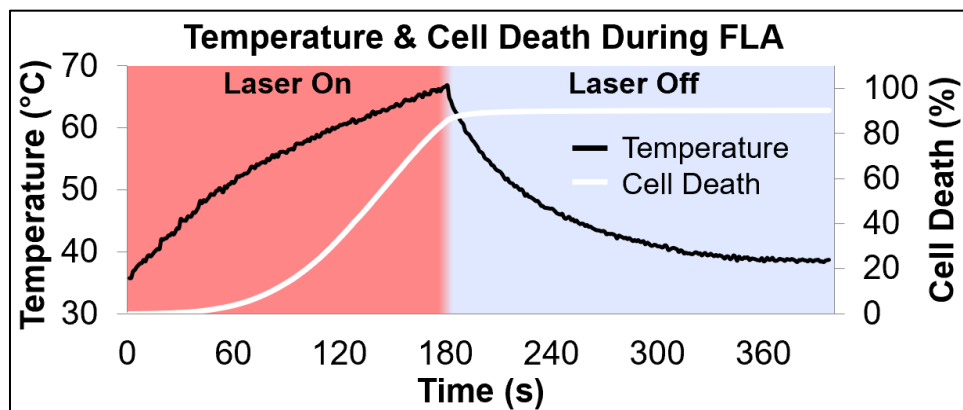


Figure 16: Estimated cell death during FLA of a patient based on the Arrhenius model and interstitial thermal probe data (Kinetic parameters: Jacques et al)

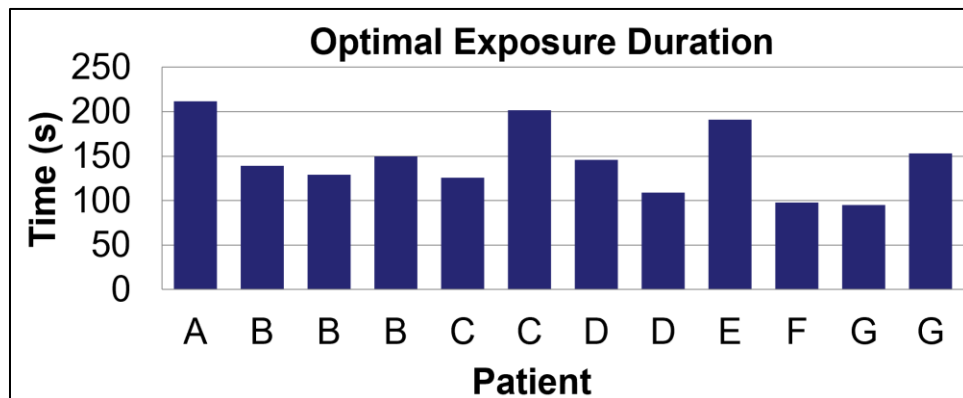


Figure 17: Optimal exposure duration for select laser activations (Kinetic parameters: Jacques et al) Note: all patients received multiple ablations but the dataset was limited to those in previously untreated tissue. Mean =145.8 standard deviation = 37.2s.

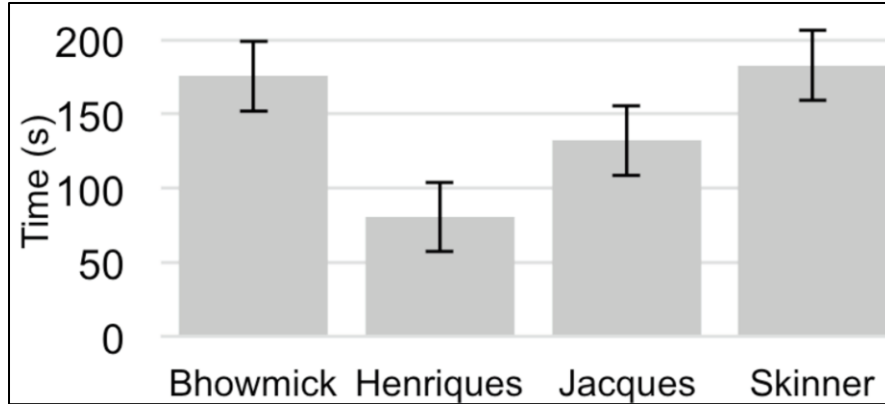


Figure 18: Comparison of optimal exposure duration estimated using the Arrhenius model with kinetic parameters from the literature.

The Arrhenius model provides an elegant method of determining the extent of coagulative necrosis and thus informing the decision to cease laser activation. However, it may be inherently unreliable due to inaccurate a priori knowledge of the kinetic parameters  $E_a$  and  $A$ . By applying the model to clinical data, we have shown that the published values for these parameters result in significantly different estimates of the exposure duration necessary to induce coagulative necrosis. Given the variation in published values for the kinetic parameters, it is possible that they vary between samples and thus cannot be determined for a given patient. We can therefore conclude that the utility of interstitial thermal probes for monitoring FLA is inherently limited due to the inability to accurately model thermally induced coagulative necrosis using the Arrhenius model.

### 3.6. Conclusion

MR-US fusion guided FLA for the treatment of prostate cancer is safe and potentially effective. In this preliminary study there was no long-term impact on sexual, urinary or general patient health. The initial protocol used to treat the first 4 patients was

ineffective due to difficulty visualizing catheter placement. With the introduction of improved instrumentation, the incidence of residual clinically significant disease dropped substantially. In addition, both the clinical outcomes and resource requirements compare favorably to our previous MR-guided trial. Further refinement of the procedure followed by a larger multicenter trial is necessary to assess the oncologic effectiveness of the treatment. Improved real-time monitoring was identified as a key area in need of development as the utility of interstitial thermal probes is inherently limited due to inaccurate thermal models.



# Chapter 4

## Optical Monitoring as a Potential Alternative to Thermal Monitoring

### 4.1. Introduction

In chapter 3 we demonstrated that FLA can be performed safely using MR-US fusion for guidance and interstitial thermal probes for feedback. We also analyzed the Arrhenius damage model that is frequently used to estimate the extent of coagulative necrosis based on thermal history. The model requires a priori knowledge of tissue specific kinetic parameters. Many groups have empirically derived these values; however, in chapter 3 we demonstrated that the variability between these values has a significant impact on the exposure duration determined by the damage model. To improve the method of monitoring MR-US fusion guided FLA, either accurate kinetic parameters for prostate must be determined or an alternative monitoring method must be developed. Given that the former has proved to be somewhat elusive we elected to focus on an alternative monitoring modality, specifically interstitial optical monitoring.

Interstitial optical monitoring may offer numerous advantages over interstitial thermal monitoring. The primary advantage is that it does not rely on the Arrhenius damage model. The Arrhenius model itself was developed to analyze the relationship between temperature and the rate constant of a chemical reaction. Empirical studies later demonstrated that it could be used to model thermally induced coagulative

necrosis [123]. It is therefore not based on comprehensive understanding of an underlying physical principle. In contrast, optical monitoring is based on the fundamental principles of laser-tissue interaction. Consequently, it provides a more direct method of characterizing the coagulative state of tissue rather than relying on an empirical model.

The second advantage of optical monitoring is that the intensity of light at a given position is a function of light-tissue interactions throughout a volume. Therefore, in contrast to a thermal probe, the signal recorded by an optical probe may be sufficient to infer the coagulative state of tissue at a distance from the probe. This is of particular interest in FLA due to tissue charring which can occur around the laser fiber as was observed in the clinical trial. Char acts as a light trap; therefore, an optical probe may be able to correlate signal loss to the onset of char. If treatment continues after the onset of char, the vast majority of photons will be absorbed near the fiber resulting in temperature sufficient to melt the dual lumen catheter. This could potentially result in detachment of the catheter tip which represents a serious adverse event and must be surgically removed.

A further advantage of interstitial optical monitoring is that feedback occurs near instantaneously with software processing the likely limiting factor. When monitoring a critical structure such as the rectal wall, an optical probe can immediately identify if the laser fiber is too close and likely to induce thermal damage. In contrast, a thermal probe can only provide similar feedback after sufficient energy has been deposited in the tissue to cause a temperature elevation. If the laser fiber is sufficiently close and activated at high power, the critical structure may be damaged before a thermal sensor can provide feedback.

The final advantage of optical monitoring is the ability to assess tissue condition after cooling. Clinically, FLA generally requires multiple overlapping ablations; therefore, both the laser fiber and the dosimetry probe must be repositioned between ablations. Protein coagulation causes a persistent change in laser-tissue interaction. As result it is possible confirm that the laser fiber and probe have been inserted into native rather than coagulated tissue. In contrast, a thermal probe can only estimate cellular damage by recording the thermal response during ablation. It is therefore not possible to determine tissue condition after repositioning for a second ablation.

In this chapter, we will outline the fundamental principles of laser-tissue in the context of FLA and then apply these principles to generate our hypothesis that an interstitial optical monitoring system can be used to monitor FLA. A short series of experiments are then presented as proof of concept. The chapter closes with a discussion of the steps necessary to robustly demonstrate the correlation between a measured optical signal and the growth of the coagulation zone during FLA.

## **4.2. Fundamentals of Laser Tissue Interaction**

The propagation of light in tissue is governed by the absorption coefficient ( $\mu_a$ ) and the reduced scattering coefficient ( $\mu'_s$ ) as depicted in Figure 19. In FLA, light is emitted from an interstitial optical fiber; therefore, reflection and remission can be ignored. In this research, we are concerned with FLA performed with a 980nm laser which has a relatively shallow penetration depth; thus, remission and transmission are also negligible.

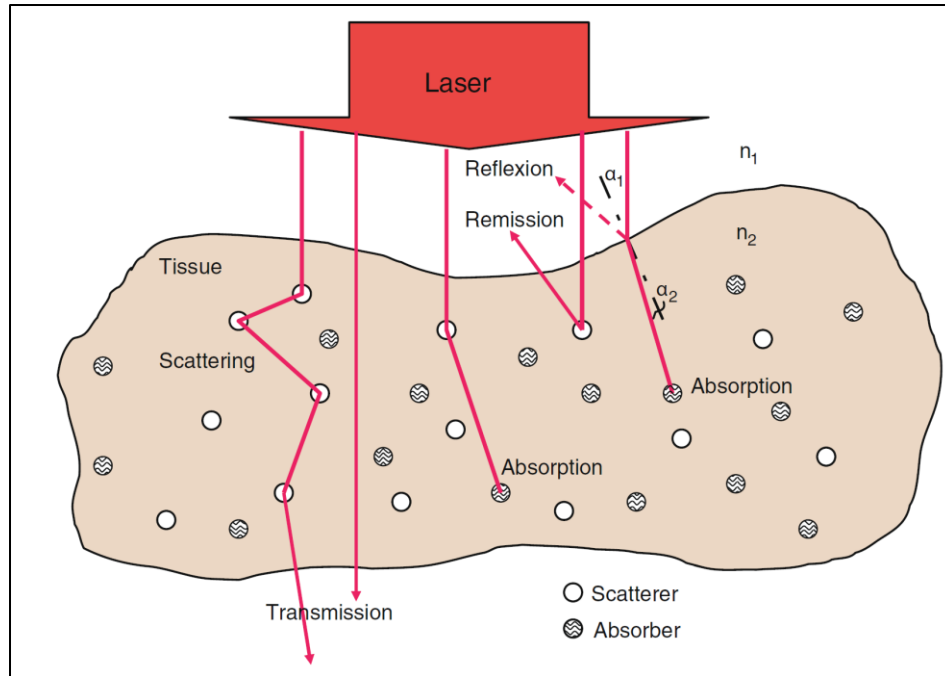


Figure 19: Laser-tissue interactions [196]

#### 4.2.1. Absorption Coefficient

Photons continue to propagate through tissue until they are absorbed by a chromophore. The probability of absorption per infinitesimal path length ( $\Delta x$ ) is  $\mu_a \Delta x$ . Additionally,  $1/\mu_a$  is the mean free path length between absorption events. At 980nm, the wavelength of FLA in our clinical trial, the primary absorbers are water molecules, oxyhemoglobin and deoxyhemoglobin (Figure 19).

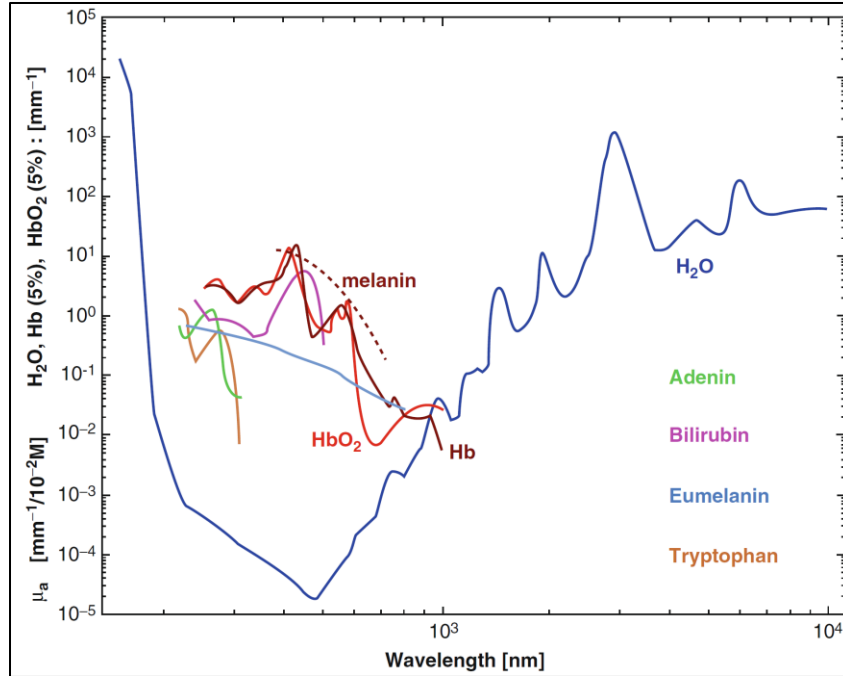


Figure 20: Absorption coefficient as a function of wavelength for typical chromophores in tissue[196]

#### 4.2.2. Scattering and Reduced Scattering Coefficients

As photons propagate through tissue, interactions with scatterers (Figure 21), result in a change in propagation direction without energy deposition. This behavior is characterized by the scattering coefficient ( $\mu_s$ ). Scattering events are classified as either Mie scattering or Rayleigh scattering with the former relevant for FLA. The probability of scattering per infinitesimal path length ( $\Delta x$ ) is  $\mu_s \Delta x$  while  $1/\mu_s$  is the mean free path length between scattering events. Mie scattering is not isotropic and the scattering direction is quantified using the anisotropy factor ( $g$ ) which ranges from 0 (isotropic) to 1 for forward scattering 0 to -1 for backscattering. Light tends to scatter forwards in tissue with typical values for  $g$  in the range 0.8 to 0.99. Taking into account the direction of light propagation, scattering can be better defined using the reduced scattering coefficient:  $\mu'_s = \mu_s(1 - g)$ .

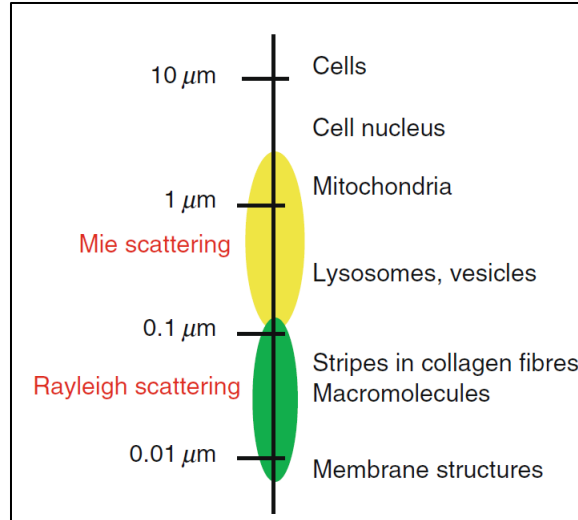


Figure 21: Mie and Rayleigh scattering

### 4.2.3. Effective Penetration Depth

The effective penetration depth is defined as the mean free path between attenuation events and is given by:

$$\delta_{eff} = \frac{1}{\mu_{eff}}$$

with the effective attenuation coefficient defined by:  $\mu_{eff} = \sqrt{3\mu_a(\mu_a + \mu_s)}$ . In tissues with long penetration depth, light is distributed over a large volume while the opposite occurs if the penetration depth is short.

## 4.3. Laser-Tissue Interaction During FLA

### 4.3.1. Dynamic Optical Properties

FLA achieves cancer control through thermally induced coagulative necrosis. During this process, proteins coagulate resulting in an increase in  $\mu'_s$  while  $\mu_a$  remains relatively constant. Consequently, FLA is characterized by a decrease in  $\delta_{eff}$ . For near infrared

light,  $\delta_{eff}$  will decrease approximately 30% due to an increase in  $\mu'_s$  of approximately 130% (Table 7). The influence of the optical properties on the coagulative response can be seen in a paper by Jiang et al [197]. In this work FLA was simulated in the liver with lasers of different wavelengths (850nm, 980nm, 1064nm). As expected 850nm and 980nm lasers induce a similar coagulative response; however, the 1064nm laser coagulates a much smaller volume of tissue. This occurs because the penetration depth is too large and thus energy deposition in the tissue is not sufficiently concentrated to increase the temperature above the coagulation threshold. During FLA, the opposite phenomenon occurs after the onset of coagulation. The coagulation zone expands outward from the laser fiber creating a zone of tissue with a short  $\delta$  which decreases the amount of light reaching areas distal to the fiber and limits the growth of the ablation zone. As light becomes trapped near the fiber, excessive temperatures can occur causing tissue char and potentially damaging the laser fiber and catheter. In an effort to reduce this risk, the catheter is cooled through continuous circulation of saline.

Table 7: Optical Properties of Prostatic Tissue in the Native and Coagulated State

Tissue	$\lambda$ (nm)	$\mu_{a\_native}$ (cm <sup>-1</sup> )	$\mu_{a\_coagulated}$ (cm <sup>-1</sup> )	$\mu'_{s\_native}$ (cm <sup>-1</sup> )	$\mu'_{s\_coagulated}$ (cm <sup>-1</sup> )	$\Delta\mu_a$ (%)	$\Delta\mu'_s$ (%)	$\Delta\delta_{eff}$ (%)
Human [198]	850	0.6	0.7	6	13.8	+17	+130	-38
Human [198]	1064	0.3	0.4	4	9	+33	+125	-41
Human [199]	1064	0.78	0.75	6.3	10.8	-4	+71	-20
Canine [198]	850	0.6	0.7	5.2	13.5	+17	+160	-41
Canine [198]	1064	0.4	0.5	4.4	8.8	+25	+100	-36
Canine [199]	1064	0.27	0.19	17.6	24.4	-30	+39	+17
Canine [199]	1064	0.71	0.47	7.9	29.4	-34	+272	-34
<b>Average Change in Optical Properties</b>						<b>+3</b>	<b>+128</b>	<b>-30</b>

### 4.3.2. Hypothesis Generation

The dynamic optical properties observed during FLA could potentially serve as a contrast mechanism to indicate the onset and propagation of thermally induced tissue coagulation. This concept was explored by Whelan et al who used an isotropic point detecting optical fiber to monitor fluence during FLA [188]. This fiber was placed 5mm from the source fiber during FLA in porcine kidney in vivo. Tissue coagulation resulted in 49% decrease in optical intensity.

Rather than monitoring the absolute change in optical intensity we hypothesize that the relative change will be of greater utility. To generate our hypothesis we performed the simplified thought experiment outlined in Figure 22 in which we consider



the effect of thermal coagulation on the optical signal recorded by an interstitial thermal probe.

- A. When the laser is initially activated, photons follow a relatively direct path towards the sensor. Consequently, many photons reach the sensor and the signal is high. Let's assume that of all the photons that propagate towards the sensor, 90% reach the sensor and 10% are absorbed.
- B. The absorbed photons cause tissue coagulation and thus increased scatter. As more photons are released, they scatter through the coagulated tissue and thus the path length to the sensor has been increased. The longer path length increases the number of interactions with chromophores leading to greater energy deposition in the tissue. Now, let's assume that 40% of photons are absorbed and only 60% reach the sensor.
- C. The deposited photons increase the volume of coagulated tissue resulting in an increase in scatter. Again, the path length is increased and now fewer photons reach the sensor as much of the energy is deposited in the tissue. Let us assume that 30% of the photons reach the sensor.
- D. At this point, the coagulation boundary has propagated as far as the sensor. The newly deposited photons cause further growth of the coagulation zone but the path length remains unchanged and thus the optical signal has reached a plateau.
- E. If laser activation continues, the coagulation zone expands beyond the optical sensor; however, as the path length remains constant so too does the optical signal.

The results of this thought experiment allow us to formulate the hypothesis that: an interstitial optical probe can be used to ensure complete thermal necrosis in a predefined region of prostatic tissue. This can be achieved by placing the probe at the desired boundary and terminating laser ablation once the recorded optical signal reaches a plateau.

The thought experiment greatly simplified the dynamic response of laser irradiated tissue. For example, light is highly scattered even when all of the tissue is in the native state. It is therefore, more scientifically rigorous to describe laser tissue interaction in terms of the dynamic optical properties shown in Table 7. Here we see that thermal coagulation causes a substantial increase in  $\mu'_s$  (~130%) and a corresponding decreasing in  $\delta$  (~30%). Therefore, as the coagulation boundary propagates towards the optical sensor, the average  $\delta$  (the penetration depth of all tissue between the laser source and sensor) decreases and reaches a steady state once all the tissue is coagulated. Further expansion of the coagulation boundary has no impact on the optical properties of the tissue between the laser source and the sensor; therefore, the optical signal remains constant.

In this scenario a ballistic optical sensor is used i.e. a sensor in which only photons travelling directly from the source are detected. An alternative hypothesis can be formed by rotating the sensor away from the source as depicted in Figure 23. Here we assume that none of the photons are detected until the coagulation boundary passes the sensor and induces sufficient scatter to cause some photons to travel backwards after passing the sensor (Figure 23D). Once this occurs an increase in optical signal is observed; hence, an optical sensor that only detects backscatter could be used to identify the coagulation boundary based on a sudden increase in optical signal. Consequently, it

is clear that the design of the sensor is critical to ensure accurate identification of the ablation boundary. Indeed, it may be beneficial to detect both ballistic and backscattered photons so that the passing of the coagulation boundary is indicated by an optical intensity inflection point rather than a plateau. An obvious disadvantage of the backscatter sensor is that there is no feedback until the coagulation boundary passes the sensor; therefore, it is not possible to confirm the inset and propagation of the coagulation front. While this may true in our simplified analysis, in practice it is likely that there is always some backscatter even with all of the tissue in the native state; however, the resulting optical signal be of insufficient magnitude to register with the photodiode.

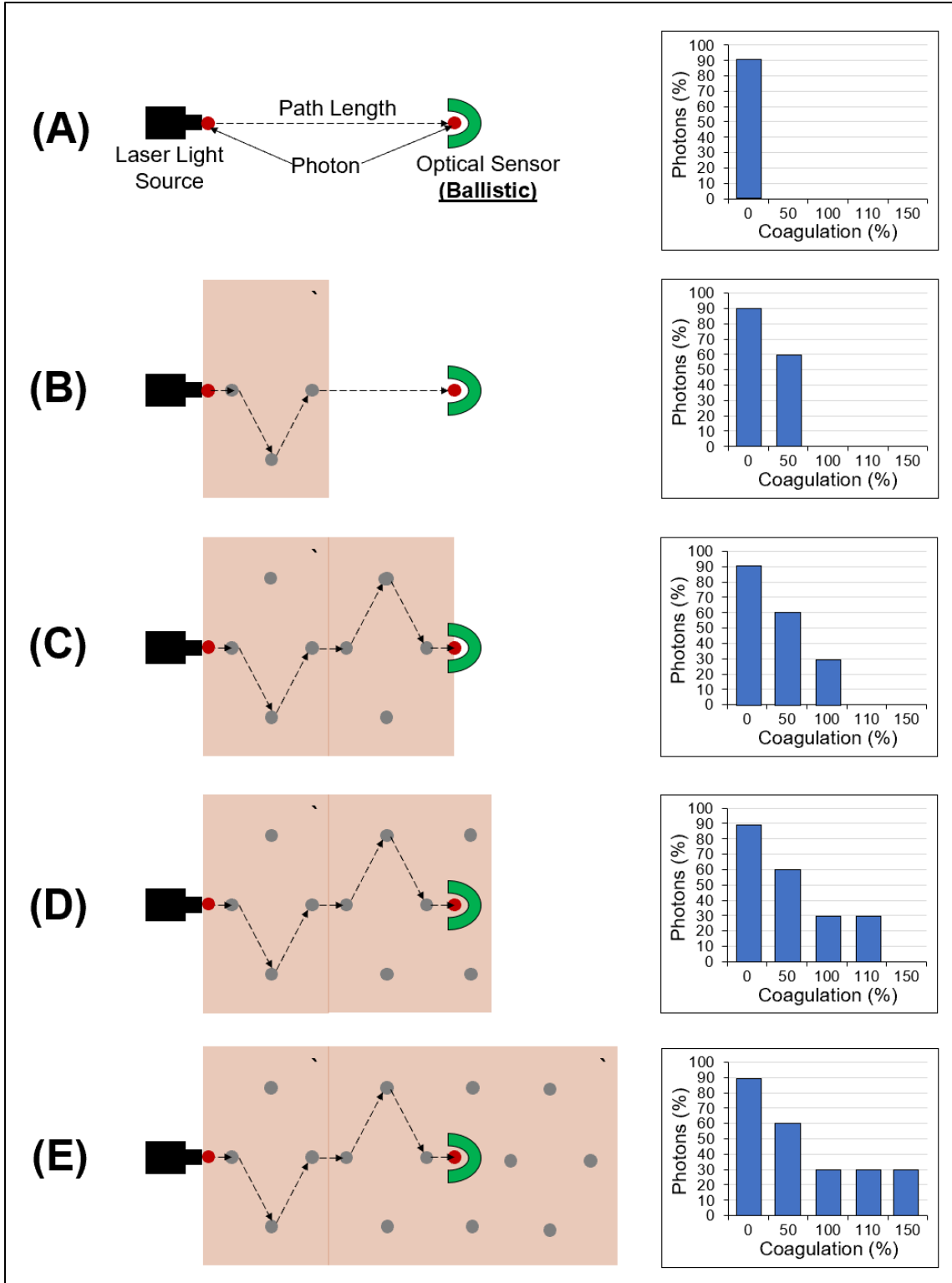


Figure 22: Thought experiment with ballistic optical sensor

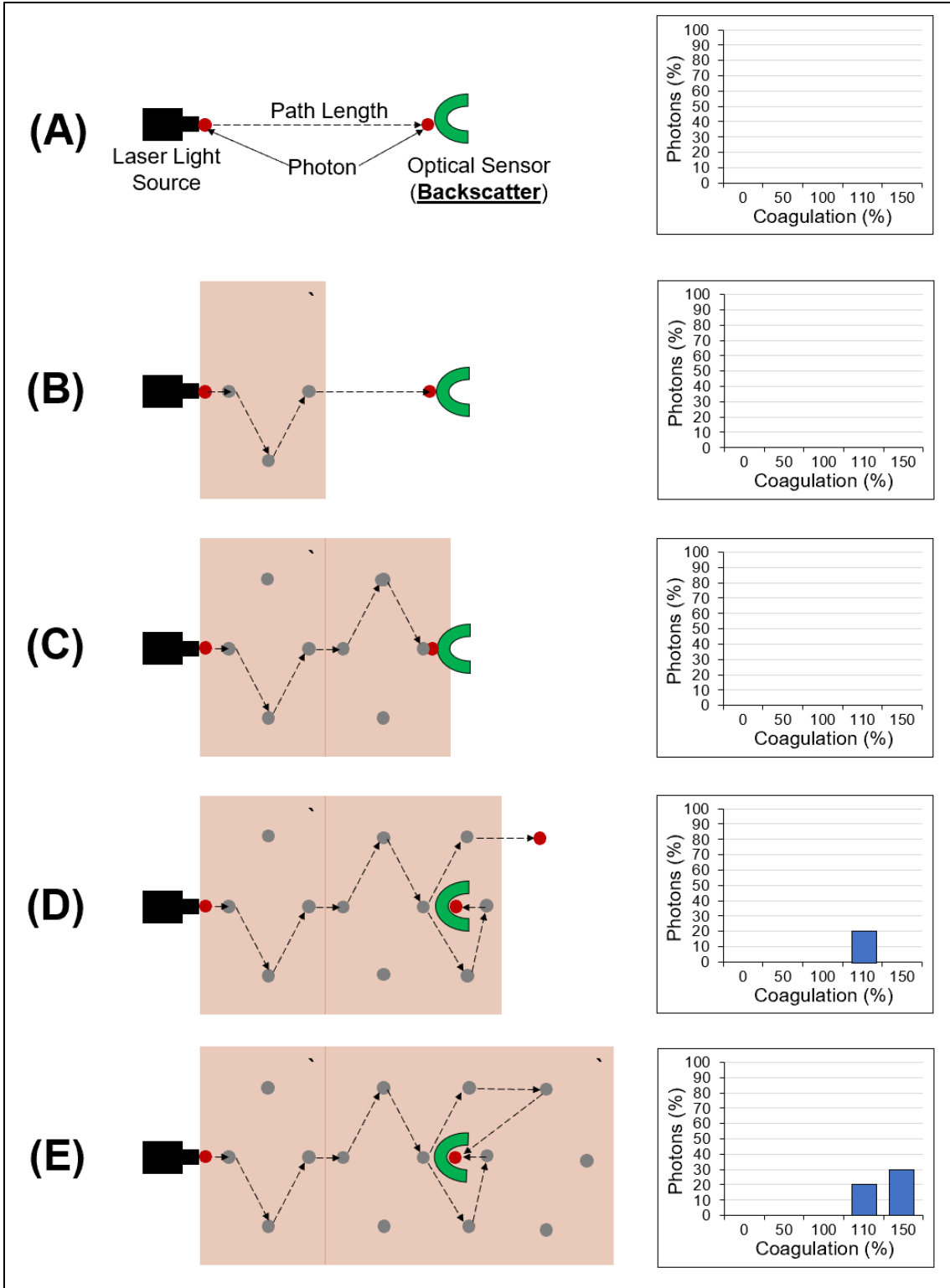


Figure 23: Thought experiment with backscatter optical sensor

## 4.4. Proof of Concept

A simple experiment was undertaken to illustrate proof of concept and identify the key challenges that must be overcome. The experimental setup is illustrated in Figure 24. Ex vivo bovine muscle was preheated to 37°C and placed in a 3D printed sample holder. A water-cooled catheter (Visualase, Medtronic) housing a laser fiber was inserted into the center with a thermal and optical probe positioned either side at a radial distance of 8mm. The thermal and optical probes consist of 14Ga flexi-needles containing a fluoroptic thermal sensor (Lumasense, CA) and a 600µm optical fiber with a 5mm long cylindrical diffuser respectively. The optical probe is connected proximally to a photodiode (PDA36A, Thorlabs, NJ) which outputs an analog signal in the range 0-10V. A voltage divider was used to decrease the range to 0-5V to accommodate the microcontroller (Arduino Leonardo, Arduino LLC, Italy) which converts the analog signal to a digital signal and outputs the data to a PC. Custom built software (Python) is then used to display the signal in real-time and save the results to disk as a .csv file. Similarly, the thermal sensor is connected to the FOT lab kit, voltage divider, microcontroller and finally to the PC. FLA was performed at 13.75W for 200s using a 980nm laser. After laser deactivation, the sample was removed from the holder and sliced along the trajectory of the catheters to facilitate visual inspection of the coagulation zone.

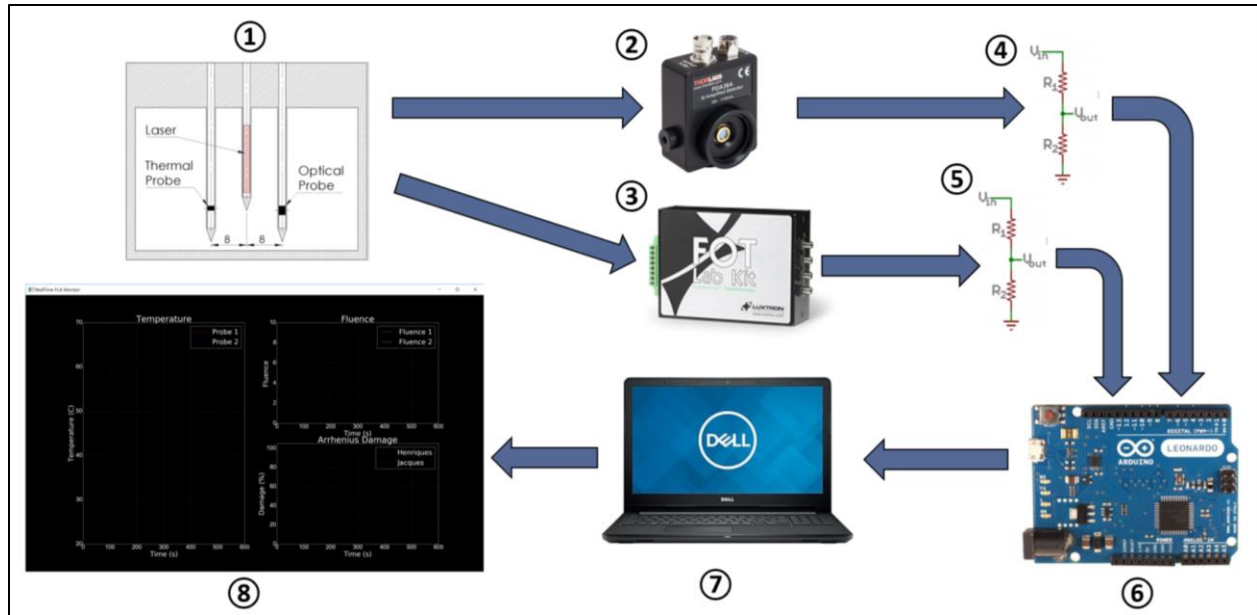


Figure 24: Experimental setup – 1) Ex vivo bovine muscle sample holder with laser fiber, thermal probe and optical probe, 2) Photodiode, 3) FOT lab kit, 4) Voltage divide, 5) Voltage divider, 6) Microcontroller, 7) Dedicated PC and 8) Custom built software for data visualization and recording

Temperature and normalized photovoltage are shown in Figure 25. Within seconds of laser activation, the temperature begins to rise while the normalized photovoltage falls. Normalized photovoltage falls because the tissue coagulates causing an increase in the reduced scattering coefficient and thus total attenuation. The results correlate with previously published data by Whelan et al who performed a similar study using in vivo porcine kidney [200]. Interestingly after approximately 60s the normalized photovoltage stops falling. This appears to indicate that the coagulation boundary is approaching the sensor. These events are not detected by the thermal sensor, which continues to show a steady rise in temperature.

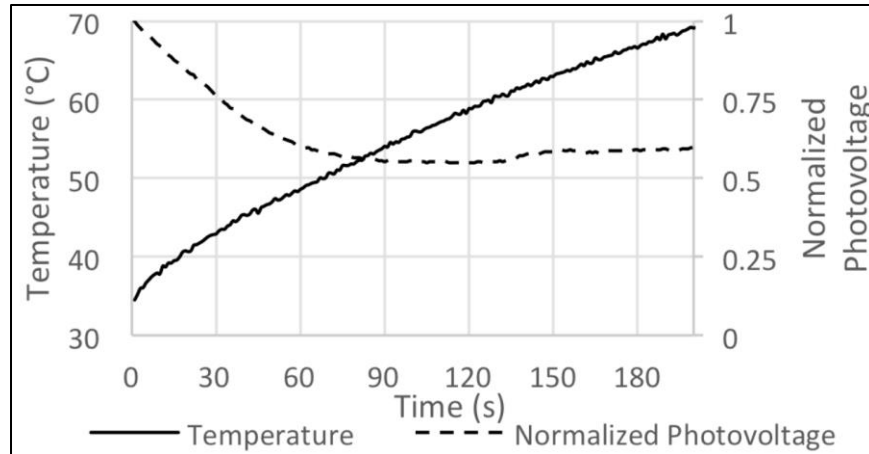


Figure 25: Temperature and photovoltage during FLA

Figure 6 compares damage estimates using the Arrhenius thermal damage model outlined in Chapter 3. Again, the normalized photovoltage drops throughout the procedure indicating the development of tissue coagulation while none of the damage estimates show significant coagulation until 100s. This clearly demonstrates that unlike the thermal system, the optical monitoring system provides an instantaneous representation of opto-thermal events occurring throughout the volume. Additionally, the thermal damage estimates vary wildly as observed in Chapter 3. Finally, the slope of the normalized photovoltage could be used to modulate laser power. For example, a steep slope may indicate that char will occur before the desired volume is ablated. This data could be used to decrease laser power; thus, allowing for greater heat transfer via conduction before the tissue chars. In this way the size of the ablation zone can be maximized.

The key limitation of this study is the inability to correlate the optical signal with the growth of the coagulation zone. It is also difficult to quantify the final coagulation zone as illustrated in Figure 27. While the coagulation zone is clearly visible, accurately delineating the coagulation boundary remains challenging. Consequently, in order to



empirically demonstrate the utility of the optical monitoring system, further studies must be undertaken in a material in which the growth of the coagulation zone can be quantified and compared to the optical signal.

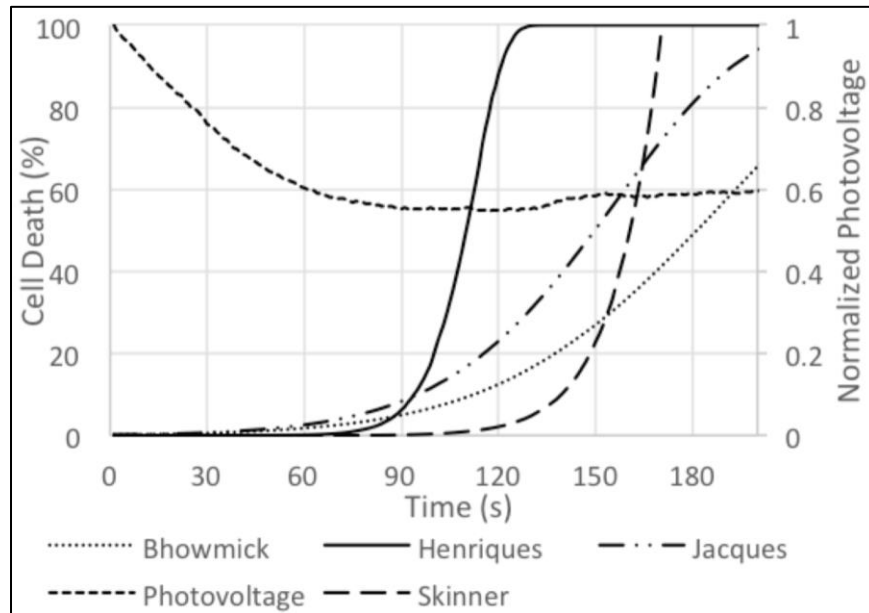


Figure 26: Temperature and predicted cell death during FLA

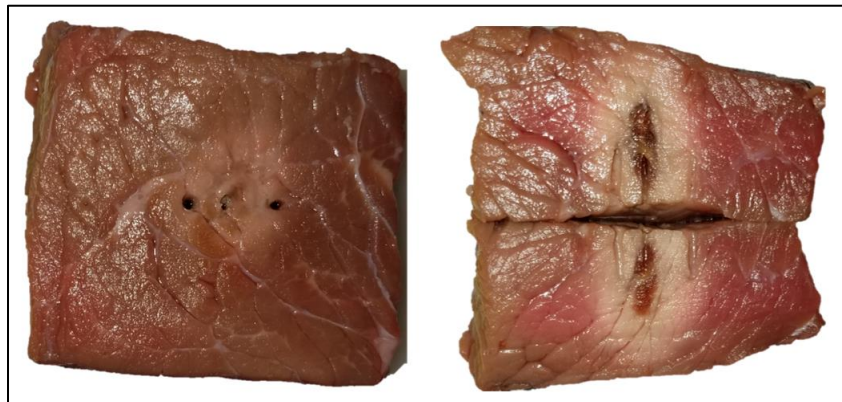


Figure 27: Ex vivo bovine muscle after FLA treatment. Note the extensive char visible along the length of the laser fiber

## 4.5. Conclusion

The signal recorded by an interstitial optical probe during FLA appears to correlate with the propagation of the coagulation boundary. In contrast, temperature rises at an approximately steady rate providing no information regarding the location of the coagulation boundary. The damage estimates provide by the Arrhenius damage model also appear to correlate with the growth of coagulation zone but conflicting estimates are provided due to inconsistent kinetic parameters.

To fully illustrate the correlation between the growth of the coagulation zone and the optical signal, a material is required in which the propagation of the coagulation zone can be accurately quantified. In the next chapter, we outline our efforts to develop such material and demonstrate its similarity to *in vivo* human prostate. In subsequent chapters the utility of interstitial optical probes will be demonstrated using this material as a prostate model and finally the probes will be tested in *ex vivo* bovine muscle.

# CHAPTER 5

## A Tissue-Mimicking Prostate Phantom for 980nm Focal Laser Ablation

### 5.1. Introduction

Focal laser ablation has been demonstrated to be a promising method of focal therapy for prostate cancer [10], [11], [73], [192]. The procedure consists of inserting a laser fiber into a target tumor and raising the temperature above 60°C. A 980nm diode laser is frequently used. Given the fixed wavelength, the induced zone of coagulative necrosis is primarily dependent on laser power, exposure duration and device characteristics such as diffuser length. Understanding the effect of these parameters on the resulting damage zone is critical for clinical success. Prior work investigating thermal response has relied on animal models [201]-[203] and cadaveric prostate [204]. Such models are heterogeneous across specimens, resulting in the requirement for a large number of samples to accurately assess laser-tissue interaction. The optical properties of these models may not be sufficiently similar to human prostate and the experimental approach is complicated by their biohazardous nature. Additionally, the zone of thermal necrosis is difficult to quantify and requires histologic analysis. Therefore, there is a need to develop a tissue-mimicking phantom to provide a standardized, controllable model for investigations of both the optical and thermal response of prostatic tissue to 980nm focal laser ablation.

Magnetic resonance thermometry is frequently used as a method of monitoring FLA; however, the resulting damage maps have been shown to overestimate the extent of thermal necrosis due to motion artifact and inaccurate thermal damage models [132]. Interstitial thermal probes have also been used as a method for monitoring ablation [193], [205]. In contrast to MRT, interstitial probes only provide thermal data for a single point. It is therefore necessary to utilize *a priori* assumptions to estimate the volume of coagulative necrosis. A tissue-mimicking phantom would provide a robust platform for further development of both MRT and interstitial thermal probes in this field. In this work we have developed the requisite phantom and demonstrated similarity to prostatic tissue using previously acquired clinical data. Furthermore, it is envisioned that the phantom will find utility in the development and characterization of FLA systems as well as for validation of computational models.

The propagation of light in tissue is governed by the absorption coefficient ( $\mu_a$ ) and the reduced scattering coefficient ( $\mu'_s$ ). The reduced scattering coefficient is given by  $\mu'_s = \mu_s(1 - g)$ , where  $\mu_s$  and  $g$  are the scattering coefficient and anisotropy factor respectively. In order to achieve clinically relevant thermal damage volumes in a phantom, the material must possess both a similar  $\mu_a$  and  $\mu'_s$  to tissue. Moreover, studies have shown that thermal tissue damage can cause up to a five-fold increase in total attenuation [195], [206], [207]. This is predominantly due to increased scatter as a result of thermally induced protein coagulation. The phantom material must therefore, also exhibit dynamic optical properties such that  $\mu'_s$  increases substantially when exposed to temperatures sufficient to induce rapid protein coagulation. This threshold is generally accepted to be 60°C [24]. Studies have highlighted the correlation between optical properties and the resulting coagulation zone during FLA. For example, using an *in vivo*

murine model, Nikfarjam et al. found that an Nd-Yag (1064nm) laser takes 50s to achieve the same coagulation zone diameter as observed after 20s with a diode laser (980nm) [208]. This occurs because the diode laser has a shorter penetration depth. Similar results were reported by Jiang et al. through simulation of FLA in the liver [197]. After 600s the predicted volume of coagulated tissue was almost three times greater using a 980nm (native:  $\mu_a=0.6\text{cm}^{-1}$ ,  $\mu'_s= 9.7\text{cm}^{-1}$ , coagulated:  $\mu_a=0.5\text{cm}^{-1}$ ,  $\mu'_s= 14.7\text{cm}^{-1}$ ) laser compared to a 1064nm (native:  $\mu_a=0.3\text{cm}^{-1}$ ,  $\mu'_s= 9.0\text{cm}^{-1}$ , coagulated:  $\mu_a=0.2\text{cm}^{-1}$ ,  $\mu'_s= 13.9\text{cm}^{-1}$ ) laser.

Both thermal conductivity and specific heat capacity also play an important role in determining the final ablation volume. It is difficult to manipulate these properties without altering the material's optical properties; however, most phantoms are composed primarily of water which has similar thermal properties to tissue. Finally, the thermal damage volume must be observable post-ablation. This can be achieved by sectioning the phantom and quantifying the thermal damage under direct visualization. It is also advantageous to observe the damage volume without disturbing the material via ultrasound or MRI.

Many tissue-mimicking phantoms have been proposed for the analysis of thermal therapy. Negussie et al. reported on a polyacrylamide gel doped with thermochromic ink [209] with color changes correlated with temperature increase. They also demonstrated that the phantom exhibited thermal properties similar to human soft tissue. Zhang et al. developed a similar phantom in which the damage zone was visualized through the coagulation of BSA [210]. BSA is optically transparent in its native state but opaque when coagulated. This phantom was based on prior work by McDonald et al. who demonstrated that the coagulation temperature of BSA can be altered by controlling pH

[211]. Without altering the pH, BSA coagulates in polyacrylamide phantoms at 70°C [212] which is considerably higher than observed during FLA.

McDonald et al. also demonstrated that the coagulation zone can be quantified with T<sub>2</sub>-weighted magnetic resonance imaging (MRI). This was possible in that phantom due to the thermal response of the protein in the BSA. Thermally-induced protein aggregation hinders the rotational averaging of protein dipolar interactions, thus; protein-proton transverse relaxation time is reduced resulting in contrast between native and coagulated states [213]. T<sub>1</sub>-weighted imaging may also be used; however, the T<sub>1</sub> relaxation times for proteins are very long and are not as heavily impacted by protein aggregation.

While all of these phantoms are useful for analyzing thermal damage, none of them have been demonstrated to possess optical properties similar to human tissue and thus they are not suitable for the analysis of FLA. In contrast, Iizuka et al. demonstrated a method for quantifying phantom optical properties and designed an albumin and agar phantom with similar optical properties to human tissue at 805nm [214]. The albumin is a key ingredient as it ensures an increase in  $\mu'_s$  during FLA. In this chapter we use the same method as Iizuka et al. for quantifying phantom optical properties to develop a tissue-mimicking prostate phantom for FLA at 980nm. While the optical properties of prostatic tissue may vary between patients and even within the same patient, we sought to achieve an  $\mu_a$  and  $\mu'_s$  of 0.66cm<sup>-1</sup> and 8.1cm<sup>-1</sup> respectively as these values have been reported for human prostate at 980nm [215]. To our knowledge these are the only published values for  $\mu_a$  and  $\mu'_s$  at 980nm in human prostate; however, they are consistent with other studies in the near-infrared region [198], [207]. In addition, the coagulation-induced increase in scatter in the human prostate has been reported to range from 71-

130% in the near-infrared region [198], [207]. As a result, we elected to design the phantom with a 100% coagulation-induced increase in  $\mu'_s$  ( $\Delta\mu'_s$ ).

In contrast to Iizuka et al., we utilized a polyacrylamide gel doped with BSA to ensure that the coagulation temperature can be adjusted using the pH method demonstrated by McDonald et al. We then demonstrate that the thermal response of the phantom can be measured via interstitial thermal probes and MRT. Quantification of the coagulation zone was demonstrated non-invasively using  $T_2$ -weighted MRI and via direct visualization after sectioning. Finally, we compared our results with our previous clinical trial in which FLA was used for the treatment of prostate cancer [205].

## 5.2. Methods

### 5.2.1. Phantom Construction

Polyacrylamide gel was chosen as the base material for the phantom due to its high melting point, optical transparency, and appropriate thermal properties [209]. The gel was prepared by mixing Acrylamide/bis-acrylamide (19:1 40% w/v, Thermo Fisher Scientific Inc., CA, AM9024) with degassed deionized water. The solution was then doped with various ingredients to change the phantom optical properties. At 980nm, the primary absorbers in tissue are water molecules, oxyhemoglobin and deoxyhemoglobin. As polyacrylamide contains a large quantity of water the  $\mu_a$  of the base material is close to that of prostatic tissue. To match  $\mu_a$  to prostatic tissue, Naphthol Green B (Sigma-Aldrich, MI, N7257-100G) was used as it is readily absorbed in water; thus, resulting in minimal scatter. In contrast Intralipid (20% v/v, Fresenius Kabi, Sweden) was used to increase  $\mu'_s$  as it is an effective scatterer and a weak absorber. Moreover, Intralipid

preferentially scatters light in the forward direction; therefore, phantoms doped with Intralipid will possess  $g$  values similar to soft tissue [216]. Intralipid is a solution of soybean oil (20%), egg yolk phospholipids (1.2%), glycerin (2.25%) and water (76.55%). Phospholipid micelles from the soybean oil scatter light; thus,  $\mu'_s$  can be altered by varying Intralipid concentration [217]. Finally, BSA (30.8% w/v, Boval Co., TX, CF-0020) was used to ensure an increase in  $\mu'_s$  post ablation while also providing contrast for MRI and direct visualization.

To reduce the coagulation temperature of BSA to 60°C, a 0.2M citrate buffer was added to ensure a pH ~ 4.7. The buffer consists of citric acid anhydrous (Sigma-Aldrich, MI, C0759) and sodium citrate tribasic dehydrate (Sigma-Aldrich, MI, S4641). Further details on this method can be found in McDonald et al [211]. To prevent bubbles from appearing in the phantom, the BSA was thoroughly degassed and added after all other ingredients were dissolved in water. Since the polymerization reaction is exothermic, and could cause premature BSA coagulation, the solution was chilled (4-8°C) before adding the initiator. Due to the reduced pH, the widely used combination of TEMED and ammonium persulfate could not be used to initiate polymerization. Instead, polymerization was initiated via a combination of L-ascorbic acid (Sigma-Aldrich, MI, A5960), iron (II) sulfate heptahydrate (Sigma-Aldrich, MI, F7002) and hydrogen peroxide (30% w/v, Sigma-Aldrich, MI, H1009) as previously used by McDonald et al.[211]. . The solution was then immediately poured into 70mm x 70mm x 40mm thin walled (1mm) prefabricated molds, sealed and refrigerated. Table 8 shows the recipe for a 1L phantom without altering the optical properties by addition of Naphthol Green B, Intralipid or BSA. Throughout this paper, the increase in volume due to the addition of BSA and/or



Intralipid addition was offset by a corresponding reduction in water volume; hence, the total volume remained constant.

Table 8: Phantom recipe prior to altering optical properties (1L)

<b>Ingredients</b>	<b>Dosage</b>
Acrylamide/bis-acrylamide (40% w/v)	250ml
Deionized water	744.5ml
Citric Acid Anhydrous	17.063g
Sodium Citrate Tribasic Dehydrate	32.696g
<u>Initiator-Activator</u>	
L-ascorbic acid	1g
FeSO4 (1% w/v)	2.5ml
Hydrogen Peroxide (3% v/v)	3ml

## 5.2.2. Absorption Coefficient as Function of Naphthol Green B Concentration

Naphthol Green B was identified as an appropriate dye to increase the absorption coefficient as it is a known absorber at 980nm. Solutions of Naphthol Green B (0.05%-0.4% w/v) dissolved in water were tested to ensure that FLA would not bleach the dye or otherwise alter the  $\mu_a$ . 7ml of each solution was placed in a test-tube and a 600 $\mu$ m core laser fiber with a 15mm long diffuser (Medtronic, Dublin, Ireland)) was inserted into the center of the tube. Each sample was then exposed to 980nm light at 13.75W for 3 minutes. These parameters were chosen to match those used in a previously conducted clinical trial of prostate cancer FLA to enable comparison with *in vivo* patient data [205]. A spectrophotometer (Agilent 8453 UV-visible Spectroscopy System) was used to measure the absorbance (A) of each solution before and after exposure to the laser light.

By assuming negligible scatter,  $\mu_a$  was calculated using the following formula which can be derived from Beer's Law [218]:

$$\mu_a = \ln\left(\frac{100}{\%T}\right)d \quad (\text{Eqn. 1})$$

where %T is the percentage of light transmitted ( $A = 2 - \log_{10} \%T$ ) and d is the thickness of the cuvette (1cm).

Phantoms doped with increasing concentrations of Naphthol Green B (0%, 0.05%, 0.15%, 0.25% and 0.35% w/v) were manufactured to determine its relationship with  $\mu_a$  using the above method. Five samples of each concentration were prepared by adding Naphthol Green B to the recipe outlined in Table 8. It was anticipated that the initiator, hydrogen peroxide, would bleach the dye; therefore, measurements were made in the polyacrylamide phantom rather than in a dye and water solution. The phantoms were prepared from 20ml solutions, 3ml of which was placed in a cuvette immediately after the addition of the initiator. The cuvettes were then covered and refrigerated. To assess the bleaching effect, the  $\mu_a$  was determined for each sample at 24 hrs., 48 hrs. and 72 hrs.

### 5.2.3. Method of Measuring the Reduced Scattering Coefficient

The apparatus shown in Figure 28 was used to measure the  $\mu'_s$  as previously demonstrated by Iizuka et al [214]. In contrast to Iizuka et al, measurements were taken after polymerization. It consists of a 3D printed testing chamber, a point source probe (Pioneer Optics, Bloomfield, CT) connected to a 980nm diode laser (Photex Inc, Houston, TX), a micrometer-controlled translation stage (Thorlabs, Newton, NJ) and a dosimetry

probe (Pioneer Optics, Bloomfield, CT) connected to an amplified photodetector (PDA36A, Thorlabs, Newton, NJ).

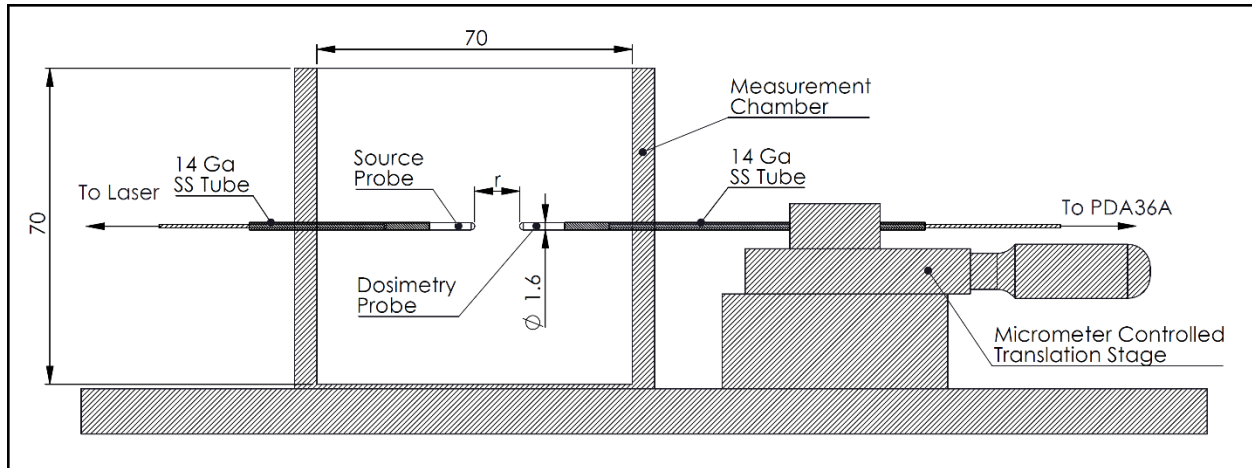


Figure 28: Apparatus used to quantify  $\mu'_s$ . Phantoms were cast in 70mm x 70mm x 40mm thin walled (1mm) containers with holes for the source and dosimetry probes. During testing the container holding the phantom is placed in the measurement chamber before inserting the probes

Each of the probes consists of a 400 $\mu$ m optical fiber with a polycarbonate case attached to the distal 20mm (Figure 29). The fiber terminates inside the polycarbonate immediately proximal to titanium dioxide powder. The powder scatters light in all directions; therefore, ensuring that the probe can act as either an isotropic point source or an isotropic point detector. The polycarbonate case is press-fit into a stainless tube and the fiber is secured proximally with a Tuohy Borst adapter and Luer lock.

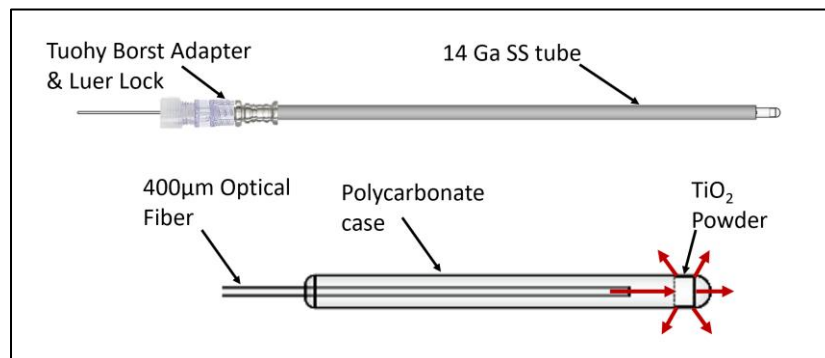


Figure 29: Design of the isotropic point source/detector probes.

As depicted in Figure 30, the light detected by the dosimetry probe is transmitted to an amplified photodetector which outputs a voltage in the range 0-10V. A voltage divider is used to reduce the range to 0-5V so that an Arduino Leonardo (Arduino LLC, Italy) can be used for analog to digital conversion. The digital signal is then transmitted to a PC over USB where custom-built software (Python) facilitates real-time data visualization and recording.

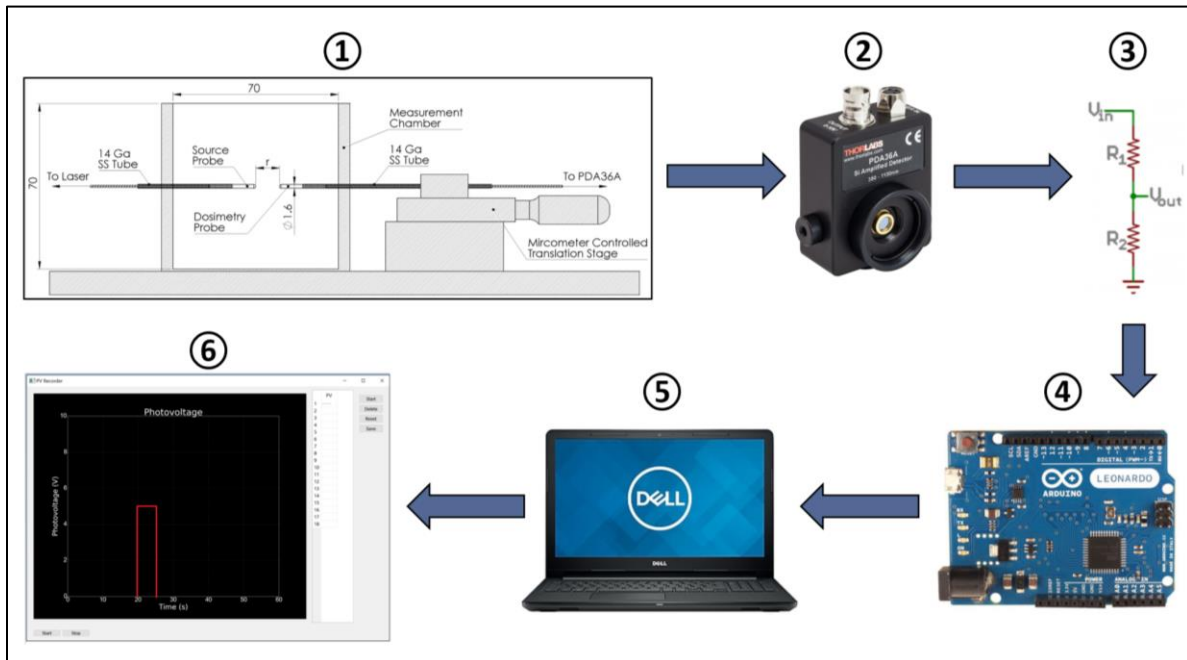


Figure 30: 1-Fluence box apparatus, 2 – Amplified photodetector, 3 – voltage divider, 4 – Arduino Leonardo, 5 – PC and 6 – Custom-built software

Using custom-built software and a microcontroller (Arduino Leonardo, Arduino LLC, Italy), the photovoltage (V) was recorded every 500 $\mu$ m as the dosimetry probe was advanced towards the source probe. These data were then used to calculate the effective attenuation ( $\mu_{eff}$ ) coefficient as the fluence rate ( $\phi$ ) for an isotropic point source radiator is given by [218]:

$$\phi(r) \propto \frac{\exp(-\mu_{eff}r)}{r} \quad (\text{Eqn. 2})$$

where  $r$  is the distance between the source and detector. Given that  $V \propto \phi$ , the magnitude of the slope of  $\ln(V \cdot r)$  vs  $r$  is the  $\mu_{eff}$ . As  $\mu_a$  is known, the  $\mu'_s$  can then be determined using the following definition of  $\mu_{eff}$  [218]:

$$\mu_{eff} = \sqrt{3\mu_a \cdot (\mu_a + \mu'_s)} \quad (\text{Eqn. 3})$$

The apparatus was calibrated against a spectrophotometer using a non-scattering medium as there was no material with a known  $\mu'_s$  available. Briefly, 300ml phantoms doped with Naphthol Green B (0-0.35%) were manufactured and poured into custom designed 3D printed boxes prior to polymerization. 3ml of each solution was also placed in cuvettes for spectrophotometric analysis.  $\mu_{eff}$  was determined from absorbance using Eqn. 1, Eqn. 2 and assuming that  $\mu_a \gg \mu'_s$ . A standard 2-point calibration was then performed using the phantoms with 0% and 0.35% Naphthol Green B.

#### **5.2.4. Reduced Scattering Coefficient as a Function of BSA & Intralipid Concentration**

Phantoms doped with 0.144% (w/v) Naphthol Green B (derived optimal concentration) and 12.5%, 25% and 37.5% (v/v) BSA were manufactured in triplicate. The phantoms were cast in thin walled containers with openings to facilitate two measurements in the fluence box apparatus (Figure 28). The two measurement sites are separated by 23mm which is sufficient to ensure that an existing needle track will not affect the second measurement. Due to the bleaching effect previously observed, testing was performed ~48hrs after initiation of polymerization. The  $\mu'_s$  was determined for each phantom at

room temperature. The phantoms were then placed in plastic bags to prevent water absorption and submerged in a water bath for 2hrs at 70°C. This was found to be sufficient to raise the temperature of the entire phantom above 65°C; thus, ensuring coagulation throughout the volume. The  $\mu'_s$  was then quantified again using a different section of the phantom. The optimal concentration of BSA was defined as the concentration that results in  $\Delta\mu'_s$  of 8.1cm<sup>-1</sup> (a 100% increase  $\mu'_s$ ).

BSA causes minimal scatter in its native state, thus the addition of Intralipid was required to achieve the desired  $\mu'_s$  of 8.1 cm<sup>-1</sup> in the native state. A second set of phantoms was manufactured in triplicate containing 0.144% Naphthol Green B (derived optimal concentration), 31.4% BSA (derived optimal concentration) and increasing concentrations of Intralipid (0%, 5%, 10%). The  $\mu'_s$  was determined in the native and coagulated states following the same protocol outlined for the BSA only phantoms.

### **5.2.5. Testing Optimized Phantom**

The derived phantom recipe was used to create eight optimized phantoms. Five of these phantoms were used to determine  $\mu'_s$  in the native and coagulated states following the same protocol as used previously. The remaining three phantoms were tested to assess the thermal response under the same conditions previously used in a clinical trial [205]. The trial utilized components from an existing magnetic resonance-guided laser ablation system (Medtronic, Dublin, Ireland) along with magnetic resonance - ultrasound fusion guidance via the Artemis® device (Eigen, Grass Valley, California). The key components were a 15W 980nm laser (BioTex, Houston, Texas), a 600  $\mu$ m core laser fiber (Medtronic, Dublin, Ireland), K-pump surgical infusion pump (K.M.I., Corona, California), Uro-kit 600 dual lumen catheter (Medtronic, Dublin, Ireland), Fluoroptic® thermal probes

(Lumasense, Santa Clara, California) and a custom-fabricated needle guide. Figure 31A depicts the clinical setup in which the laser fiber housed in a saline cooled dual lumen catheter was inserted into the target. The procedure was monitored via a thermal probe placed level with the catheter tip and at a radial distance of 8mm. Figure 31B elucidates the phantom experimental setup designed to match the clinical procedure. The experiment utilizes the same laser fiber, dual lumen catheter, infusion pump and thermal probe. Component placement was achieved using a custom-fabricated insulated box with needle tracks placed 8mm apart. Prior to being placed in the box, phantom temperature was raised to  $37 \pm 1$  °C using a water bath. FLA was performed for 3 min. at 13.75 W, matching parameters of the clinical trial. In contrast to the clinical trial, the experiment was simultaneously monitored via gradient echo magnetic resonance thermometry to demonstrate the utility of the phantom for the development of MRT sequences.

Measurement of the coagulation zone was then demonstrated using MRI and direct visualization. Immediately after laser deactivation, a high resolution T2-weighted turbo spin echo image was acquired (echo time = 52ms, repetition time = 2000ms, resolution =  $0.5 \times 0.5 \times 1 \text{mm}^3$ ) using a 3T scanner (Prisma, Siemens). Alignment of the imaging plane with the fiber trajectory was achieved using a fiducial marker within the insulated box. The fiducial marker consisted of a  $2 \times 2 \text{mm}^2$  water-filled channel circumscribing the phantom. Following laser application, the phantom was sliced in half along the fiber trajectory and photographed.

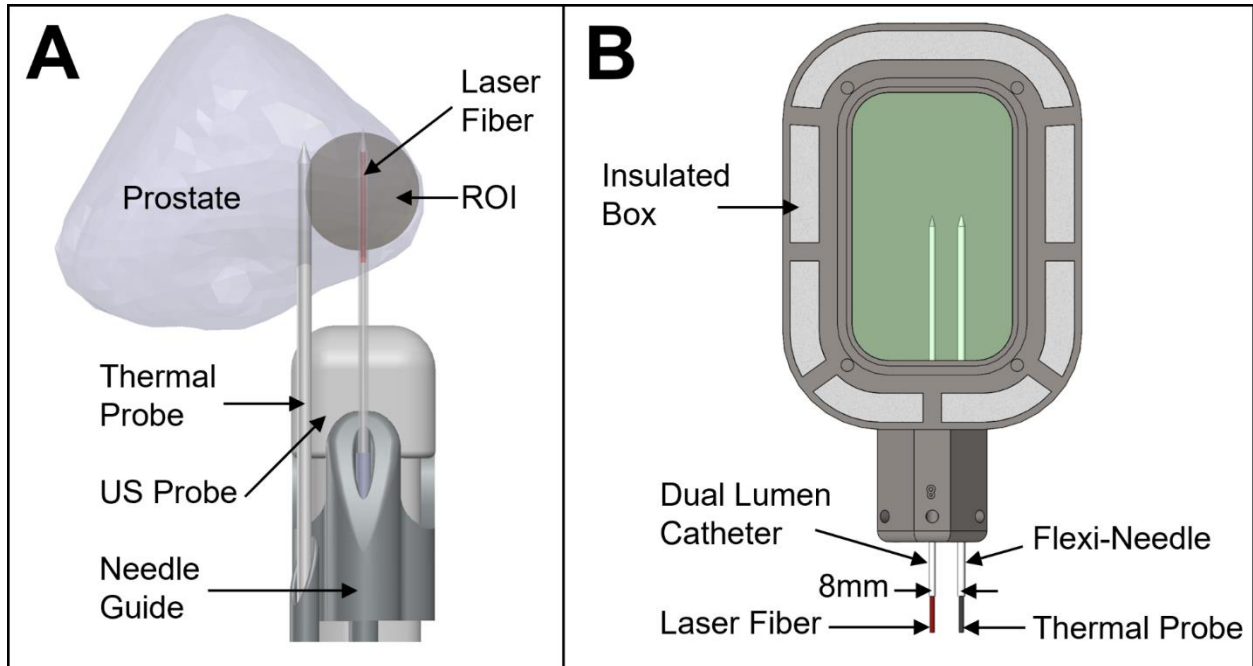


Figure 31: A) Clinical setup during MR-US fusion guided FLA for the treatment of prostate cancer. FLA was performed in the region of interest (ROI) for 3 min. at 13.75W with a 980nm laser. A thermal probe was used to record temperature. B) Experimental setup mimicking clinical conditions. The phantom was heated to 37°C in a water bath prior to being placed in the insulated box. FLA was performed using the same equipment and configuration used clinically

## 5.3. Results

### 5.3.1. Absorption Coefficient

The effect of photobleaching was examined by comparing  $\mu_a$  before and after FLA in Naphthol Green B and water solutions (Figure 32). The difference in  $\mu_a$  was found to be negligible at all concentrations (mean absolute error = 0.035  $\text{cm}^{-1}$ ); therefore, it can be assumed that Naphthol Green B will not photobleach during FLA. In polyacrylamide phantoms, a non-linear relationship was observed between Naphthol Green B concentration and  $\mu_a$  (Figure 33). This was previously observed by Iizuka et al [214], who attributed this effect to bleaching induced by the initiator, ammonium persulfate (APS). They found that bleaching only occurs during the first 2 hours after the addition of APS.



In contrast, hydrogen peroxide was used as the initiator in our phantoms and appears to cause bleaching beyond 24hrs. No further bleaching was observed after 48 hours. The requisite concentration of Naphthol Green B to achieve the desired  $\mu_a$  of  $0.66 \text{ cm}^{-1}$  was determined by interpolating the data from the 48hr and 72hr measurements. It was found that 0.144% Naphthol Green B results in an  $\mu_a$  of  $0.66 \pm 0.06 \text{ cm}^{-1}$ .

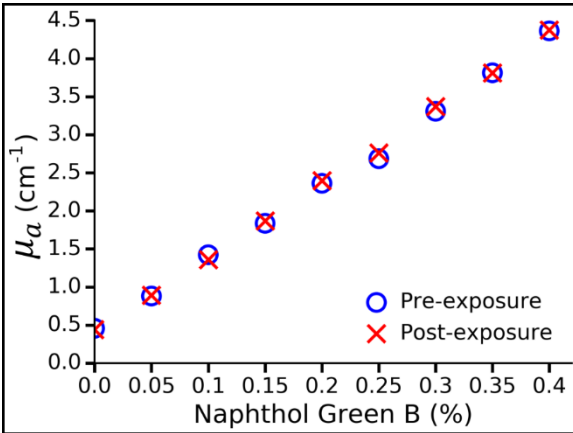


Figure 32: The effect of photobleaching in Naphthol Green B/water solutions at 980nm. No change was observed as a result of laser exposure

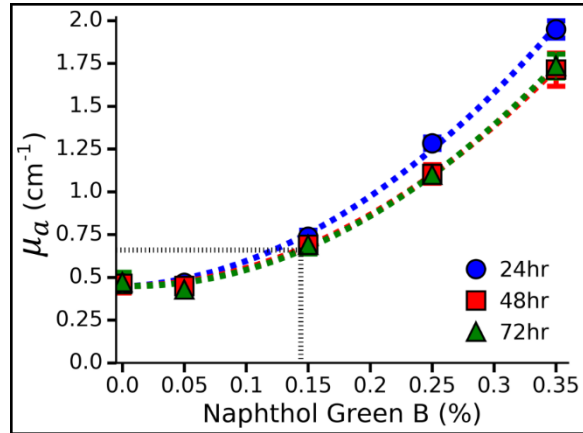


Figure 33:  $\mu_a$  as function of Naphthol Green B concentration at 980nm in polyacrylamide gel.  $\mu_a$  was determined by a spectrophotometer at 24, 48 and 72 hours. No further bleaching was observed after 48 hours. By interpolation (dashed black line), a 0.144% concentration of Naphthol Green B was found to provide the desired  $\mu_a$  of  $0.66 \text{ cm}^{-1}$ .

### 5.3.2. Reduced Scattering Coefficient

Prior to determining the reduced scattering coefficient, the fluence box was calibrated against a spectrophotometer.  $\mu_{eff}$  measured by the fluence box was linear ( $r^2 = 0.998$ ) throughout the measurement range. After standard 2-point calibration was applied,  $\mu_{eff}$  measured by the fluence box and spectrophotometer was equivalent (mean absolute error =  $0.033 \text{ cm}^{-1}$ ).

Figure 34A shows the data measured by the fluence box in order to calculate  $\mu'_s$  for a set of phantoms doped with various concentrations of BSA before and after coagulation. The slope of the curves gives  $\mu_{eff}$  which was used to generate Figure 34B as previously described (Eqn. 2). Figure 35 shows the corresponding curves for phantoms doped with the optimal concentration of BSA and increasing concentrations of Intralipid. All measurements were taken at least 48 hours after adding the initiator to ensure that the bleaching effect had subsided. As expected, the presence of BSA ensures a coagulation-induced increase in  $\mu'_s$  with 31.4% BSA providing the desired  $\Delta\mu'_s$  of 8.1  $\text{cm}^{-1}$ . In the native state the target  $\mu'_s$  is also 8.1  $\text{cm}^{-1}$  which is achieved by adding 8.06% Intralipid. Interestingly, Intralipid also appears to have some effect on the coagulation-induced increase in  $\mu'_s$ .

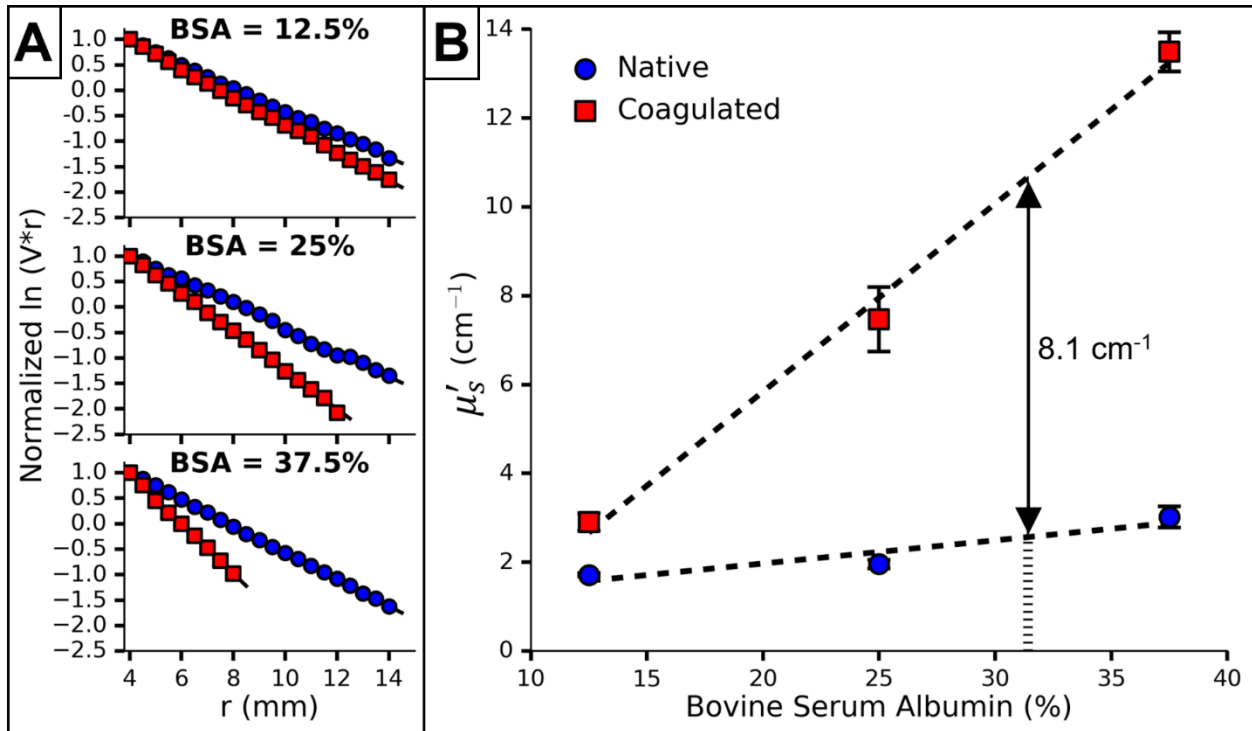


Figure 34: A) Normalized  $\ln(V \cdot r)$  vs  $r$  for a single set of phantoms doped with 12.5%, 25% and 37.5% BSA and 0.144% Naphthol Green B. B) The effect of BSA concentration on  $\mu'_s$  before and after coagulation measured in 3 sets of phantoms. Given the desired coagulation-induced change in  $\mu'_s$  of  $8.1 \text{ cm}^{-1}$ , the requisite concentration of BSA was found to be 31.4%. Error bars represent one standard deviation and are not visible at all points

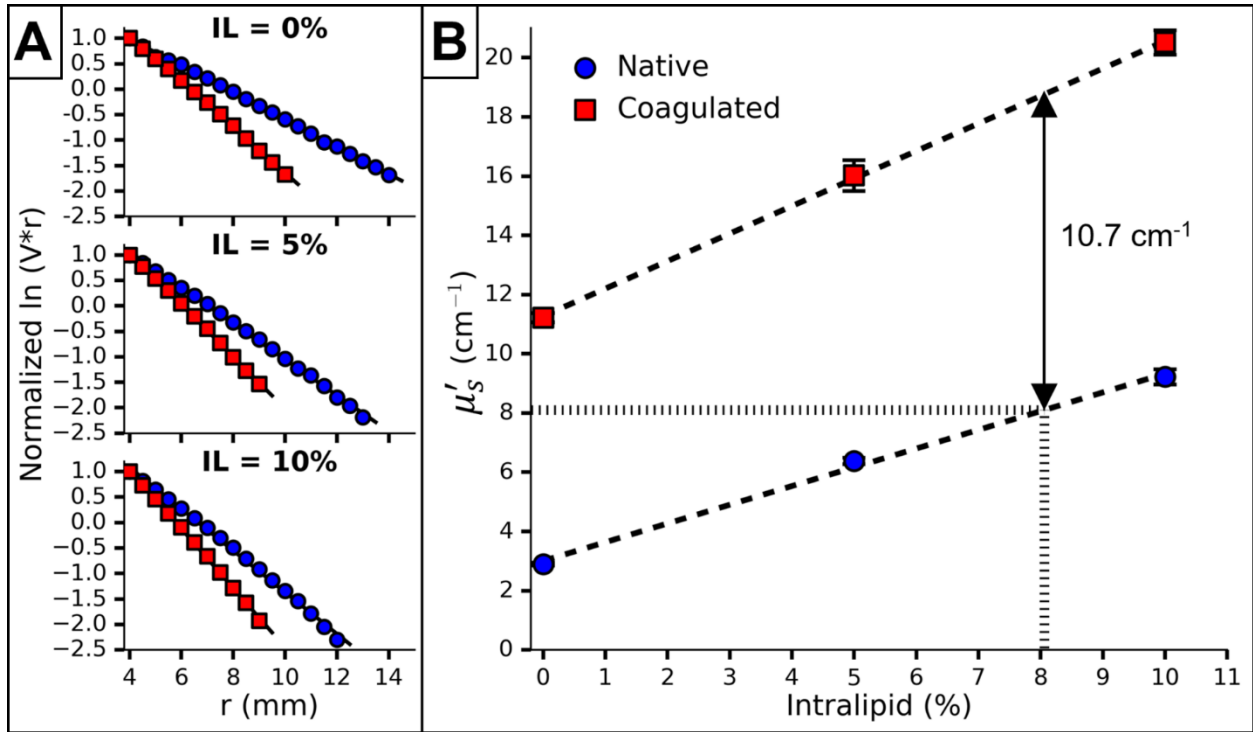


Figure 35: A) Normalized  $\ln(V \cdot r)$  vs  $r$  for a single set of phantoms doped with 0%, 5% and 10% Intralipid (IL), 0.144% Naphthol Green B and 31.4% BSA. B) The effect of Intralipid and BSA concentration on  $\mu'_s$  before and after coagulation measured in 3 sets of phantoms. By interpolation, the requisite concentration of Intralipid was found to be 8.06%. Error bars represent one standard deviation and are not visible at all points

Incorporating optimized concentrations for BSA and Intralipid yielded a final phantom recipe (Table 9) which was subsequently characterized in the same manner as before (Figure 36). The optical properties are summarized in Table 10. The mean  $\Delta\mu'_s$  across the five tested samples was  $113 \pm 11\%$ .

Table 9: Tissue-mimicking phantom recipe (1L)

Ingredients	Dosage
Acrylamide/bis-acrylamide (40% w/v)	250ml
Deionized water	349.9ml
Naphthol Green B	1.44g
Intralipid (20%)	80.6ml
BSA (30.6%)	314ml
Citric Acid Anhydrous	17.063g
Sodium Citrate Tribasic Dehydrate	32.696g
<b>Initiator-Activator</b>	
L-ascorbic acid	1g
FeSO4 (1% w/v)	2.5ml
Hydrogen Peroxide (3% v/v)	3ml

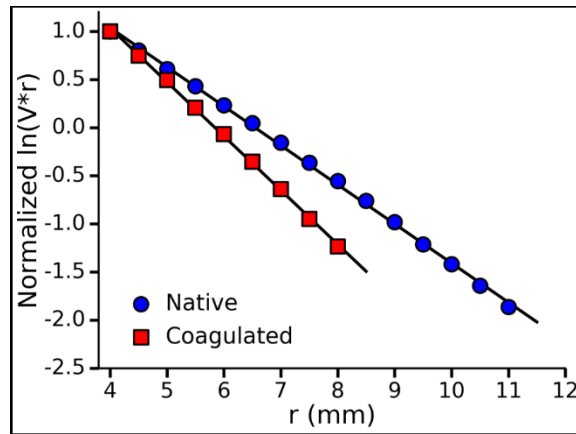


Figure 36: Normalized  $\ln(V \cdot r)$  vs  $r$  for a single optimized phantom before and after coagulation. A total of five phantoms were tested and one standard deviation was used to quantify the uncertainty in the measured optical properties shown in Table 10.

Table 10: Optical properties of tissue-mimicking phantom

	$\mu_a$ ( $\text{cm}^{-1}$ )	$\mu'_s$ ( $\text{cm}^{-1}$ )
Native	$0.66 \pm 0.06$	$8.27 \pm 0.50$
Coagulated	$0.66 \pm 0.06$	$17.63 \pm 1.41$

### 5.3.3. Thermal Response

Figure 37 compares the thermal response of the phantom to a patient under the same conditions. The temperature was recorded at radial distance of 8mm from the laser fiber in both cases. After 180s, the laser was deactivated and the maximum temperature was found to be  $64.1\pm 0.9^{\circ}\text{C}$  and  $66.9^{\circ}\text{C}$  in the phantom and patient respectively. The temperature dropped rapidly following laser deactivation, reaching  $60^{\circ}\text{C}$  in 10s and  $44\pm 5\text{s}$  for the patient and phantom respectively.

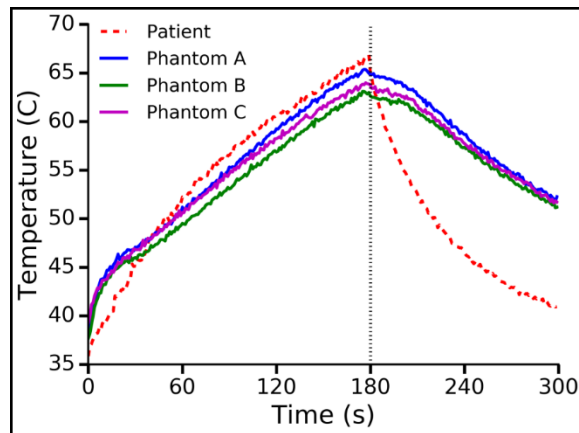


Figure 37: Temperature at a radial distance of 8mm from the laser as measured in a patient and three phantoms.

Figure 38(A-C) demonstrates the utility of the phantom as a robust platform for the development of MRT sequences for monitoring FLA. Thermal maps were calculated from phase maps acquired during the procedure. The zone of elevated temperature was localized around the laser fiber as expected. The growth of this zone was evident as the procedure progressed. Additionally, the maximum temperature recorded in each of the three phantoms was  $98.8^{\circ}\text{C}$ ,  $99.2^{\circ}\text{C}$  and  $99.7^{\circ}\text{C}$ .

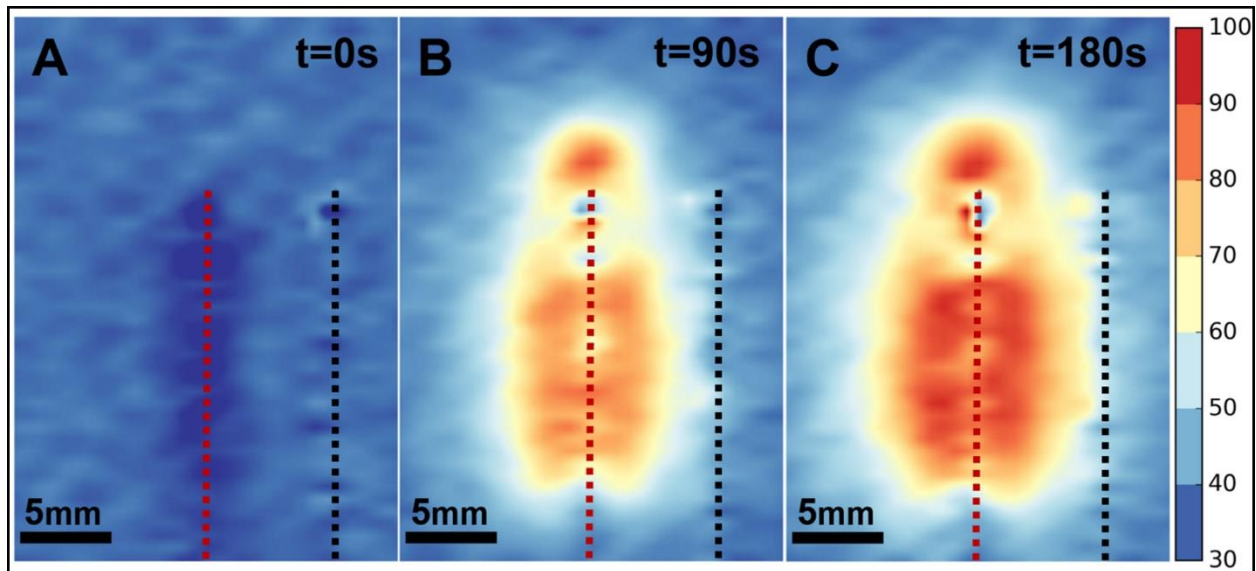


Figure 38: Absolute temperature ( $^{\circ}\text{C}$ ) during FLA of the optimized phantom as determined by MRT at 0 (A), 90 (B) and 180 (C) seconds after laser activation. The location of the laser fiber (dashed red line) and thermal probe (dashed black line) are marked

### 5.3.4. FLA Induced Coagulation

Figure 39 compares the induced coagulation zone in (A) a patient, (B) a phantom under  $T_2$ -weighted MRI, and (C) a phantom under direct visualization. The experiment was performed on three phantoms and in all cases the coagulation zone approximates an ellipse. The major and minor axes for the phantom were  $2.65 \pm 0.03\text{cm}$  and  $1.6 \pm 0.05\text{cm}$  on MRI and  $2.58 \pm 0.03\text{cm}$  and  $1.52 \pm 0.01\text{cm}$  under direct visualization. A similar coagulation zone was observed clinically with major and minor axes of  $2.44\text{cm}$  and  $1.51\text{cm}$  respectively.

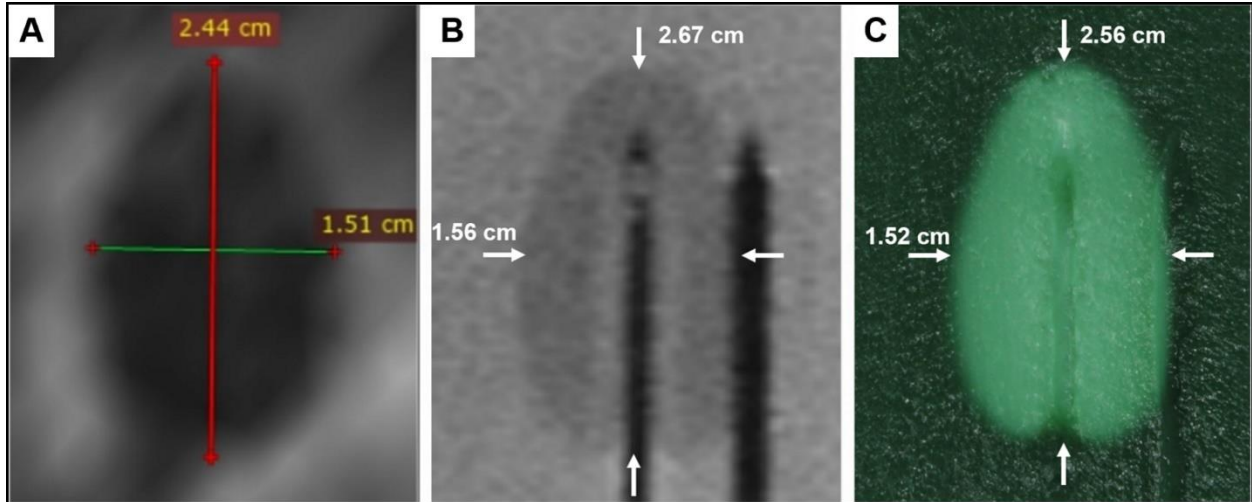


Figure 39: A) Zone of coagulative necrosis in a patient as indicated by non-perfused tissue. The scan was acquired immediately after the patient received FLA for 3 min. at 13.75W. Further information can be found in Natarajan et al (2017)1. B) Phantom coagulation zone under T2-weighted MRI showing major and minor axes (white arrows). Note that the catheters in the center and on the right contain the laser fiber and thermal probe respectively. C) Phantom coagulation zone under direct visualization showing major and minor axes (white arrows). Note the needle tracks in the center and to the right.

## 5.4. Discussion

We have developed a novel tissue-mimicking phantom with similar optical and thermal properties to human prostatic tissue. The relationship between phantom ingredients and optical properties was determined empirically using fluence measurements and light diffusion theory. In the native state  $\mu_a$  and  $\mu'_s$  have been reported as  $0.66\text{cm}^{-1}$  and  $8.1\text{cm}^{-1}$  in human prostate at 980nm [215]. In addition, FLA causes coagulative necrosis leading to an increase in  $\mu'_s$  which is expected to lie in the range of 71-130% [198], [207]. To mimic these properties the requisite concentrations of Naphthol Green B, Intralipid and BSA were quantified and found to be 0.144%, 31.4% and 8.06% respectively which resulted in  $\mu_a$  and  $\mu'_s$  of  $0.66\pm 0.06\text{cm}^{-1}$  and  $8.27\pm 0.5\text{cm}^{-1}$  in the native state. After coagulation  $\mu'_s$ , increased to  $17.63\pm 1.41$  which corresponds to an increase of 113%. The

phantom optical properties therefore correspond to the expected values of prostatic tissue at 980nm. In addition, the phantom coagulation threshold was matched to tissue (~60°C) by reducing pH to 4.7 as outlined in a previous study [211]

The measured change in  $\mu'_s$  after coagulation is higher than predicted as we assumed that the coagulation-induced increase in  $\mu'_s$  was solely due to BSA protein coagulation and independent of Intralipid. This assumption was found to be incorrect as the presence of Intralipid led to a relatively small increase in the coagulation induced change in  $\mu'_s$ . This was not anticipated but may be due to interaction between the two substances. Indeed, earlier studies have shown that fatty acid alters the BSA denaturation process [219], [220]. Moreover, in our calculations we have assumed that  $\mu_a$  remains constant during laser exposure. While we demonstrated that this is true for the absorbing agent Naphthol Green B, when dissolved in water, it is possible that interactions with other ingredients results in an alteration of  $\mu_a$ . This is unlikely as it has previously been demonstrated that the effect of dyes dissolved in water on  $\mu_a$  is independent of scattering introduced by Intralipid [221]-[223]. While the assumption is frequently made when designing tissue mimicking phantoms, it could be verified using alternative techniques such as the inverse adding doubling method [224]. Nevertheless, the measured increase in  $\mu'_s$  is similar to previously reported values for prostatic tissue in the near-infrared region [198], [207]. In the limited number of human prostate samples studied, the maximum coagulation-induced increase in  $\mu'_s$  was 130%, while 272% was reported for canine studies with a much larger sample size.

It should also be noted that in contrast to a previous study by Iizuka et al. [214], we were able to measure the optical properties after polymerization; thus, chemical reactions with the initiator have been accounted for. This greatly reduces measurement



uncertainty as the initiator contains hydrogen peroxide which bleaches Naphthol Green B resulting in a decrease in  $\mu_a$  after polymerization. For some studies it may be desirable to increase the BSA content in an effort to achieve a greater post-coagulation increase in  $\mu'_s$ . While this is possible, we limited BSA concentration to 37.5%, as higher concentrations resulted in the formation of large bubbles.

The thermal response of the phantom was compared to previously acquired clinical data. The maximum temperature observed clinically was 66.9°C while the phantom peaked at 64.2±0.9°C at the same location. Interestingly, after laser deactivation, the temperature drops to 60°C, the theorized damage threshold, 44s earlier in the patient. Given this relatively short timeframe it is likely that there is only a minor increase in coagulation volume as minimal damage occurs during the cooling phase [225]. This variation in the rate of cooling is likely due to the absence of perfusion in the phantom as well as possible disparity in active cooling. Perfusion has been shown to affect both the volume of thermal damage and the temperature distribution during FLA [226]. In addition, further active cooling is provided by continuous circulation of water through the dual lumen catheter; however, the flow rate and temperature were not precisely controlled. Positioning of the thermal probe was also a challenge in the clinical setting. A needle guide was used to aid in placement; however, the needle was susceptible to deflection when passing through the prostatic tissue. Additionally, in the clinical study, the distal section of the thermal probe was covered with a thin copper film to prevent laser light from interfering with the thermal measurement. This occurs as the thermal probe relies on fluoroptic technology in which the temperature is determined based on the decay rate of a phosphor element at the tip of the probe. The decay rate is assessed using a photodiode sensitive to 980nm light. In our MRI

experiments the copper film was removed and an in-line filter was used to remove the offending light. This approach was taken as the copper film would likely cause an artifact on MRI. The absence of the copper film may also explain the initial rapid heating observed in the phantom as light can be absorbed directly by the Tefzel jacket covering the thermal probe. Likewise, the rate of cooling in the clinical setting may have been faster as the copper film rapidly conducts heat away from the sensor tip after laser deactivation.

We also demonstrated that the thermal response during FLA can be monitored via MRT as shown in previous clinical trials [11], [192]. The data from the MRT images facilitates analysis of the thermal response throughout a single plane. At the end of FLA, data from the MRT images shows that the temperature near the fiber is approximately 100°C with a maximum temperature of 99.7°C. This was expected and correlates with clinical experience in which char is frequently observed on the dual lumen catheter after removal. Despite the high temperatures, the phantom does not appear to melt. While we did not measure the melting point, a previous study found the melting point of similar polyacrylamide phantoms to be 113°C [227].

Finally, the FLA-induced coagulation zone was compared to that found clinically. In the phantom, the induced coagulation zone was readily apparent under T<sub>2</sub>-weighted MRI and direct visualization after sectioning along the laser fiber trajectory. It was found to be quantitatively and qualitatively similar to the non-perfused region observed on a contrast-enhanced MRI acquired immediately after a patient received FLA for the treatment of prostate cancer. Moreover, the MRT derived temperature map acquired during FLA of the phantom (Figure 38) appears to correlate with the coagulation zone identified in both the patient and phantom (Fig. 10). This suggests that the phantom

provides a useful platform for studying the effect of procedure parameters on the resulting coagulation zone and also for development of feedback techniques including MRT.

The advantages of this phantom over *ex vivo* tissue are numerous. It is homogenous, reproducible, and easy to work with as it is not a biohazard, unlike cadaveric tissue. It should be noted that acrylamide monomers are toxic; therefore, safety procedures must be adhered to during fabrication. After polymerization the risk is substantially reduced; however, nitrile gloves should still be worn due to the possibility of residual monomers. A key advantage of this phantom is the ability to accurately quantify the coagulation zone. This can be achieved via either direct visualization or T<sub>2</sub>-weighted MRI. Given this characteristic, the phantom should find utility in both the development and characterization of focal laser ablation systems. Finally, the thermal and optical properties of the phantom are similar to human prostate; thus, the phantom provides a useful platform for the development of monitoring modalities such as magnetic resonance thermometry and interstitial thermal probes.

Like many other phantoms a lack of perfusion is the primary limitation of this model; therefore, this phantom is likely to find utility as a substitute for *ex vivo* rather than *in vivo* studies. In addition, the phantom does not account for *in vivo* factors such as the urethra, prostate capsule, prostate stones or capsular cooling. Consequently, the phantom should not be used for direct pre-treatment planning. It should also be noted, that while every effort was made to match the phantom's optical properties to human prostate, batch to batch variation in the optical properties of Naphthol Green B, Intralipid and BSA was not considered in our analysis. This potential variation is likely to be minor and have a limited impact on the phantom's thermal response. Finally,



knowledge of  $g$  and  $\mu_s$  are important for Monte Carlo modelling but could not be determined due to the employed method of measuring the optical properties. This limitation can be overcome by assuming  $g=0.74$  as previously reported for Intralipid [216]. This assumption must be utilized with some caution as the effect of BSA coagulation on  $g$  is unknown.

To our knowledge this is the first phantom with all of the following characteristics: (1) optical properties matched to bulk prostatic tissue at 980nm, (2) thermal response similar to clinical data, and (3) visualization of the induced damage zone via MRI and direct visualization. These characteristics make this phantom ideal for the development and characterization of tools for focal laser ablation at 980nm.

In chapter 4, we performed FLA experiments using ex vivo bovine muscle as a prostate model. In general, ex vivo tissue is difficult to work with because it is excessively pliable. As a result, it is challenging to insert the catheters and probes without compressing the tissue. It is also difficult to slice the tissue along the trajectory of the laser fiber. Even, if correctly sliced, the tissue is likely to expand after it is sliced; therefore, the size of ablation zone cannot be accurately measured. In addition, it is difficult to delineate the ablation boundary via direct visualization while there is no obvious contrast mechanism for MRI. Finally, the optical properties are unknown and inconsistent due to both inter and intra-sample variation which naturally results in variation in the size of the ablation for a given set of laser exposure parameters. Due to this variation in optical properties and the inability to non-invasively monitor the ablation zone with MRI, it is impossible to demonstrate the utility of optical monitoring as the optical signal cannot be correlated with the growth of the ablation zone. As outlined in Table 11, all of these limitations have been successfully addressed through

the development of the tissue mimicking phantom. Consequently, it is now possible to proceed with development and validation of an interstitial optical monitoring system.

Table 11: Tissue mimicking prostate phantom vs ex vivo tissue

	<b>Phantom</b>	<b>Ex vivo tissue</b>
<b>Optical properties</b>	Matched to prostate	Unknown
<b>Damage visualization</b>	Direct + MRI	Direct (unclear boundary)
<b>Repeatable</b>	Yes	No
<b>Appearance</b>		

## 5.5. Conclusion

A tissue mimicking phantom was developed to facilitate the study of FLA at 980nm in prostatic tissue. The thermal and optical properties of the phantom were designed to match human prostatic tissue. As a result, the thermal response of the phantom was consistent with that observed clinically. The induced coagulation zone can be observed directly or via  $T_2$ -weighted MRI. Furthermore, FLA-induced coagulation is both qualitatively and quantitatively similar to that observed in *in vivo* human prostate. This phantom provides a useful platform for the development and optimization of FLA techniques including monitoring modalities such as interstitial probes and MRT. Indeed, this phantom provides the necessary platform for testing our hypothesis that interstitial optical probes can be used to monitor FLA. In the next chapter, we will outline the

development of an optical monitoring system and perform initial validation using the tissue mimicking phantom.

# CHAPTER 6

## Development of an Interstitial Optical Monitoring System

### 6.1. Introduction

Foal laser ablation offers a minimally invasive approach for the treatment of cancer and has been used in many organs including prostate [11], [29], [73], breast [74], liver [75], lung [76] and brain [77]. During FLA, a laser fiber is inserted into the target tumor and oncologic control is achieved via thermally induced coagulative necrosis. Successful treatment is contingent upon inducing coagulative necrosis throughout the target volume; therefore, treatment monitoring is critical. Magnetic resonance imaging is frequently employed for this purpose as it can be used to guide the laser fiber to the target and monitor thermal changes via magnetic resonance thermometry. For example, in a recent study, FLA was performed on 120 patients with prostate cancer and monitored with MRT [6]. At one year follow up there was an 83% freedom of retreatment rate and the median procedure time was 122 minutes (range, 60-250 minutes). While the clinical results are promising the high cost associated with extended use of MRT is a major barrier to the widespread adoption of FLA in oncology. As a result, there are ongoing efforts to develop interstitial probes capable of monitoring FLA in real time. These efforts have largely focused on the use of interstitial thermal probes consisting of either thermocouples [98], [99] or fluoroptic probes [29], [73], [205].

Given that FLA achieves cancer control through hyperthermia, it seems logical to monitor temperature; however, raw thermal data is of limited utility for predicting cellular death. Instead thermal data is generally used in conjunction with the Arrhenius thermal damage model [11], [228], [229]. The model predicts cell death based on thermal history i.e. taking into account both the magnitude and duration of hyperthermia. Tissue specific kinetic parameters are also required inputs for the model and have proven to be difficult to quantify. Indeed, due to the variation in estimated kinetic parameters the Arrhenius model may be inherently inaccurate when monitoring FLA. Moreover, a recent study found that the Arrhenius model overestimates the extent of thermal necrosis when compared to histopathology and  $T_1$ -weighted contrast enhanced MRI [132]. Consequently, there is a need to develop alternative interstitial probes that do not rely on thermal data and inaccurate damage models.

In this chapter we outline the development of an interstitial optical monitoring system that monitors laser-tissue interaction during FLA. Previous work by Whelan et al demonstrated that in contrast to interstitial thermal probes an interstitial optical probe can detect the onset and propagation of thermal coagulation during FLA [188]. Further publications by the same group utilized monte carlo modelling to characterize laser tissue interaction during FLA to demonstrate the potential of optical monitoring [189], [230]. As outlined in chapter 4, coagulation is characterized by an increase in the reduced scattering coefficient and therefore a decrease in the optical penetration depth which results in a corresponding decrease in optical intensity recorded by an interstitial optical probe. To our knowledge no study has empirically demonstrated the utility of optical monitoring due to an inability to visualize the propagation of the coagulation zone and quantify the coagulation radius as function of time. The tissue mimicking phantom



presented in chapter 5 was specifically designed to overcome this limitation and thus facilitate temporal registration of the optical response and the coagulation radius.

We begin with a detailed description of the prototype optical monitoring system. The performance of four optical probe designs are then assessed using the tissue mimicking phantom which simulates the optical properties of prostatic tissue during FLA. In contrast to previous work, growth of the coagulation is monitored in near real-time via  $T_2$ -weighted MRI. This enables correlation of optical probe data with the coagulation radius. Finally, we demonstrate the utility of the system in an *ex vivo* bovine muscle model under the same conditions used in a previous clinical trial [205].

## **6.2. System Design**

### **6.2.1. System Requirements**

The optical monitoring must be capable of minimally invasively monitoring light intensity at a predefined location deep within the target tissue. The measured signal must be recorded, displayed and analyzed in real-time. To this end the key components that must be developed are: 1) an interstitial optical probe, 2) hardware for optical to digital signal conversion, and 3) software for real-time analysis.

a software package capable of analyzing the resulting signal.

The following design requirements were identified for the interstitial optical probes:

1. Light Collection & Delivery:

The probe must be able to collect light at a known location near the probe tip. In the clinical setting, the interstitial optical probes and laser fiber are inserted parallel to each other using a needle guide; therefore, it is necessary to be able to

collect light travelling perpendicular to the long axis of the probe. This precludes the use of a simple bare cut fiber in which light primarily enters the fiber parallel to the long axis. Collected must then be transferred from the probe tip to a photodiode with minimal loss.

2. MR safe:

While clinically the system is expected to be used in an office setting, testing and validation will be performed under MRI surveillance; thus, the probes must be MR safe. Consequently, to prevent torqueing and susceptibility artifacts, the probes cannot contain ferromagnetic components. Additionally, the photodiode must be placed sufficiently far from the scanner to minimize both the interference and attractive force of the magnetic field. Five meters from isocenter was deemed sufficient.

3. Probe diameter:

In our clinical trial (Chapter 3), the largest needle used was a 13Ga flexi-needle. This corresponds to an outer diameter of 2.413mm; therefore, this value was chosen as the maximum probe diameter.

4. Mechanical Properties:

Although not explicitly measured, the probe must be rigid to facilitate insertion without flexion. These probes were designed primarily for use with a soft hydrogel tissue mimicking phantom; therefore, while sharp tips are required, they do not need to meet the requirements of a typical needle.

5. Thermal Properties:

During testing of the tissue mimicking phantom under magnetic resonance thermometry (Chapter 5) the maximum temperature recorded was 99.7°C but this

occurs close to the fiber. The interstitial probes will be tested at radii of 4mm, 5mm, 6mm and 7mm where maximum temperatures were observed to be 86°C, 77°C, 60°C and 65°C respectively. The probe must remain thermally stable at these temperatures; therefore, the melting point of the probe materials must be greater than 86°C.

The following hardware requirements were identified:

1. Optical to analog conversion

Optical to analog conversion can be achieved with an amplified photodiode. To maintain MR safety, the photodiode must be located at least 5m from isocenter. It is anticipated that the optical signal will be relatively weak; therefore, up to 70dB gain may be necessary.

2. Analog to digital conversion

Rapid analog to digital conversion is necessary to facilitate real-time signal analysis. It is preferable to perform this step in the MR environment with resulting digital signal transmitted to the control room.

3. Signal Analysis & Display

A dedicated PC is required in the control room to run custom built software for signal display, analysis and feedback

Finally, the software requirements are:

1. Data Collection & Display

The raw data received must be collected and displayed in a real-time so that user can see the optical signal as a function of time. A rate of 1Hz should be sufficient for the proposed application. The software should be capable of simultaneously

managing two optical and four thermal signals. In addition, during subsequent analysis it will be necessary to temporally register the MRI data with the optical data. As data is collected on different computing platforms, the individual timestamps will not be sufficient.

## 2. Data analysis & Feedback

Rapid data processing must be undertaken to facilitate application of a feedback algorithm in real-time. Consequently, the software requires dedicated thread for data collection and analysis. The output from the feedback algorithm must be displayed on screen with an alert to notify the user to deactivate the laser when the complete coagulation has occurred within the target volume

## 3. Data storage

The optical signal, feedback algorithm and respective timestamps must be saved to disk upon completion of each experiment.

### **6.2.2. System Architecture & Optical Probe Design**

As depicted in Figure 40A, the key components of the optical monitoring system are: 1) custom designed interstitial optical probe, 2) photodiode, 3) voltage divider, 4) microcontroller, 5) Computer and 6) custom built software. Light collected by the interstitial probe is transmitted along a 5m optical fiber to the photodiode, Si switchable gain detector (Thorlabs, NJ), using an SMA905 connector. The photodiode outputs an analog signal in the range 0-10V. Analog to digital conversion is performed by a microcontroller, Arduino Leonardo (Arduino LLC, Italy), at 1Hz. The microcontroller operates with a maximum voltage of 5V; therefore, a voltage divider is used to reduce the analog output range from the photodiode to 0-5V. Data from the microcontroller is

transferred in real-time via USB to computer in the control room. The computer runs the in house developed 'FLA Monitor' software (Python) which enables real-time data collection, visualization and analysis. This software package is discussed in more detail in the next section.

A total of four interstitial optical probes were designed, manufactured and evaluated. The primary difference between probes lies in the range of angles over which they collect light.

### **Design 1: Ballistic**

This probe is designed to predominantly detect ballistic and snake photons, that is photons that undergo no scattering or minimal scattering while travelling from the laser towards the probe. To achieve this the probe collects light from a single point at the distal end with a limited cone of acceptance as depicted in Figure 1B. During use, the probe is rotated such that the cone of acceptance points directly towards the laser fiber. The probe consists of a 5m long, 200 $\mu$ m core optical fiber with the tip encased in a 20mm section of polycarbonate tubing (Pioneer Optics, CT). The tip of the polycarbonate is sharp to facilitate insertion and coated with black epoxy (3M, DP-420, McMaster-Carr #7467A51) to block incoming light. The polycarbonate is press-fit into a carbon fiber tube and the fiber is secured proximally with a Tuohy Borst adapter. The tip of the optical fiber is polished to 43° to facilitate collection of light through the side of the polycarbonate casing as illustrated by the 'cone of acceptance' in Figure 1B.

Hypothesis: The probe is expected to primarily detect ballistic and snake photons; therefore, photovoltage will drop as the coagulation boundary grows and reach steady state once the coagulation boundary reaches the probe.

### **Design 2: Backscatter**

This probe is identical to the previous probe; however, during testing the probe is rotated such that the cone of acceptance points directly away from the laser source. Consequently, the probe should primarily detect photons travelling back towards the laser source after undergoing multiple scattering events.

Hypothesis: The probe is expected to primarily detect photons that travel past the probe undergo multiple scattering events and are ultimately backscattered towards the probe; therefore, the photovoltage should decrease as the coagulation boundary grows and then increase once the coagulation boundary passes the probe.

### **Design 3: Spherical**

Figure 44C illustrates an alternative design, designated 'Spherical', which facilitates light collection from all angles. This is achieved by scattering the light off titanium dioxide powder embedded in the polycarbonate tubing directly in front of the optical fiber. In contrast to the previous designs the optical fiber has a core diameter of 400  $\mu\text{m}$ . The fiber and polycarbonate casing are embedded in a carbon fiber tube as outlined in Design 1.

Hypothesis: This probe detects photons travelling in all directions; therefore, photovoltage will decrease as the coagulation zone increases.

### **Design 4: Radial**

The final probe shown in Figure 40D is designated 'Radial' as it accepts light from all directions in a single plane. The fiber has a core diameter of 400  $\mu\text{m}$  and the tip is tapered to a point which facilitates photon acceptance from all radial angles.

Hypothesis: This probe detects ballistic/snake photons and backscattered photons; therefore, the optical signal will decrease as the coagulation zone increases and increase once the coagulation zone passes the probe.

The following summarizes how each of the design requirements were satisfied:

1. Light Collection - Collect light at tip of probe and transmit to photodiode
  - Achieved using angled fiber tip (Ballistic, Backscatter and Radial) or titanium dioxide powder (Spherical) and 5m long optical fiber
2. MR Safe - no ferromagnetic material within 5m of iso-center
  - Probe shaft made from carbon fiber (non-ferromagnetic)
  - Probe tip made from polycarbonate (non-ferromagnetic)
  - Optical fiber made from silica (non-ferromagnetic)
  - 5m long optical fiber ensures photodiodes can be placed sufficiently far from iso-center
3. Probe diameter - <2.413mm
  - The carbon fiber tube has a diameter of 3.2mm but the distal section is turned down to 2.4mm to ensure that the section within the tissue mimicking phantom is less than 2.413mm.
4. Mechanical Properties - Rigid
  - Probe shaft made from carbon fiber which has comparable mechanical properties to metal (aluminum 6061)
5. Thermal properties - melting point > 86°C
  - Carbon fiber mechanical properties rated at 82°C by the manufacturer but no adverse effects were observed when placed in boiling water

- Polycarbonate melting point = 147°C
- Silica (optical fiber) melting point >400°C.
- Titanium dioxide melting point = 1855°C

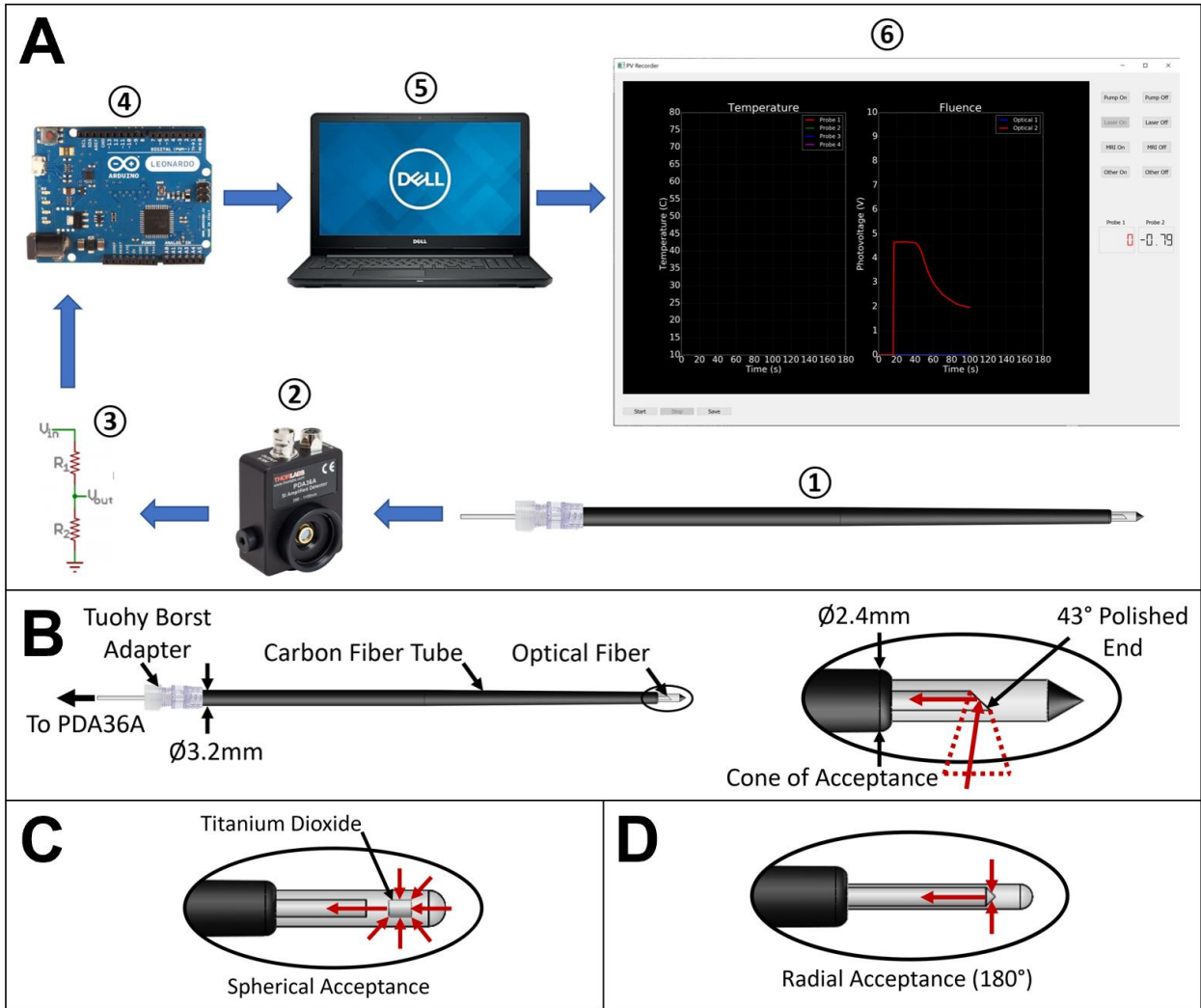


Figure 40: A - Components of the optical monitoring system: 1) Interstitial optical probe, 2) Photodiode, 3) Voltage divider, 4) Microcontroller, 5) Computer and 6) Custom built software. B – Detailed view of interstitial optical probe with a defined cone of acceptance. C – Detailed view of tip of interstitial probe with spherical acceptance. D - Detailed view of tip of interstitial probe with radial acceptance.



### 6.2.3. FLA Monitoring Software

The FLA monitoring software consists of the graphical user interface (GUI) shown in Figure 41. It was designed to simultaneously record, display and analyze data from up to four Fluoroptic® thermal probes (Lumasense, Santa Clara, California) and two custom designed optical probes. The graphs 'A' and 'B' display real-time data for the thermal and optical probes respectively (In this chapter, the thermal probes will not be used). The buttons highlighted by the blue circle allow the user to start/stop data collection and save results as a .csv file. Buttons in the red circle allow the user to record the timing of events including pump on/off, laser on/off and MRI on/off. The latter of which is crucial to enable temporal registration between the optical data and the imaging data from the MRI scanner. Finally, in the yellow circle, the output from the feedback algorithm is displayed in real-time.

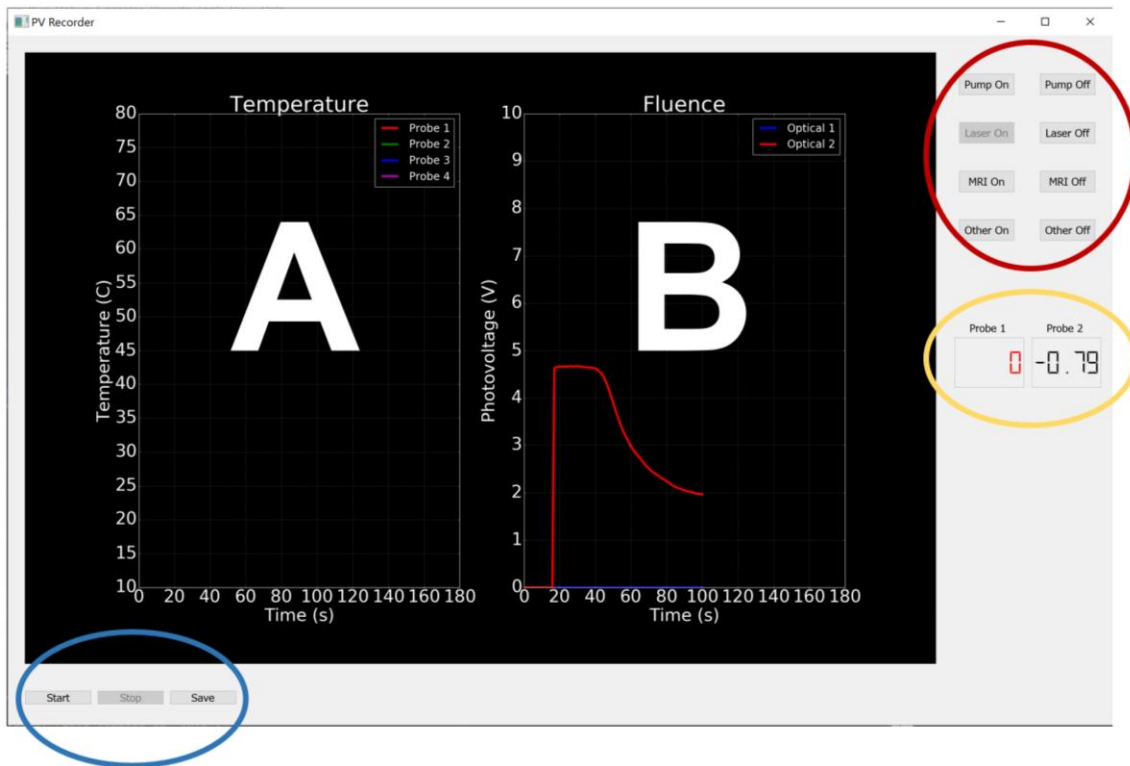


Figure 41: Custom built FLA monitoring software

The feedback algorithm is based on the hypothesis that the fluence at a fixed point within the ablation zone will drop during coagulation and either reach a steady state or an inflection point once the coagulation boundary has propagated up to that point. The photovoltage is proportional to fluence; therefore, we hypothesize that steady state indicates that all material has coagulated between the probe and the laser fiber. The feedback algorithm is designed to notify the user when the photovoltage has reached a steady state. As shown Figure 42, the algorithm analyzes data in a 10 second window. A 2<sup>nd</sup> order polynomial is fit to this data and the instantaneous rate of change at the last datapoint is quantified and displayed in the GUI (yellow circle). This feedback begins 15 seconds after the 'Laser On' button is activated to account for the initial steady state photovoltage which can be seen in Figure 42. This occurs because it takes time for the tissue temperature to reach a sufficient magnitude to induce coagulative necrosis. Once steady state has been achieved (slope = 0), the color of the text changes from black to red to notify the user that the ablation has been successful. Clinically, the laser should be deactivated once the steady state notification has been displayed.

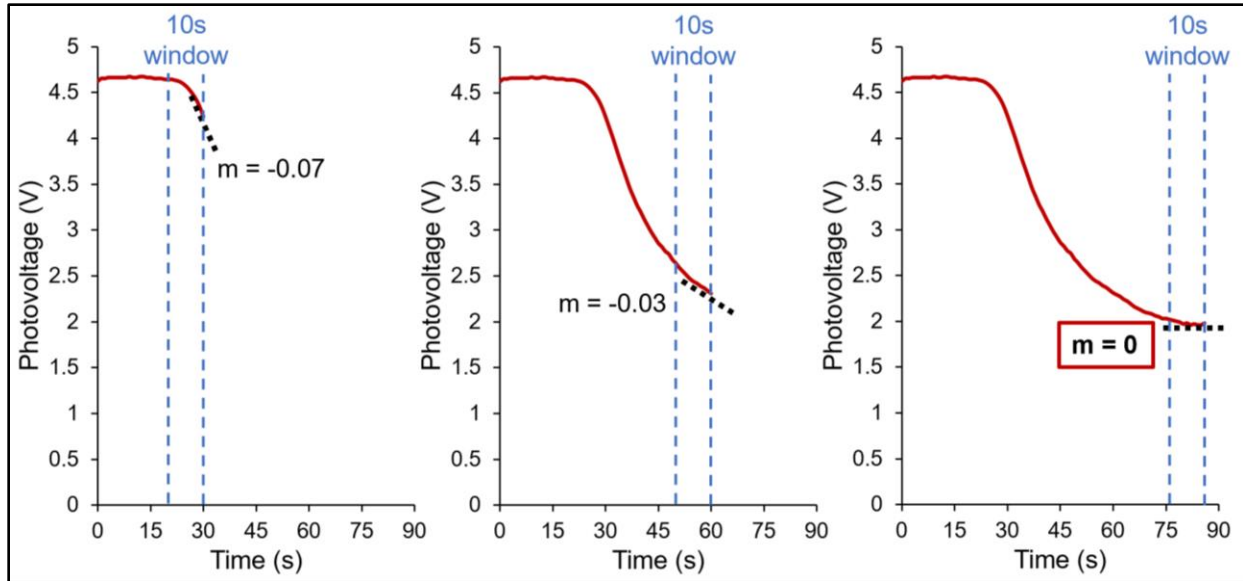


Figure 42: Feedback algorithm – A 2nd order polynomial is fit to the most recent 10s of data and the instantaneous rate of change ( $m$ ) at the most recent data point is quantified. We hypothesize that a steady state ( $m=0$ ) indicates complete coagulation of all tissue between the probe and the laser fiber.

### 6.3. System evaluation: Tissue Mimicking Phantom

#### 6.3.1. Methods

Each of the four interstitial optical probes was tested in a tissue mimicking phantom under the same conditions as in a previous clinical trial (Figure 43). Chapter 3 provides further detail on the clinical trial. Briefly, in the clinical setting a needle guide was used to insert the dual lumen catheter and a thermal probe in parallel into the prostate. We have simulated this setup using the tissue mimicking phantom developed in chapter 5. The phantom is preheated in a water bath to 37°C and then placed into a 3D printed testing rig consisting of an insulated box with channels for laser fiber and probe insertion. These channels are used to secure the probes at known distances from the laser fiber. The setup is similar to that described in detail in chapter 5 with the exception

that the insulated box contains multiple probe channels and is designed to accommodate two tests per phantom.

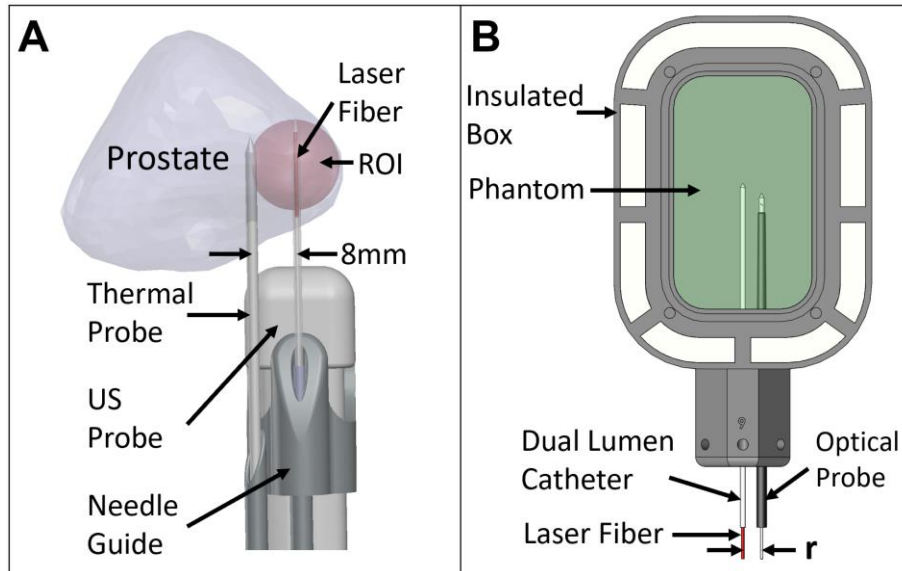


Figure 43: A) Clinical setup during FLA. B) Experimental setup designed to match clinical conditions with an optical probe used instead a thermal probe

For each test, FLA was performed at 13.75W for 3 min as in the clinical trial. The interstitial optical probes were tested at radial distances ( $r$ ) of 4mm, 5mm, 6mm and 7mm and simultaneously monitored with 3T MRI (Prisma, Siemens). The imaging plane was aligned along the trajectory of the laser fiber and the optical probe with both objects in the field of view. This was achieved using water fiducials that are visible in images acquired by the MRI localizer. The fiducials were created by designing the testing rig to contain 1mmx1mm channels as shown in Figure 44. The channels circumscribe the testing rig and are filled by injecting water through the screw holes used to seal the lid. The cross-section of the fiducials can be seen on the transverse image acquired by the MRI localizer. The coronal plane is then positioned such that it intersects both fiducials, the laser fiber and the optical probe. A  $T_2$ -weighted turbo spin echo sequence was then

acquired to confirm correct alignment (PRE). Once confirmed, an altered version of this sequence (CINE) was used to monitor the growth of the coagulation zone in near real-time. To ensure rapid image acquisition a trade-off was made between the signal to noise ratio (SNR) and the scan time. After laser deactivation another high-quality scan is acquired (POST) using the same imaging parameters as the PRE scan. The POST scan was later used to calibrate the automatic edge detection algorithm as described in the results section. Table 12 outlines the key parameters of each sequence. The scan duration of the CINE sequence is considerably shorter than the POST sequence due to a shorter echo time (TE), a shorter repetition time (TR) and a larger pixel size. In an effort to increase the SNR, the slice thickness was also increased relative to the PRE sequence. Figure 44 also shows the thumb screws that are used to seal the lid and secure the probes after insertion. This method cannot be used for the laser fiber as it is inserted through a dual lumen catheter which flows water around the fiber during laser activation. Using locking screws would impede water flow; therefore, the laser fiber is simply fixed in place by taping it to the already secured optical probe.

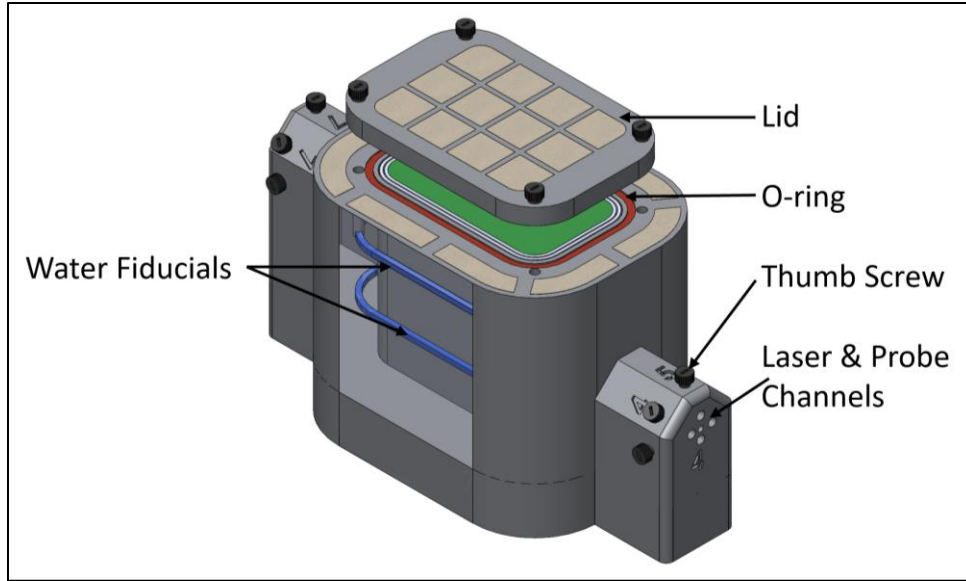


Figure 44: Detailed view of the testing rig with one wall rendered transparent to highlight the location of the water fiducials. Note that there are 2 fiducials as each phantom is used for two tests; one in the top section and one in the bottom section. An O-ring and thumb screws are used to seal the lid in place to minimize heat loss to the surroundings. Thumb screws are also used to secure the optical probes in place.

Table 12: MRI Sequence Parameters

Scan	TE (ms)	TR (ms)	Echo Train Length	Scan Duration (s)	Pixel (mm)	Slice Thickness (mm)
<b>CINE</b>	16	390	13	2	0.75*0.75	2
<b>PRE/POST</b>	52	2000	13	47	0.5*0.5	1

The final setup is shown in Figure 45 which depicts the setup in the MRI suite. The testing rig was placed on the scanner bed and advanced to isocenter after inserting the optical probes, dual lumen catheter and laser fiber. The optical fibers are 5m long and connect directly to photodiodes which are located as far from the scanner as possible but still within the magnet room. Data from the photodiodes is recorded by the microcontroller and transmitted via USB through a waveguide to the dedicated PC located in the control room. The laser and pump are also located in the control room and waveguides are used to connect the respective optical fiber and cooling line to the

dual lumen catheter. Finally, in order to temporally register the optical probe data and the imaging data, key events (MRI on/off, Pump on/off and laser on/off) were time stamped using the FLA monitoring software interface while the corresponding time reported by the MRI scanner was manually recorded.

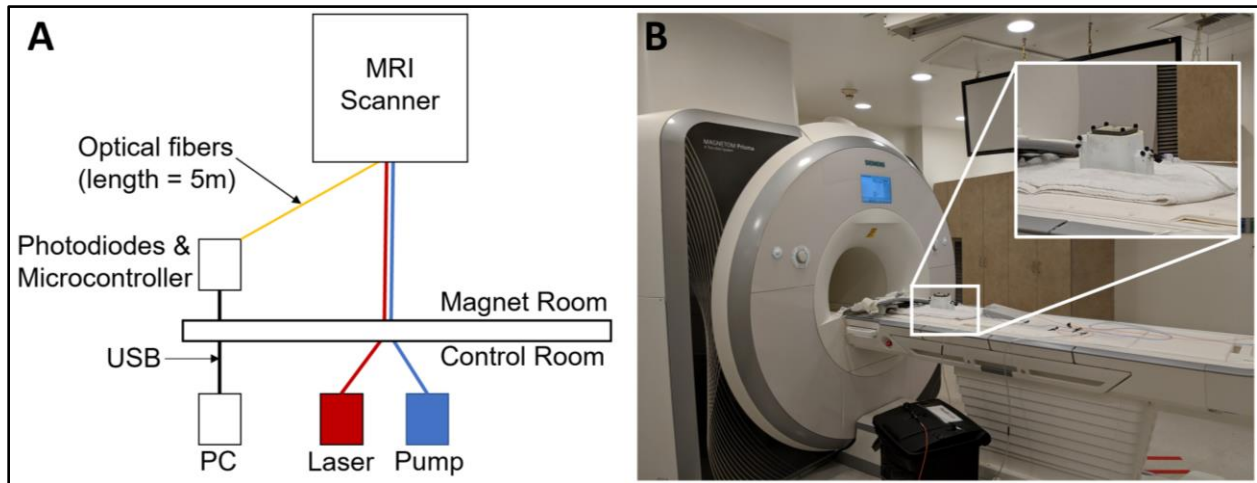


Figure 45: A) Block diagram of experimental setup using MRI to monitor laser ablation in the tissue mimicking phantom. B) Photograph of testing rig (inset) on the scanner table prior to placement at isocenter.

### 6.3.2. Results

Accurate imaging plane alignment is crucial for determining the coagulation radius and was achieved using water fiducials as illustrated in Figure 46. Figure 46A shows an example of the transverse image acquired by the MRI localizer. The cross-section of the fiducials is clearly visible; therefore, the coronal plane can be correctly aligned as indicated by the dashed red line. Alignment is confirmed using the PRE scan as shown in Figure 46B. The fiducials, dual lumen catheter and optical probe are clearly visible; thus, confirming correct alignment. To reduce the number of scans required, two optical probes were inserted for each test. While both probes are parallel to the dual lumen catheter, one probe is placed out of plane. This is necessary as the probe in-plane

interferes with the calculation of the ablation radius. Consequently, the ablation radius is determined from the opposite side only and the ablation zone is assumed to be cylindrically symmetrical.

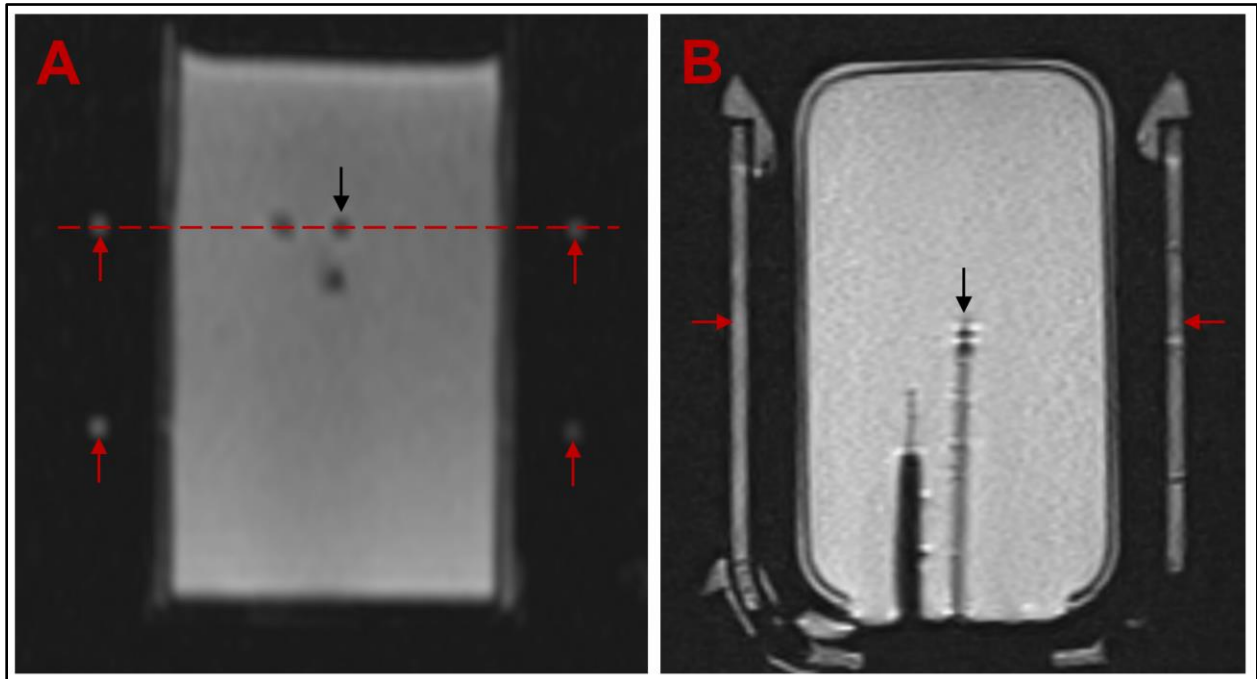


Figure 46: A) Transverse image acquired by the MRI localizer. The cross-sections of the fiducials are clearly visible (red arrows). Note that there are two sets of fiducials as each phantom is used for two tests. In this case the test is being performed in the top section of the phantom where the dual lumen catheter (black arrow) and optical probes are visible. B) PRE scan used to confirm alignment. The fiducials (red arrows), dual lumen catheter (black arrow) and one optical probe can be seen. The second optical probe is not in the imaging plane.

An example of the normalized photovoltage (each datapoint divided by initial photovoltage) recorded by the optical monitoring system is shown in Figure 47 along with corresponding MR images. The selected images illustrate the growth of the ablation zone over time and indicate that there is a correlation between the photovoltage and the coagulation radius. The first image was taken at the instant of laser activation. Both the dual lumen catheter and optical probe are visible and the ablation zone has yet to form.



In the second image the ablation zone has formed and is expanding towards the optical probe while the temporally registered photovoltage has begun to decrease. The edge of the ablation has been outlined using the edge detection algorithm which will be discussed in the next section. The next image shows that the ablation zone has reached the optical probe while the photovoltage has reached a steady state. In the final image, the ablation boundary extends beyond the optical probe and was taken just before laser deactivation.

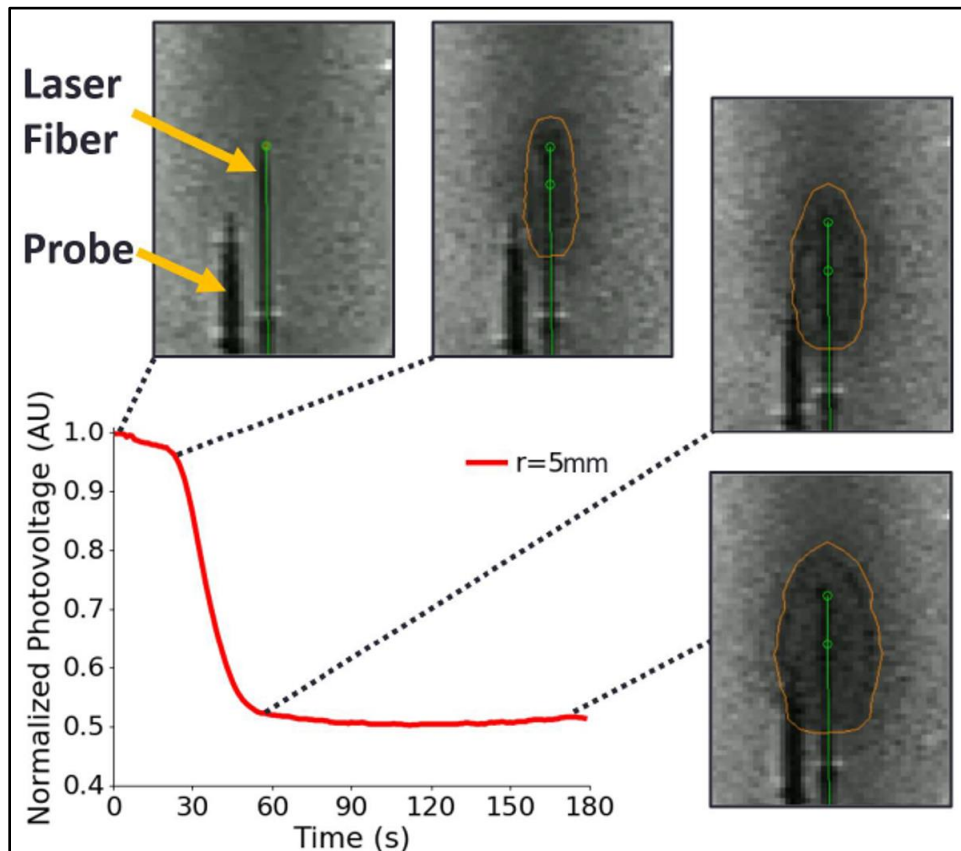


Figure 47: Photovoltage recorded using 'Ballistic' optical probe placed at 5mm for the laser fiber and corresponding MR images. The orange line in the MR images is the coagulation boundary derived using the edge detection algorithm. The green line denotes the location of the laser fiber.

To further illustrate the correlation between the photovoltage and the coagulation radius, it is necessary to quantify the coagulation radius as a function of time and

temporally register the datasets. To do so, an edge detection algorithm was developed using MATLAB and Python to derive an equation describing coagulation radius as a function of time. The algorithm follows this protocol:

Step 1: Create image dataset containing images acquired during laser activation only

- Import all images from an experiment into MATLAB
- The laser activation time reported by the scanner was manually recorded during the test
- Each laser activation lasted for 180s
- Given this information and the timestamps stored in the DICOM metadata, it is trivial to reduce the dataset to include only images acquired during laser activation

Step 2: Identify laser fiber and optical probe co-ordinates

- Using a custom GUI, the user manually selects the co-ordinates of the tip and base of both the laser fiber and optical probe from the first image in the dataset. Note, the laser fiber is housed inside the dual lumen catheter and is always located in the center of the phantom.
- Analysis of these co-ordinates indicates the location of the optical probe (left or right) and subsequent analysis is undertaken on the opposite side only. This is necessary as both the probe and the coagulation zone appear as areas of low signal; therefore, it is difficult to differentiate between them.

Step 3: Define coagulation-native threshold

- Coagulated pixels appear dark (low signal) and native pixels appear bright (high signal)

- A sample of definitely coagulated pixels is taken from the final image in the dataset (Figure 48).
- A series of thresholds are defined:  

$$\text{threshold} = \text{mean of coagulation sample} + (X \cdot \text{standard deviation of coagulation sample})$$
where X is 0.5-3 in steps of 0.25
- All pixels with a value less than the threshold are defined as coagulated

#### Step 4: Delineate the coagulation boundary

- A circular pattern of vectors is defined around the center of the ablation.
- For each vector on the side without the probe, the boundary is determined using each threshold defined in step 3
- This process is repeated for every image in the dataset
- Let's define the resulting datapoints as 'boundaryData'.

#### Step 5: Coagulation Radii

- The coagulation radius is defined as the maximum value in 'boundaryData'
- At this stage, each image has multiple estimates of the radius as the radius is determined for every threshold value defined in Step 3
- For convenience, let's define this data as 'radiiData'

#### Step 6: Subsample 'radiiData' at 1Hz

- Photovoltage was recorded at 1Hz while the MRI scanner acquired images at approximately 0.5Hz. To temporally register the two datasets the relationship between the coagulation radius and time must be determined
- The dataset 'radiiData' was imported into Python

- A 3-sample moving average filter was applied to 'radiiData' to reduce the effect of noise introduced due to the poor image quality of the CINE sequence
- Coagulation radius as a function of time was then derived using a logarithmic fit as shown in Figure 48. Note that the derived equation ignores radii less than 1mm to account for pixels occupied by the dual lumen catheter.
- Using the derived equation, it is trivial to subsample 'radiiData' at 1Hz
- For convenience, lets define the resulting dataset as 'radiiData1Hz'. Note that 'radiiData1Hz' contains estimates of the radius at each second during laser activation. There are multiple estimates at each second as the radius was estimated for each threshold defined in Step 3.

#### Step 7: Identify optimum coagulation threshold

- In this final step, the data (radius vs time at 1Hz) in 'radiiData1Hz' is filtered using the final radius (designated 'r' in Figure 48) determined from the higher resolution POST scan using Radiant DICOM Viewer
- The optimum coagulation threshold is then defined as the threshold that minimizes the error between the final radius and the radius at the last time point (180s) in 'radiiData1Hz'
- The final dataset, designated 'radiusVsTime', is then simply the data from 'radiiData1Hz' that was found using the optimum coagulation threshold. This data is temporally registered with the photovoltage dataset by filtering the latter for photovoltage > 0 i.e. laser active.

The edge detection algorithm was applied to data gathered in each experiment and in all experiments a logarithmic fit proved sufficient to describe coagulation radius

as a function of time ( $r^2 > 0.92$ ). In addition, the coagulation boundary shown in Figure 47 was found using the 'boundaryData' dataset where the threshold is equal to the optimum coagulation threshold found in Step 7. To create the plot the data is mirrored across the laser vector defined in Step 2.

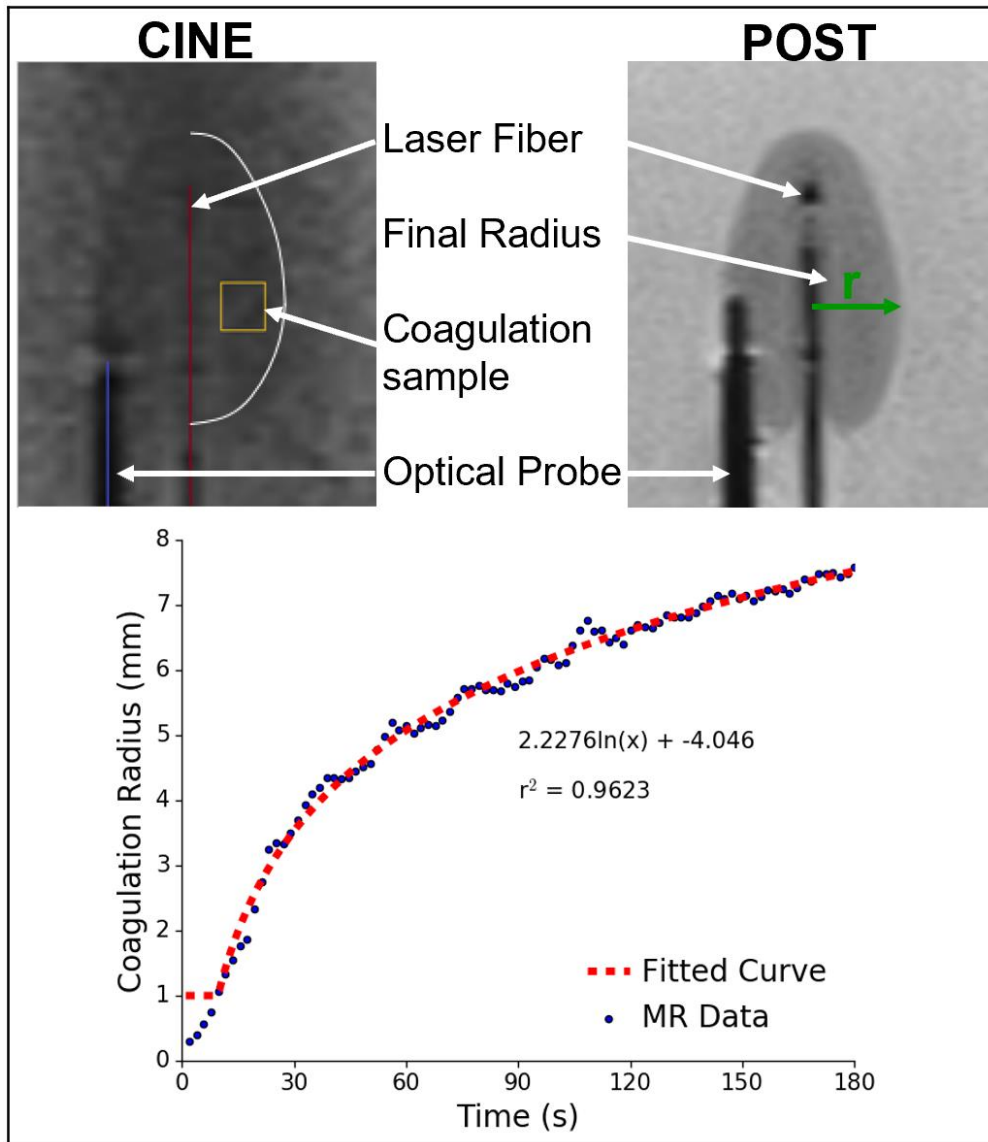


Figure 48: Coagulation radius as a function of time as determined by the edge detection algorithm using both the CINE and POST scan data.

For each experiment the edge detection algorithm was used to temporally register the photovoltage (from the FLA monitoring software) and the coagulation radius (from the MRI). To illustrate the relationship between photovoltage and the coagulation radius, the normalized photovoltage was plotted against the coagulation radius as shown in Figure 49 (left column). In addition, data from the feedback algorithm is shown Figure 49 (right column).

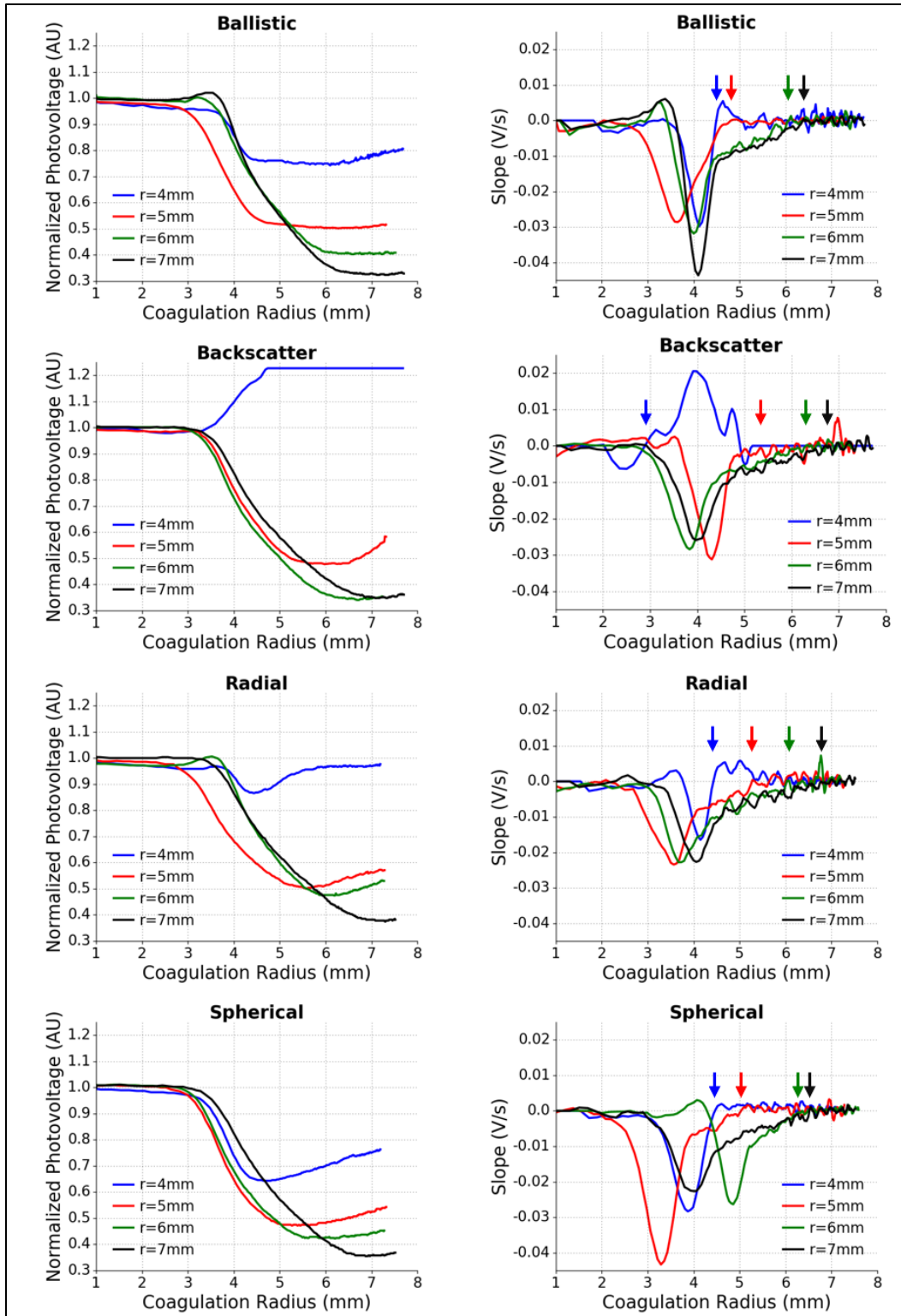


Figure 49: Normalized photovoltage and instantaneous rate of change (slope) as a function of coagulation radius for each interstitial optical probe. Arrows identify the signal plateau/inflection point for each probe

In this set of experiments, the feedback algorithm was ignored and laser activation continued for three minutes in all tests. Retrospective analysis was performed to determine the coagulation radius that would have been achieved if the algorithm was used to determine the laser deactivation time. To assess the accuracy of each probe, the feedback algorithm derived coagulation radius was compared to the true radius as defined by the MRI data (Figure 50). Finally, to quantify the accuracy of each probe the absolute error (mean  $\pm$  one standard deviation) was calculated as shown in Table 13.

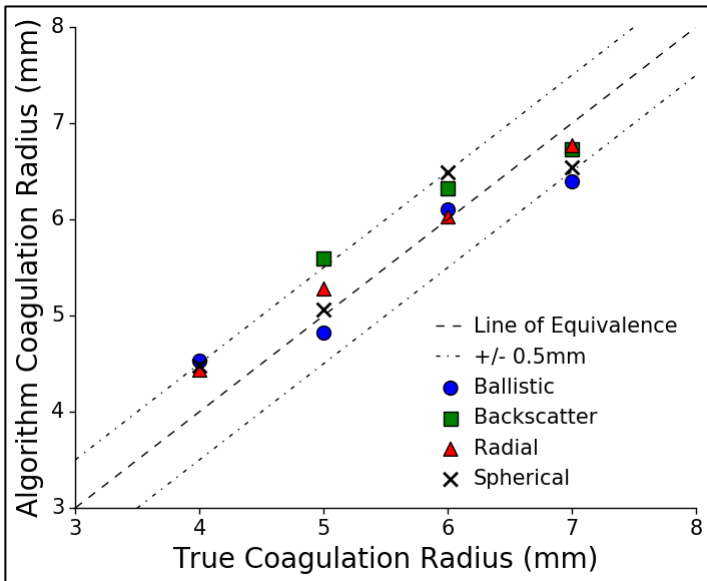


Table 13: Absolute error (mean  $\pm$  one standard deviation) for each optical probe

	Absolute Error (mm)
<b>Ballistic</b>	0.35 $\pm$ 0.21
<b>Backscatterer</b>	0.39 $\pm$ 0.14
<b>Radial</b>	0.25 $\pm$ 0.15
<b>Spherical</b>	0.37 $\pm$ 0.18

Figure 50: Comparison of the feedback algorithm coagulation radius and the true coagulation radius derived from the MRI data.

### 6.3.3. Discussion

The primary components of the optical monitoring system are the optical probe, photodiode, microcontroller and FLA monitoring software. Throughout testing, the system performed as designed and no unexpected problems were encountered. There was some concern that the photodiode and microcontroller would suffer from



interference or magnetic attraction as they were located in the magnet room. These concerns proved to be unwarranted as no issues were encountered. Additionally, the FLA monitoring software successfully displayed photovoltage in real-time and recorded the timing of key events (MRI on/off, pump on/off and laser on/off). All data were saved as .csv files with no data loss observed during subsequent data analysis.

MRI scanning was also successful with the fiducials in the testing rig proving sufficient to correctly align the imaging plane with the laser fiber and optical probe under evaluation. In addition, the thumb screws secured the optical probes and prevented unwanted movement during advancement of the scanning table into the bore. Likewise, no movement of the dual lumen catheter was observed as the proximal end was taped to the adjacent optical probe.

The PRE, CINE and POST MR scans were all able to identify the coagulation zone. As expected, the image quality of the CINE scan suffers because the sequence was designed to minimize scan duration which results in reduced SNR. Nevertheless, the growth of the coagulation zone over time was successfully quantified through the use of the edge detection algorithm. The relationship between coagulation radius and time was described using a logarithmic fit with  $r^2 > 0.92$  in all cases.

Four optical probe designs were tested in a tissue mimicking phantom using a custom designed testing rig to match conditions to those in a previous clinical trial. The key design requirements were identified as 1) interstitial light collection and delivery to photodiodes, 2) MR safe, 3) diameter  $< 2.413\text{mm}$ , 4) sufficiently rigid to prevent flexion during insertion, and 5) thermally stable during FLA. All probes successfully met these conditions. Throughout laser activation a voltage was recorded by the photodiodes; thus, confirming that the optical probes are capable of interstitial light collection and delivery

to the photodiodes. Moreover, the recorded signal is relatively noise free suggesting that the MR scanner magnetic field does not cause interference. The probes themselves contain no ferromagnetic material and thus no movement or imaging artifact was observed during testing. The absence of large imaging artifacts is critical to facilitate quantification of the coagulation radius using the edge detection algorithm. Finally, the diameter of the carbon fiber probe shaft was designed and manufactured at 2.4mm and no flexion or melting was observed during or after testing.

Each optical probe possesses unique light collection capabilities:

### **Design 1: Ballistic**

Hypothesis: The probe is expected to primarily detect ballistic and snake photons; therefore, photovoltage will drop as the coagulation boundary grows and reach steady state once the coagulation boundary reaches the probe.

The results in Figure 49 support this hypothesis with photovoltage observed to decrease as the coagulation radius expands towards the probe. During the initial growth of the coagulation radius (<3mm), a minimal change in photovoltage is observed. This is followed by a sharp decrease in photovoltage when the coagulation radius lies in the range 3-4mm. This characteristic was observed for all probe positions and demonstrates that the optical signal is dependent on optical interactions throughout a volume of material. In contrast an interstitial thermal probe only records the temperature of tissue under direct contact. A similar observation was made by Whelan et al who recorded the response of an interstitial thermal probe and an interstitial optical probe during FLA of porcine kidney *in vivo* [200]. In that experiment the thermal output

remains approximately constant while the photovoltage decreases. In contrast to our work, they were unable to derive the relationship between the coagulation radius and time. Consequently, the correlation between photovoltage and coagulation radius could not be assessed.

From Figure 49, it is also evident that the photovoltage reaches a steady state once the coagulation boundary propagates up to the optical probe. This characteristic represents a promising method of monitoring FLA. A pre-defined coagulation zone may be achieved by placing the laser fiber in the center and the optical probe at the desired margin with laser activation continuing until steady state photovoltage is observed.

## **Design 2: Backscatter**

Hypothesis: The probe is expected to primarily detect photons that travel past the probe undergo multiple scattering events and are ultimately backscattered towards the probe; therefore, the photovoltage should decrease as the coagulation boundary grows and then increase once the coagulation boundary passes the probe.

In contrast to the 'Ballistic' probe, the optical response with the 'Backscatter' probe appears to depend on its position. When placed 4mm from the laser fiber, no drop in photovoltage is observed. Instead, the photovoltage remains constant until the coagulation radius exceeds 3mm. The photovoltage then rises rapidly and eventually saturates the photodiode at approximately 5mm. This behaviour is indicative of the 'light trapping' effect that occurs due to a coagulation induced increase in the reduced scattering coefficient and a corresponding decrease in the optical penetration depth. Interestingly, this effect is reduced substantially when the probe is placed at 5mm and is completely absent when the probe is positioned at 6mm and 7mm. The data therefore

does not support our hypothesis at radii greater than 5mm. Moreover, in tissue with different optical properties, the 'light trapping' effect may extend beyond 5mm or possibly not even reach 4mm. For this reason it is difficult to design an algorithm to automatically detect the ablation boundary based on data from the 'Backscatter' probe.

### **Design 3: Spherical**

Hypothesis: This probe detects photons travelling in all directions; therefore, photovoltage will decrease as the coagulation zone increases and subsequently increase once the coagulation radius passes the optical probe.

Again, no drop in photovoltage is observed for a coagulation radius less than 3mm. For all probe positions a sharp drop in photovoltage is then observed followed by an inflection point once the coagulation boundary propagates as far the optical probe. This data supports the hypothesis and like the 'Ballistic' probe it provides a useful method of identifying the instant the coagulation radius reaches the optical probe.

### **Design 4: Radial**

Hypothesis: This probe detects ballistic/snake photons and backscattered photons; therefore, the optical signal will decrease as the coagulation zone increases and increase once the coagulation zone passes the probe. The response of the 'Radial' probe approximates that of the 'Spherical' probe and therefore supports our hypothesis.

In summary, all of the optical probes except for the 'Backscatter' probe behave as expected and can potentially be used to monitor FLA with a high level of accuracy as

indicated in Figure 50. For these three probes the mean absolute error ranged from 0.25mm to 0.39mm which suggests that no design is inherently superior.

The ideal optical probe should be able to detect light at multiple locations simultaneously. For example, when treating prostate cancer, it is critical that the rectal wall remains free from thermal damage. With a multielement optical probe, a single probe could be used to monitor both the rectal wall and the intended coagulation boundary. It may also be advantageous to combine thermal and optical probes into a single probe. In both cases, only the 'Ballistic' probe can be easily integrated as it only requires line of sight at a single point. In contrast, the addition of extra elements would block some of the light that would otherwise be collected by 'Spherical' and 'Radial' probes. Moreover, the 'Ballistic' probe can be fixed to the outside of a rigid opaque needle which greatly eases manufacturing.

For these reasons the 'Ballistic' probe was chosen for the optical monitoring system. Further testing in the tissue mimicking phantom will not provide useful data as the tissue mimicking phantom was designed with known optical properties and therefore the optical response should be consistent across experiments. Instead, in the next section, the optical monitoring system with the 'Ballistic' probe will be tested in *ex vivo* bovine muscle. The optical properties of *ex vivo* bovine muscle should be similar to *in vivo* soft tissue; however, in contrast to the phantom there is likely to be variability between samples. This ensures that the optical monitoring system can be tested in a less controlled environment than the phantom.

## 6.4. System Evaluation: Ex Vivo Bovine Muscle

### 6.4.1. Methods

A total of 20 ex vivo bovine muscle samples were prepared and placed in 3D printed sample holders as shown in Figure 51. The sample holders consist of two sections which split along the trajectory of the laser fiber. After the tissue sample is inserted into the bottom section a compression plate is placed on top of the sample and the top section of the sample holder is secured in place with four screws. A further pair of screws is then used to force the compression plate downwards and compress the sample within the holder. This is necessary to secure the sample in place and facilitate dual lumen catheter and probe insertion. Without the compressive force, the sample is excessively pliable making it difficult to accurately insert and remove the dual lumen catheter and optical probe.

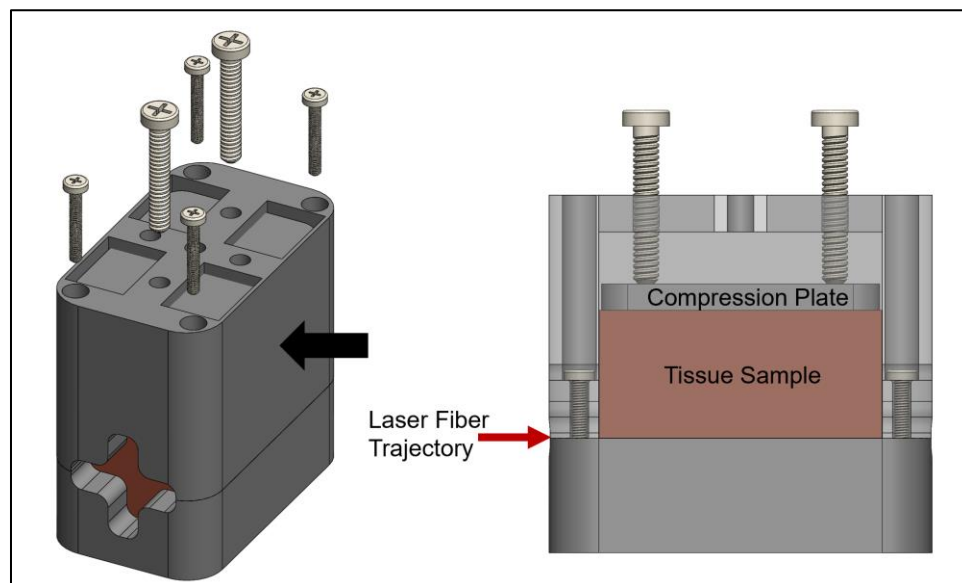


Figure 51: Ex vivo bovine tissue sample holder. The image on the right is orientated in the direction of the black arrow and the top section of the sample holder is rendered transparent

The fully assembled sample holder is shown in Figure 52A. The sample holders are then placed in sealed bags and submerged in a water bath to raise the temperature to 37°C. Each sample is then tested in an insulated testing rig similar to the MRI testing rig (Figure 52B). FLA is performed with the 'Ballistic' optical probe and is monitored via the FLA monitoring software. The feedback algorithm outlined in Figure 42 is used to notify the operator when the coagulation boundary has successfully propagated as far as the optical probe. The test was performed five times with the optical probe placed at 4mm, 5mm, 6mm and 7mm from the laser fiber. After each test, the sample was removed from the testing rig, placed in a sealed bag and stored in a freezer for at least 12 hours. The frozen samples were then removed from the freezer and the top section of the sample holder was detached. Figure 52C shows the sample in the bottom half of the holder with the compression plate still on top of the sample. The frozen sample is then sectioned along the surface of the sample holder using a deli slicer. This process ensures that the sample is sectioned accurately along the laser fiber trajectory. It is difficult to identify the ablation zone when the sample is frozen; therefore, the sample is allowed to thaw for approximately 45 minutes. The final sample is then ready to be photographed from directly above as indicated in Figure 52D.

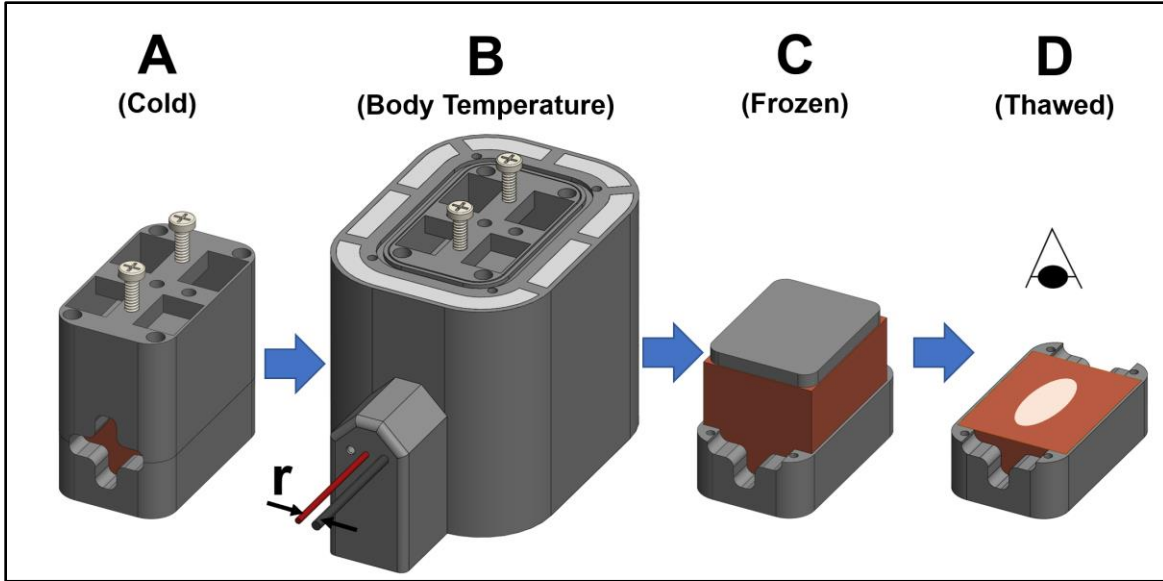


Figure 52: A) Cold tissue sample in tissue holder. B) Sample holder in testing rig after being preheated to 37°C. C) Sample holder with top section

To ensure consistent lighting across samples photographs were taken in a lightbox with a Canon EOS Rebel camera as shown in Figure 53.

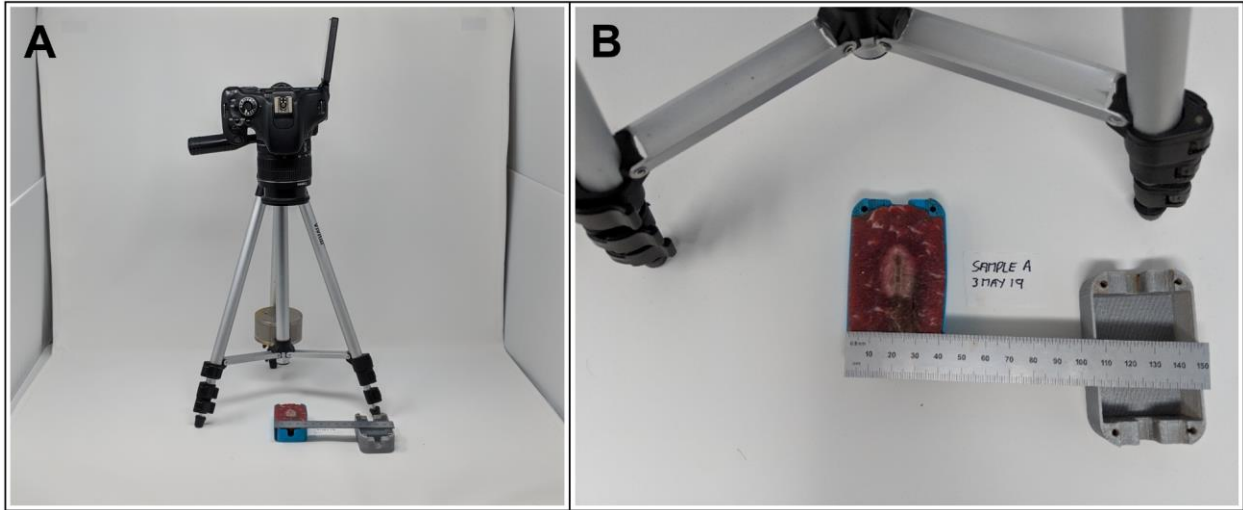


Figure 53: A) Setup for acquiring photograph of sample ablation zone. To ensure consistent lighting a professional lightbox was used. B) Sample image showing ruler which will be used to scale the acquired photograph. Photographs used for analysis were taken with greater magnification



## 6.4.2. Results

Each photograph was analyzed using a custom python script with the following steps:

Step 1: Prepare images for analysis

- Each image is imported into python and a custom GUI is used to select the co-ordinates of the laser fiber and the edges of the sample holder.
- Using these co-ordinates, each photograph is then rotated and cropped as shown in Figure 54 (middle row)

Step 2: Define coagulation thresholds

- Coagulated pixels appear bright (high signal) and native pixels appear dark (low signal)
- A sample of definitely coagulated pixels is taken from within the ablation zone.
- A series of thresholds is defined:

$\text{threshold} = \text{mean of coagulation sample} - (X * \text{standard deviation of coagulation sample})$

where X is 1-3 in steps of 0.25

Step 2: Define profile line

- Using a second GUI, the user specifies the co-ordinates of a profile line (see Figure 54).
- The profile is placed immediately above the optical probe and the user must select a location that is not obscured by fat. Both fat and coagulated tissue appear white; therefore, it is difficult to differentiate them.
- The profile line is eleven pixels thick. The average pixel intensity along the profile line is shown in the bottom row of Figure 54. This step is necessary to reduce the effect of artifact from glare and fat which both appear bright

### Step 3: Analyze profile line to determine coagulation radius

- By observation, the user specifies the window of pixels in which each edge lies.
- Linear regression is used to fit a line to the data within each window
- Using the equation of this line, the coagulation boundary is quantified for each threshold defined in Step 2
- This process is performed on both edges of the ablation zone and the radius is simply half the distance between the points
- If fat obscures one edge, the radius is calculated from the center of the laser fiber as shown in Figure 54 at 'r=5mm'. If fat obscures both edges, the image is removed from the dataset and the experiment is repeated.

### Step 4: Optimum threshold and estimated radius

- Multiple estimates of the coagulation radius exist at this point as the coagulation radius was quantified using the series of thresholds defined in Step 2.
- A leave-one-out approach is used to define the optimum threshold for each image:
  - A subset of data is created containing every image except the image under analysis
  - The optimum threshold is then chosen to minimize the error between the estimated radius and the expected radius (probe location)
  - This threshold is then used to define the estimated coagulation radius in the image under analysis

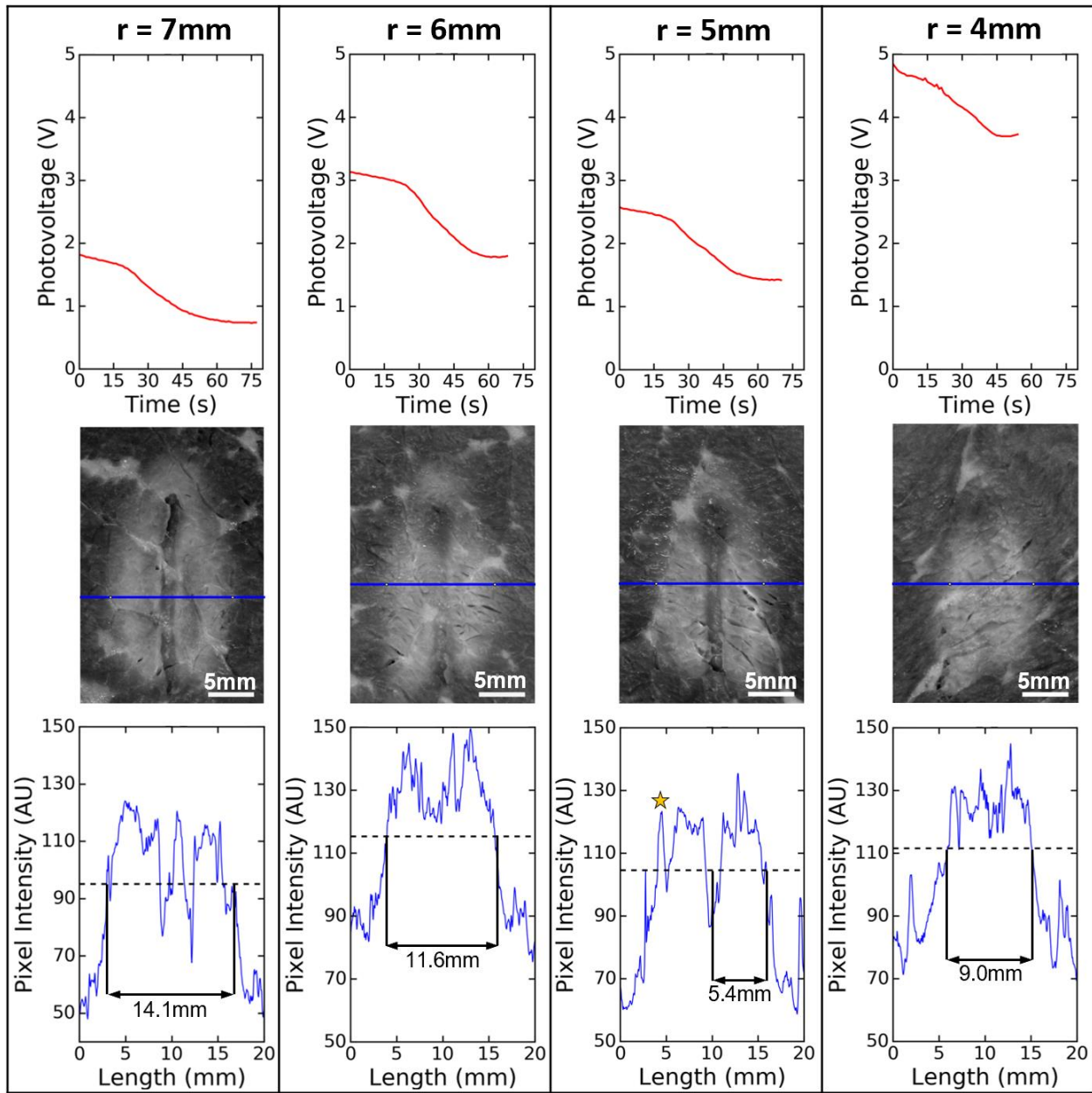


Figure 54: Photovoltage recorded during FLA experiments in ex vivo bovine muscle (Top row), photographs of the ablation zone after FLA (middle row) and profile lines used to determine the coagulation radius (bottom row). Note that 'r' indicates the distance between the probe and the laser fiber. For  $r=5$ , fat obscures the left edge and is seen as signal spike on the profile line (yellow star). In this case the radius is measured from the center of the dual lumen catheter.

Figure 54 shows examples of the photovoltage, coagulation zone and profile line recorded for each probe position. Each of these experiments was repeated five times for a total of twenty experiments. The utility of the feedback algorithm is demonstrated in Figure 55 which compares the measured damage radius (calculated as in Figure 54) against the target damage radius. The target damage radius is the position of the probe relative to the laser fiber as the proposed protocol for achieving a predefined radius is to place the optical probe at the desired margin. As expected, there is a strong linear relationship between the measured damage radius and the target damage radius ( $r^2 = 0.91$ ) and the absolute error (mean  $\pm$  SD) is  $0.3 \pm 0.1$  mm.

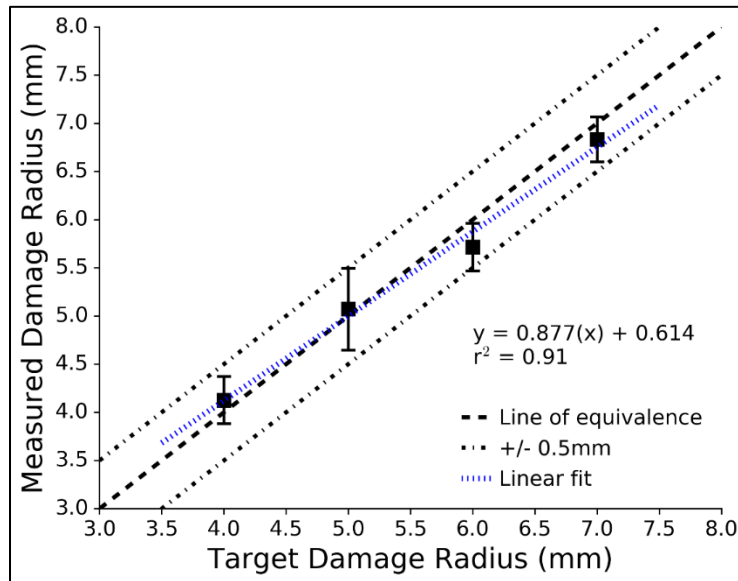


Figure 55: Comparison of the measured damage radius (from analysis of the ablation zone) against the target damage radius (position of the probe relative to the laser fiber). Error bars signify one standard deviation. Mean absolute error =  $0.3 \pm 0.1$

Finally, we compare the laser exposure duration for each coagulation radius in ex vivo bovine muscle, the tissue mimicking phantom and in vivo human prostate. For bovine muscle, it was necessary to assume that the measured damage radius was equal to the target damage radius. The phantom calculation was based on the 'radiusVsTime'

dataset outlined in the edge detection algorithm section and Figure 48. The laser exposure duration is interpolated from three minute laser activations. Consequently, it does not account for growth of the coagulation zone after the laser is deactivated; however, this error is expected to be minimal due to rapid cooling. The prostate data is taken from the clinical trial (see chapter 3) in which ten men received FLA followed by an MRI to assess the extent of coagulation based non-perfused tissue. While ten patients were treated, nine of them received overlapping ablation zones, rendering it impossible to correlate the coagulation zones with the laser exposure duration. For coagulation radii less than 6mm, the laser exposure duration is similar for bovine muscle and tissue mimicking phantom; however, there is a statistically significant difference ( $p < 0.01$ ) between the two at radii of 6mm and 7mm. In contrast, the laser exposure duration necessary to achieve a coagulation radius of 7.5mm is similar for the tissue mimicking phantom and in vivo human prostate.

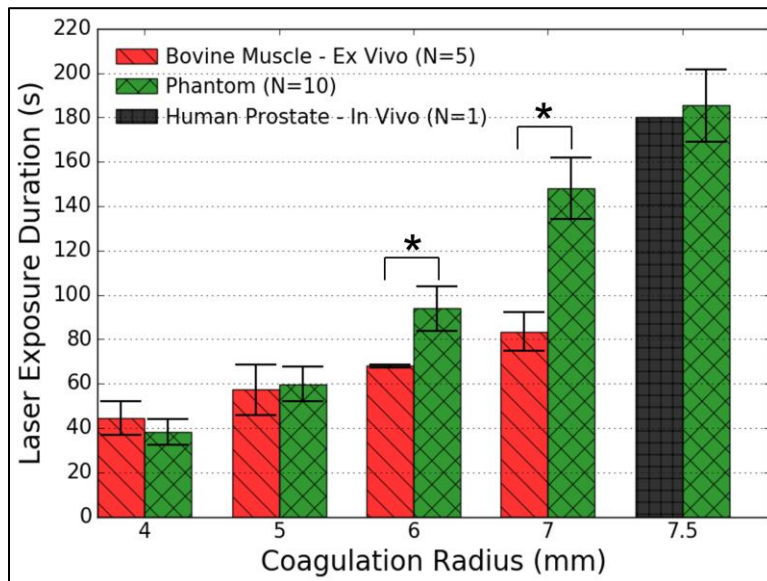


Figure 56: Laser (980nm) exposure duration at 13.75W required to achieve predefined coagulation radii in ex vivo bovine muscle, tissue mimicking phantom and in vivo human prostate. \* $P < 0.01$  (Wilcoxon rank-sum)

### 6.4.3. Discussion

FLA achieves oncologic control by inducing hyperthermia throughout the target volume. Consequently, many groups have attempted to use thermal monitoring methods as a feedback modality. MRT [6] and interstitial thermal probes [29], [73], [98], [99], [205] have been widely investigated for this purpose. To estimate the induced cell death, the thermal data is generally used in combination with an Arrhenius thermal damage model [11], [228], [229]. In addition to thermal data, these models require tissue specific kinetic parameters. In chapter 3 we demonstrated that published values for these parameters result in significantly different estimates of the optimal exposure during FLA. In this chapter we have explored the effect of thermal coagulation on laser-tissue interactions in an effort to develop an alternative method of monitoring FLA that does not rely on thermal damage models.

In the previous sections we described an optical monitoring system and tested various interstitial optical probes in a tissue mimicking phantom. Ultimately, an interstitial radiance probe designed to preferentially collect ballistic and snake photons was identified as the optimal interstitial optical probe for the proposed application. In this section we sought to characterize the performance of the optical monitoring system in a less controlled environment than that provided by the tissue mimicking phantom. Ex vivo bovine muscle was chosen as a testing model as it is readily available and unlike the tissue mimicking phantom the optical properties are unknown and likely to vary between samples. Ex vivo bovine muscle has been used in similar studies analyzing the effect of thermally induced coagulation on tissue properties [188], [206], [231].

In contrast to the tissue mimicking phantom, the growth of the coagulation zone cannot be tracked in ex vivo bovine muscle via MRI. Instead we have performed FLA

using the FLA monitoring software to identify the correct time to deactivate the laser. Tests were performed with the interstitial optical probes placed at 4mm, 5mm, 6mm and 7mm from the laser fiber. The feedback algorithm in the FLA monitoring software indicates when the coagulation boundary has propagated up to the probe. Accurate assessment of the coagulation radius was successfully achieved using a 3D printed sample holder (Figure 52) and a deli slicer to section the sample along the laser fiber trajectory (Figure 54). The sample was then photographed and the coagulation radius was found using a custom-built image analysis algorithm developed in python.

The accuracy of the interstitial optical monitoring system was assessed by comparing the measured coagulation radius against the target coagulation radius. The absolute error (mean  $\pm$  SD) was found to be  $0.3\pm 0.1$ mm. While this result provides strong evidence in support of the optical monitoring system, a key limitation of the experimental approach must be considered. Specifically, the image analysis algorithm used to determine the coagulation radius defines the coagulation threshold such that it minimizes the overall error. This threshold is determined from a dataset that does not include the image under analysis; however, it is still likely that the true absolute error is greater than reported here. For example, if the optical monitoring tends to underestimate the extent of ablation, the resulting bias is removed by the image analysis algorithm. However, the advantage of the algorithm over direct measurement is that measurement errors tend to be systematic i.e. if the algorithm underestimates the ablation radius in one image by 1mm, then it underestimates the radius in all images by approximately 1mm. For this reason, we have also shown that there is a strong linear relationship between the measured damage radius and the target damage radius ( $r^2 = 0.91$ ). The coefficient of determination is largely independent of the bias removed by

the image analysis algorithm. Again, if the algorithm underestimates the coagulation radius, all measurements are equally effected; therefore, the relationship between the measured and true coagulation radius will change but the coefficient of determination will not.

The goal of testing in ex vivo bovine muscle as well as the tissue mimicking phantom was to demonstrate that the utility of interstitial optical monitoring in media with various optical and thermal properties. The tissue mimicking phantom was designed to possess dynamic optical properties similar to human prostate. As a result, the laser exposure time required to achieve a coagulation radius of 7.5mm was found to be similar in the phantom and in vivo human prostate (Figure 56). In contrast ex vivo bovine muscle only exhibits a similar laser exposure time at radii of 4mm and 5mm with a significant difference ( $p < 0.01$ ) observed for radii of 6mm and 7mm. These results suggest that the optical and/or thermal properties of ex vivo bovine muscle are not closely matched to the tissue mimicking phantom and are therefore also not similar to in vivo human prostate. In spite of this, the optical monitoring system performed adequately in both models as both exhibit the characteristic coagulation induced increase in scatter. This increase in scatter is present for all soft tissues therefore, the optical monitoring system is likely to find utility in various soft tissues such as brain, liver and kidney.

## **6.5. Conclusion**

An interstitial optical monitoring system was successfully designed, constructed and evaluated. While, three optical probe designs ('Ballistic', 'Spherical' and 'Radial') were found to be suitable for monitoring focal laser ablation, the 'Ballistic' probe was



identified as the optimal design as it can easily be expanded to a multi-element probe. A feedback algorithm, based on the instantaneous rate of change of measured photovoltage as a function of time, is capable of identifying the coagulation boundary. The utility of the optical monitoring system was successfully demonstrated in ex vivo bovine muscle with a mean absolute error of  $0.3\pm 0.1\text{mm}$  observed in coagulation volumes in the range 4-7mm. It is anticipated that the optical monitoring system will provide accurate feedback in a variety of soft tissue such as brain, liver and kidney.

# CHAPTER 7

## Conclusions and Future Directions

### 7.1. Summary

Radical prostatectomy and radiation therapy represent the current state of the art in interventional treatment for prostate cancer. Both modalities are associated with numerous side-effects including erectile dysfunction and urinary incontinence. The advent of improved diagnostic techniques has facilitated localization of the tumor within the gland. This has led to a growing interest in developing minimally invasive technologies that treat the target tumor while sparing surrounding healthy tissue and thus limiting undesirable side-effects. FLA represents a promising modality; however, it is currently preformed using MRI to both guide the laser to the target tumor and monitor treatment progress. The resource intensive nature of this approach presents a barrier to widespread adoption. Consequently, our research efforts have focused on developing technology to translate FLA from the MRI suite to the urology clinic.

To perform FLA in the absence of MRI, alternative methods must be developed for both guiding the laser fiber to the target and monitoring treatment progress in real-time. At our institution, there is considerable experience with MR-US fusion guided biopsies. In this procedure, ROIs are generated from existing MRI data and co-registered with real-time ultrasound imaging. This facilitates targeted biopsies in which tissue samples are drawn from suspicious areas identified via MRI. These procedures are routinely performed in under 30 minutes. Given that a biopsy needle can be guided to a

predefined location with MR-US fusion guidance, there should be minimal difficulty swapping the biopsy needle for a laser fiber. The greater challenge lies in replicating MRI's ability to monitor treatment progress in real-time.

In this thesis, I sought to demonstrate that FLA can be performed safely and effectively in a urology clinic using MR-US fusion guidance and interstitial probes for targeting and monitoring respectively. As FLA aims to achieve oncologic control via hyperthermia, the utility of interstitial thermal probes was initially investigated. A clinical trial was performed in which FLA was safely performed in 10 patients using MR-US guidance and interstitial thermal probes for targeting and monitoring respectively. However, retrospective analysis of thermal data highlighted limitations inherent to thermal monitoring. As a result, alternative monitoring modalities were sought, with interstitial optical probes presenting a particularly promising solution.

To demonstrate a correlation between laser-tissue interaction and propagation of the coagulation boundary it is necessary to be able to visualize the latter as the treatment progresses. This cannot be achieved in ex vivo tissue samples as no imaging modality is capable of accurately differentiating coagulated and native tissue in non-perfused samples. This considerable hurdle was navigated by developing a tissue mimicking phantom that simulates the optical and thermal properties of prostatic tissue while also facilitating visualization of the coagulation zone via MRI. An optical monitoring system was then designed, constructed and validated using the tissue mimicking phantom. The acquired data enabled development of an algorithm capable of identifying the coagulation boundary in real-time. The algorithm was subsequently evaluated in ex vivo bovine muscle and found to provide an accurate method of monitoring FLA.

## **7.2. Conclusions**

### **7.2.1. Monitoring Focal Laser Ablation with Interstitial Thermal Probes**

Focal laser ablation achieves coagulative necrosis by inducing hyperthermia through the absorption of optical energy. Monitoring the thermal response presents a potential method of ensuring the safety of critical structures and the complete coagulation of the target tumor. In our proposed approach laser targeting will be achieved with MR-US fusion; therefore, the laser fiber and thermal probe must be integrated into the existing clinical setup used for targeted biopsies. With these requirements, we designed a dual channel needle guide that attaches to an ultrasound probe in a similar manner to the guide routinely used for MR-US fusion biopsy. The two channels are parallel and separated by 8mm. One channel houses the laser fiber, while an interstitial thermal probe is inserted through the other. The thermal probe consists of a fluoro-optic probe inside a flexi-needle. The goal is to maintain laser activation until lethal temperatures are recorded by the thermal probe; thus, ensuring coagulative necrosis in all of the tissue between the laser fiber and the probe. As light is emitted from a cylindrical diffuser, it is expected that the coagulation zone will approximate a cylinder of 8mm radius. A clinical trial was undertaken to demonstrate the feasibility of performing FLA with MR-US fusion guidance and interstitial thermal probe monitoring.

Focal laser ablation was performed in 10 men using MR-US fusion guidance for targeting and interstitial thermal probes for monitoring. The goal of the trial was to demonstrate that the procedure was safe and feasible. We can conclude that these endpoints were successfully achieved as no serious adverse events reported. Although

the trial did not focus on efficacy, promising results were observed with Gleason 4 CaP found in only 40% of patients at 9-month follow-up. While these results are encouraging, considerable improvement is necessary before FLA can be widely adopted for the treatment of low and intermediate risk CaP. Greater oncologic control requires the development of improved instrumentation. The custom designed needle guide and echogenic trocar utilized in the trial were sufficient to enable MR-US fusion targeting as routinely performed during biopsy. In contrast, improved real-time monitoring was identified as a key area in need of development because the utility of interstitial thermal probes appears to be inherently limited due to inaccurate thermal models. This conclusion stems from retrospective analysis of the thermal data acquired during the clinical trial.

The Arrhenius damage model is the standard approach to estimating thermally induced cellular death. The key inputs to the model are thermal history and tissue specific kinetic parameters. These parameters have been determined by multiple groups and when combined with the thermal data from the trial we found that the Arrhenius model outputs significantly different estimates of cellular death depending on the choice of kinetic parameters ( $p < 0.01$ ). Considerable efforts have already been made by other groups to both improve the Arrhenius model and better characterize the kinetic parameters of prostate tissue. Consequently, we concluded that we should focus on the development of an alternative monitoring modality which led to interest in interstitial optical monitoring.

## **7.2.2. Monitoring Focal Laser Ablation with Interstitial Optical Probes**

In FLA, laser-tissue interaction is characterized by two coefficients: 1) the absorption coefficient, and 2) the reduced scattering coefficient. The optical penetration depth is a function of these coefficients with an increase in either coefficient resulting in decreased optical penetration. Previous studies have demonstrated that ablation causes an increase in the reduced scattering coefficient while the absorption coefficient remains relatively unchanged. Increased scatter results in reduced optical penetration; therefore, once the tissue has coagulated, photons tend to be absorbed closer to the laser fiber. This 'light trap' represents a limitation of FLA as it prevents the creation of large ablation zones. However, we sought to utilize this limitation as a mechanism for identifying the coagulation boundary by interrogating the optical response during FLA.

We hypothesized that the signal recorded by an interstitial optical probe would decrease with the growth of the ablation zone during FLA and reach a plateau/inflection point once the coagulation boundary has propagated up to the sensor. Therefore, the desired ablation radius could potentially be achieved by placing an interstitial optical probe at the requisite distance from the laser fiber and terminating laser activation once a signal plateau is observed. The optical probe may be used instead of or in conjunction with the interstitial thermal probe deployed in our clinical trial.

A series of preliminary experiments were undertaken to ascertain whether or not this approach warranted further investigation. FLA was performed in ex vivo bovine muscle with both interstitial thermal probes and interstitial optical probes employed as monitoring modalities. The predicted signal plateau was observed while there was no obvious correlation between thermal data and the propagation of the coagulation

boundary. It was therefore concluded that optical monitoring may present a viable alternative to interstitial thermal probes with further investigations necessary to demonstrate utility. In addition, these experiments identified the lack of an appropriate model as a key barrier to the development of novel FLA monitoring modalities such as optical monitoring. Ex vivo tissue is not a suitable model as it is not possible to non-invasively quantify the growth of the ablation zone; therefore, the ablation zone cannot be correlated with the signal recorded by an interstitial optical probe. An appropriate model must have the following characteristics: 1) optical and thermal properties matched to prostatic tissue, 2) sufficiently solid to support needle insertion, and 3) enable non-invasive quantification of the growth of the ablation zone.

We created the requisite model through the development of a tissue mimicking prostate phantom consisting of a polyacrylamide hydrogel with optical properties matched to prostate. The gel was doped with Naphthol Green B to match the absorption coefficient of prostatic tissue while Intralipid and BSA were used to match the reduced scattering coefficient. The necessary concentration of each ingredient was determined via fluence measurements and light diffusion theory. The phantom was then validated by comparing the thermal response during FLA with that observed in the clinical trial. Both the thermal response and the shape of the induced coagulation zone were found to be similar to that observed clinically. In addition, coagulation of the BSA facilitates non-invasive quantification of the coagulation zone via  $T_2$ -weighted MRI. This is an important characteristic for the development of the proposed optical monitoring system as it facilitates correlation of the optical signal with the growth of the coagulation zone.

Finally, an interstitial optical monitoring system was designed, constructed and evaluated using the tissue mimicking phantom. The primary components of this system

are an interstitial optical probe, an amplified photodetector, a microcontroller and a dedicated PC running custom built software. A cine MRI sequence was also developed to rapidly acquire images during FLA and thus enable tracking of the expanding ablation zone. This sequence along with the phantom should find further utility in the development of FLA instrumentation.

A total of four interstitial optical probe designs were evaluated. The distinguishing feature between each is the range of angles over which light is collected. The utility of each probe was assessed by performing FLA in the tissue mimicking phantom with simultaneous MRI and optical monitoring. Three of the probes ('Ballistic', 'Spherical' and 'Radial') were found to be suitable for monitoring focal laser ablation. Ultimately, the 'Ballistic' probe was identified as the best design as it can easily be expanded to a multi-element probe. A feedback algorithm was developed based on the acquired data. The algorithm monitors the instantaneous rate of change of the optical signal and notifies the user when an inflection point has been reached. The inflection point was shown to correlate with the instant the coagulation boundary reaches the sensor. The feedback algorithm was subsequently validated in ex vivo bovine muscle. Predefined coagulation radii were successfully achieved with a mean absolute error of  $0.3\pm 0.1$ mm.

In conclusion, an interstitial optical monitoring system was developed and demonstrated to be capable of identifying the ablation boundary during FLA. The system can be deployed in a similar fashion to the thermal probes used in the clinical trial in chapter 3. Further work is necessary to create multi-element optical probes capable of distributed sensing. In addition, the system must be validated against histologically quantified ablation zones in human prostate.



### **7.2.3. Impact on Prostate Cancer Management**

It is widely recognized that there is a need to develop a treatment for prostate cancer with fewer associated complications than radical prostatectomy and radiation therapy. FLA has shown considerable promise; however, current investigations utilize MRI to both guide the laser to the desired ROI and monitor the growth of the ablation zone. Widespread adoption of FLA is likely to be hindered due to the cost and limited availability of MRI. The work presented in this thesis shows that FLA can be safely performed in a urology clinic without direct MRI. This represents a substantial development as it ensures that a large number of patients can be treated. However, in order for FLA to be considered a viable treatment, efficacy must be comparable to current gold standard treatments. In an effort to ensure efficacy, we developed an optical monitoring system which must be validated in further pre-clinical and clinical studies. If successful, FLA may provide a solution for CaP with minimal side-effects. This is particularly beneficial for patients diagnosed with low-to-intermediate risk CaP. This cohort is currently faced with the dilemma of living with CaP or undergoing treatment resulting in a reduction in quality of life due to treatment complications. Many of these patients elect for radical intervention due to the fear of living with a potentially life-threatening disease. FLA may provide a solution for this group and the work presented in this thesis lays the foundation for the clinical deployment of this revolutionary technology.

## **7.3. Future work**

### **7.3.1. Validation Against Histology**

In chapter 6 we derived a feedback algorithm for the optical monitoring system by testing the optical probe in the tissue mimicking phantom. The algorithm was subsequently validated in ex vivo bovine muscle. A key limitation of this work lies in the method of quantifying the ablation zone. This was achieved by photographing the ablation zone and employing an image analysis algorithm to identify the ablation boundary. While this method is a substantial improvement over direct measurement with calipers, it is unclear whether or not pixel intensity changes coincide with coagulative necrosis. To alleviate this limitation, future work should be undertaken to validate the optical monitoring system in ex vivo human prostate with histologic analysis utilized to quantify the ablation zone.

The proposed experiments should be performed under MRT surveillance. Testing rigs similar to those used in chapter 6 will be required to facilitate co-registration of the MRT and histology data along the trajectory of the laser fiber. We hypothesize that the damage zone estimated by the optical monitoring sensor will correlate with the histologically confirmed zone at least as well as that provided by the MR data. Should this prove to be correct, the study will provide robust evidence supporting the translation of FLA from the MR suite to the clinic. The associated reduction in cost and complexity may lead to widespread adoption of FLA for the treatment of prostate cancer.

### 7.3.2. Multi-element Thermal and Optical Probe

The outer diameter of the largest flexi-needle used in the clinical trial (chapter 3) was 2.4mm. As the diameter of the fiber optic cables can be less than 200 $\mu$ m, it should be feasible to develop an optical probe containing multiple optical sensors arrayed along the length of the probe. Given the size of the optical cables and the likely layout, it should also be possible to include multiple micro-thermocouples as depicted in Figure 57. The advantage of a linear sensor array is that some of the sensors can be used to monitor the growth of the ablation zone while others ensure the safety of surrounding structures. In particular, it is of critical importance that the rectal wall remains intact. This could be achieved by positioning the proximal sensor between the rectal wall and the distal edge of the laser fiber. In chapter 3, this task was accomplished using transperineal thermal probes; however, this approach greatly increases the complexity of the procedure.

The combined use of thermal and optical probes may lead to an improved monitoring algorithm once a feedback loop is implemented between the sensor and the laser. For example, if the tissue exhibits an unusually short penetration depth, the tissue near the fiber will coagulate rapidly. The optical sensor will show a decrease in signal while the thermal probe remains unusually low. By analyzing this data in real-time it may be possible to salvage the ablation by reducing the power output to increase the impact of the thermal conduction. Moreover, in the absence of feedback, this particular scenario would result in the formation of char around the laser fiber and which could lead to melting of the dual lumen catheter. In the worst-case scenario, the distal portion of the dual lumen catheter may detach and have to be surgically removed.

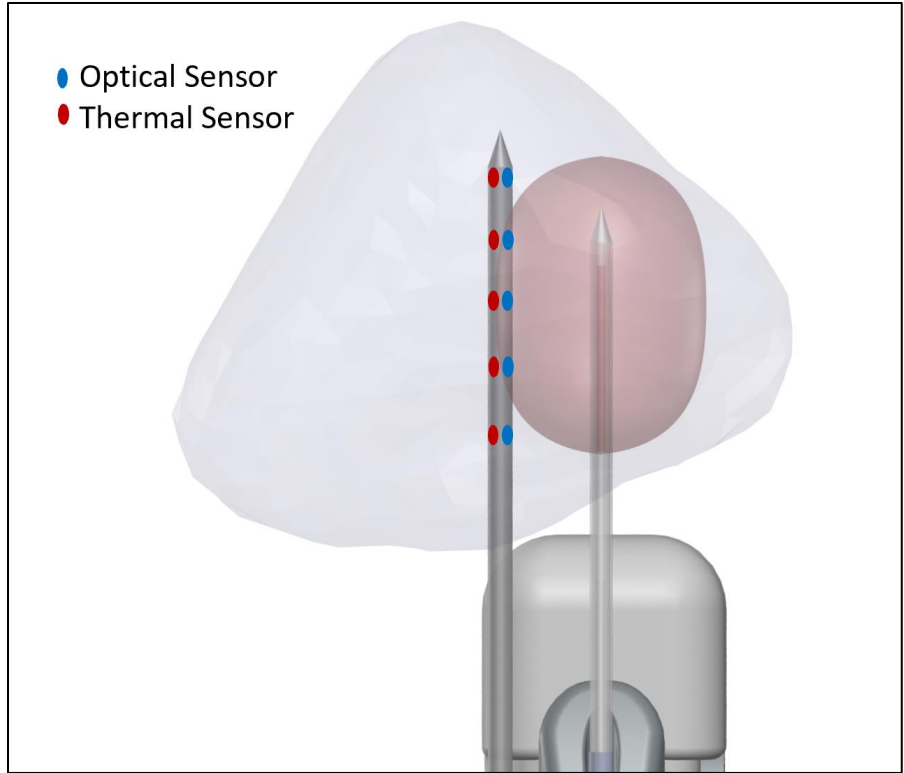


Figure 57: Proposed multi-element dual thermal and optical interstitial probe

### 7.3.3. Clinical Implementation

Our clinical study (chapter 3) demonstrated that it is both safe and feasible to perform FLA using interstitial thermal probes as a monitoring modality. A further ‘intent-to-treat’ trial must be undertaken to assess the efficacy of this procedure. With the development of a dual thermal and optical probe it will be possible to gather optical data while actively using feedback from the thermal probes as in the previous trial. The utility of optical monitoring can then be assessed via a retrospective study comparing both the optical and thermal data to the non-perfused zone observed on post-treatment MRI. This study should lead to the development of a robust feedback algorithm incorporating both optical and thermal data. Moreover, if the trial establishes that the procedure is efficacious, we can proceed to disseminate the technology to other institutions with the

ultimate goal of providing a minimally invasive treatment for the 175,000 men diagnosed with CaP every year.

## 8. References

- [1] R. L. Siegel and K. D. Miller, "Cancer Statistics , 2019," vol. 69, no. 1, pp. 7–34, 2019.
- [2] M. R. Cooperberg, "Re: Follow-up of Prostatectomy Versus Observation for Early Prostate Cancer," *Eur. Urol.*, vol. 73, no. 3, pp. 477–478, 2018.
- [3] M. Ferrer *et al.*, "Quality of life impact of treatments for localized prostate cancer : Cohort study with a 5 year follow-up," *Radiother. Oncol.*, vol. 108, no. 2, pp. 306–313, 2013.
- [4] A. Bill-Axelsson *et al.*, "Radical prostatectomy or watchful waiting in early prostate cancer.," *N. Engl. J. Med.*, vol. 370, pp. 932–42, 2014.
- [5] L. Klotz, L. Zhang, A. Lam, R. Nam, A. Mamedov, and A. Loblaw, "Clinical results of long-term follow-up of a large, active surveillance cohort with localized prostate cancer," *J. Clin. Oncol.*, vol. 28, no. 1, pp. 126–131, 2010.
- [6] E. Walser *et al.*, "Focal Laser Ablation of Prostate Cancer : Results in 120 Patients with Low- to Intermediate-Risk Disease," *J. Vasc. Interv. Radiol.*, vol. 30, no. 3, pp. 401-409.e2, 2019.
- [7] R. Van Velthoven *et al.*, "A prospective clinical trial of HIFU hemiablation for clinically localized prostate cancer," *Prostate Cancer Prostatic Dis.*, vol. 19, no. 1, pp. 79–83, 2016.
- [8] M. Valerio *et al.*, "Nanoknife electroporation ablation trial: a prospective development study investigating focal irreversible electroporation for localized prostate cancer," *J. Urol.*, vol. 197, no. 3 Part 1, pp. 647–654, 2017.
- [9] S. E. Eggener, A. Yousuf, S. Watson, S. Wang, and A. Oto, "Phase II Evaluation of MRI-Guided Focal Laser Ablation of Prostate Cancer," *J. Urol.*, no. September, pp. 3–8, 2016.
- [10] H. Lepor, E. Llukani, D. Sperling, and J. J. Futterer, "Complications, Recovery, and Early Functional Outcomes and Oncologic Control Following In-bore Focal Laser Ablation of Prostate Cancer," *Eur. Urol.*, vol. 68, no. 6, pp. 924–926, 2015.
- [11] A. Oto *et al.*, "MR Imaging – guided Focal Laser Ablation for Prostate Cancer : Phase 1 Trial," *Radiology*, vol. 267, no. 3, pp. 932–640, 2013.
- [12] M. Otori, M. W. Kattan, T. Utsunomiya, K. Suyama, P. T. Scardino, and T. M. Wheeler, "Do impalpable stage T1c prostate cancers visible on ultrasound differ from those not visible?," *J. Urol.*, vol. 169, no. 3, pp. 964–968, 2003.
- [13] F. Lee *et al.*, "Transrectal ultrasound in the diagnosis of prostate cancer: location, echogenicity, histopathology, and staging," *Prostate*, vol. 7, no. 2, pp. 117–129, 1985.
- [14] M. Otori, T. M. Wheeler, and P. T. Scardino, "The new American joint committee on cancer and international union against cancer TNM classification of prostate cancer," *Cancer*, vol. 74, no. 1, pp. 104–114, 1994.
- [15] P. Choyke and S. C. Eberhardt, "Imaging Prostate Cancer : A Multidisciplinary Perspective 1," no. May 2016, 2007.
- [16] M. Souvatzoglou *et al.*, "The sensitivity of [11C] choline PET/CT to localize prostate cancer depends on the tumor configuration," *Clin. Cancer Res.*, vol. 17, no. 11, pp. 3751–3759, 2011.
- [17] F. Russo *et al.*, "Detection of prostate cancer index lesions with multiparametric magnetic resonance imaging ( mp-MRI ) using whole-mount histological sections as the reference standard," pp. 84–94, 2016.
- [18] A. Priester *et al.*, "Magnetic Resonance Imaging Underestimation of Prostate Cancer Geometry: Use of Patient Specific Molds to Correlate Images with Whole Mount Pathology," *J. Urol.*, vol. 197, no. 2, pp. 320–326, 2017.
- [19] S. Loeb *et al.*, "Systematic Review of Complications of Prostate Biopsy," *Eur. Urol.*, vol. 64, no. 6,

- pp. 876–892, 2013.
- [20] M. Roethke *et al.*, “MRI-guided prostate biopsy detects clinically significant cancer: analysis of a cohort of 100 patients after previous negative TRUS biopsy,” *World J. Urol.*, vol. 30, no. 2, pp. 213–218, 2012.
- [21] M. M. Siddiqui *et al.*, “Comparison of MR/Ultrasound Fusion–Guided Biopsy With Ultrasound-Guided Biopsy for the Diagnosis of Prostate CancerMR/Ultrasound Fusion Biopsy for Prostate CancerMR/Ultrasound Fusion Biopsy for Prostate Cancer,” *JAMA*, vol. 313, no. 4, pp. 390–397, Jan. 2015.
- [22] F. C. Hamdy *et al.*, “10-year outcomes after monitoring, surgery, or radiotherapy for localized prostate cancer,” *N. Engl. J. Med.*, vol. 375, no. 15, pp. 1415–1424, 2016.
- [23] Piotr GAS, “Essential Facts on the History of Hyperthermia and their Connections with Electromedicine,” *Electr. Rev.*, no. 12, pp. 37–40, 2011.
- [24] M. H. Niemz, *Laser-Tissue Interactions: Fundamentals and Applications*, Third. Berlin: Springer, 2007.
- [25] B. V Bronk, “Thermal potentiation of mammalian cell killing: Clues for understanding and potential for tumor therapy,” *Adv. Radiat. Biol.*, vol. 6, pp. 267–324, 1976.
- [26] D. E. Thrall, L. Gerweck, E. L. Gillette, and W. C. Dewey, “Response of Cells In Vitro and Tissues in Vivo to Hyperthermia and X-Irradiation,” *Adv. Radiat. Biol.*, vol. 6, p. 211, 2013.
- [27] I. Har-Kedar and N. M. Bleehen, “Experimental and clinical aspects of hyperthermia applied to the treatment of cancer with special reference to the role of ultrasonic and microwave heating,” *Adv. Radiat. Biol.*, vol. 6, pp. 229–266, 1976.
- [28] E. S. Glazer and S. Curley, “The ongoing history of thermal therapy for cancer,” *Surg. Oncol. Clin. N. Am.*, vol. 20, no. 2, pp. 229–235, vii, 2011.
- [29] U. Lindner *et al.*, “Image guided photothermal focal therapy for localized prostate cancer: phase I trial,” *J. Urol.*, vol. 182, no. 4, pp. 1371–1377, 2009.
- [30] F. Wu *et al.*, “Extracorporeal high intensity focused ultrasound treatment for patients with breast cancer,” *Breast Cancer Res. Treat.*, vol. 92, no. 1, pp. 51–60, 2005.
- [31] F. Wu *et al.*, “Feasibility of US-guided high-intensity focused ultrasound treatment in patients with advanced pancreatic cancer: initial experience,” *Radiology*, vol. 236, no. 3, pp. 1034–1040, 2005.
- [32] P. Liang, Y. Wang, D. Zhang, X. Yu, Y. Gao, and X. Ni, “Ultrasound guided percutaneous microwave ablation for small renal cancer: initial experience,” *J. Urol.*, vol. 180, no. 3, pp. 844–848, 2008.
- [33] T. Livraghi, L. Solbiati, M. F. Meloni, G. S. Gazelle, E. F. Halpern, and S. N. Goldberg, “Treatment of Focal Liver Tumors with Percutaneous Radio-frequency Ablation: Complications Encountered in a Multicenter Study,” *Radiology*, vol. 226, no. 2, pp. 441–451, 2003.
- [34] Y. Zhou, “High intensity focused ultrasound in clinical tumor ablation,” *World J. Clin. Oncol.*, vol. 2, no. 1, pp. 8–27, 2011.
- [35] E. Barret *et al.*, “Morbidity of focal therapy in the treatment of localized prostate cancer,” *Eur. Urol.*, vol. 63, pp. 618–622, 2013.
- [36] D. E. Dupuy, R. J. Zagoria, W. Akerley, W. W. Mayo-Smith, P. V Kavanagh, and H. Safran, “Percutaneous radiofrequency ablation of malignancies in the lung,” *Am. J. Roentgenol.*, vol. 174, no. 1, pp. 57–59, 2000.
- [37] F. Westermarck, “Über die Behandlung des ulcerierenden Cervixcarcinoms mittels konstanter Wärme,” *Zbl. Gynakol.*, vol. 22, pp. 1335–1339, 1898.
- [38] W. B. Coley, “The treatment of malignant tumors by repeated inoculations of erysipelas,” *Am. J. Med. Sci.*, vol. 105, no. 5, pp. 487–510, 1893.
- [39] W. J. Fry, W. H. Mosberg Jr, J. W. Barnard, and F. J. Fry, “Production of focal destructive lesions in

- the central nervous system with ultrasound.," *J. Neurosurg.*, vol. 11, no. 5, pp. 471–478, 1954.
- [40] D. J. Coleman *et al.*, "Therapeutic ultrasound in the treatment of glaucoma: I. Experimental model," *Ophthalmology*, vol. 92, no. 3, pp. 339–346, 1985.
- [41] R. Muratore, "A history of the sonocare CST-100: The first FDA-approved HIFU device," *AIP Conf. Proc.*, vol. 829, no. 2006, pp. 508–512, 2006.
- [42] G. ter Haar, D. Sinnett, and I. Rivens, "High intensity focused ultrasound—a surgical technique for the treatment of discrete liver tumours," *Phys. Med. Biol.*, vol. 34, no. 11, p. 1743, 1989.
- [43] Y. Kim, H. Rhim, M. J. Choi, H. K. Lim, and D. Choi, "High-intensity focused ultrasound therapy: an overview for radiologists.," *Korean J. Radiol.*, vol. 9, no. 4, pp. 291–302, 2008.
- [44] E. van Sonnenberg, W. McMullen, and L. Solbiati, *Tumor Ablation: Principles and Practice*. New York: Springer, 2005.
- [45] Z. W. Qian, L. Xiong, J. Yu, D. Shao, H. Zhu, and X. Wu, "Noninvasive thermometer for HIFU and its scaling," *Ultrasonics*, vol. 44, no. SUPPL., pp. 31–35, 2006.
- [46] J. P. McGahan, P. D. Browning, J. M. Brock, and H. Tesluk, "Hepatic ablation using radiofrequency electrocautery.," *Invest. Radiol.*, vol. 25, no. 3, pp. 267–270, 1990.
- [47] S. Rossi, F. Fornari, C. Pathies, and L. Buscarini, "Thermal lesions induced by 480 KHz localized current field in guinea pig and pig liver.," *Tumori*, vol. 76, no. 1, pp. 54–57, 1990.
- [48] J. P. McGahan, P. Schneider, J. M. Brock, and H. Tesluk, "Treatment of liver tumors by percutaneous radiofrequency electrocautery," in *Seminars in interventional radiology*, 1993, vol. 10, no. 2, pp. 143–149.
- [49] L. W. Organ, "Electrophysiologic principles of radiofrequency lesion making," *Stereotact. Funct. Neurosurg.*, vol. 39, no. 2, pp. 69–76, 1976.
- [50] G. Carrafiello *et al.*, "Microwave tumors ablation: Principles, clinical applications and review of preliminary experiences," *Int. J. Surg.*, vol. 6, no. SUPPL. 1, pp. 65–69, 2008.
- [51] C. L. Brace, "Radiofrequency and microwave ablation of the liver, lung, kidney, and bone: what are the differences?," *Curr. Probl. Diagn. Radiol.*, vol. 38, no. 3, pp. 135–143, 2009.
- [52] T. P. Ryan, P. F. Turner, and B. Hamilton, "Interstitial microwave transition from hyperthermia to ablation: historical perspectives and current trends in thermal therapy.," *Int. J. Hyperthermia*, vol. 26, no. 5, pp. 415–433, 2010.
- [53] T. P. Ryan, B. S. Trembly, D. W. Roberts, J. W. Strohbehn, C. T. Coughlin, and P. J. Hoopes, "Brain hyperthermia: I. Interstitial microwave antenna array techniques—the Dartmouth experience," *Int. J. Radiat. Oncol. Biol. Phys.*, vol. 29, no. 5, pp. 1065–1078, 1994.
- [54] M. D. Sherar, J. Trachtenberg, S. R. H. Davidson, and M. R. Gertner, "Interstitial microwave thermal therapy and its application to the treatment of recurrent prostate cancer," *Int. J. Hyperth.*, vol. 20, no. 7, pp. 757–768, 2004.
- [55] P. K. Sneed *et al.*, "Survival benefit of hyperthermia in a prospective randomized trial of brachytherapy boost±hyperthermia for glioblastoma multiforme," *Int. J. Radiat. Oncol. Biol. Phys.*, vol. 40, no. 2, pp. 287–295, 1998.
- [56] C. T. Coughlin *et al.*, "Interstitial microwave-induced hyperthermia and iridium brachytherapy for the treatment of obstructing biliary carcinomas," *Int. J. Hyperth.*, vol. 8, no. 2, pp. 157–171, 1992.
- [57] M. H. Seegenschmiedt, P. Martus, R. Fietkau, H. Iro, L. W. Brady, and R. Sauer, "Multivariate analysis of prognostic parameters using interstitial thermoradiotherapy (IHT-IRT): Tumor and treatment variables predict outcome," *Int. J. Radiat. Oncol. Biol. Phys.*, vol. 29, no. 5, pp. 1049–1063, 1994.
- [58] J. Overgaard *et al.*, "Randomised trial of hyperthermia as adjuvant to radiotherapy for recurrent or metastatic malignant melanoma," *Lancet*, vol. 345, no. 8949, pp. 540–543, 1995.



- [59] E. L. Jones *et al.*, "Randomized trial of hyperthermia and radiation for superficial tumors," *J. Clin. Oncol.*, vol. 23, no. 13, pp. 3079–3085, 2005.
- [60] P. Liang and Y. Wang, "Microwave ablation of hepatocellular carcinoma," *Oncology*, vol. 72, no. Suppl. 1, pp. 124–131, 2007.
- [61] F. J. Wolf, D. J. Grand, J. T. Machan, T. A. DiPetrillo, W. W. Mayo-Smith, and D. E. Dupuy, "Microwave ablation of lung malignancies: effectiveness, CT findings, and safety in 50 patients," *Radiology*, vol. 247, no. 3, pp. 871–879, 2008.
- [62] P. Liang, Y. Wang, D. Zhang, X. Yu, Y. Gao, and X. Ni, "Ultrasound guided percutaneous microwave ablation for small renal cancer: initial experience.," *J. Urol.*, vol. 180, no. 3, pp. 844–848; discussion 848, 2008.
- [63] C. J. Simon, D. E. Dupuy, and W. W. Mayo-Smith, "Microwave ablation: principles and applications," *Radiographics*, vol. 25, no. suppl\_1, pp. S69–S83, 2005.
- [64] N. J. Lygidakis *et al.*, "Microwave ablation in locally advanced pancreatic carcinoma--a new look.," *Hepatogastroenterology.*, vol. 54, no. 77, pp. 1305–1310, 2006.
- [65] J. C. Chen *et al.*, "Prostate Cancer: MR Imaging and Thermometry during Microwave Thermal Ablation-Initial Experience," *Radiology*, vol. 214, no. 1, pp. 290–297, 2000.
- [66] C. J. Simon, D. E. Dupuy, and W. W. Mayo-Smith, "Microwave ablation: principles and applications.," *Radiographics*, vol. 25 Suppl 1, pp. S69–S83, 2005.
- [67] M. G. Lubner, C. L. Brace, J. L. Hinshaw, and F. T. Lee, "Microwave tumor ablation: mechanism of action, clinical results, and devices," *J. Vasc. Interv. Radiol.*, vol. 21, no. 8, pp. S192–S203, 2010.
- [68] M. Kuang *et al.*, "Liver Cancer : Increased Microwave Delivery to Ablation Zone with Cooled- Shaft Antenna — Experimental and Clinical studies," *Radiology*, vol. 242, no. 3, pp. 914–924, 2007.
- [69] D. Hashimoto, "Clinical application of the thermal effect of lasers. 2. Application of the laser thermal effect to the therapy of liver neoplasms.," *Nihon Rinsho.*, vol. 45, no. 4, pp. 888–896, 1987.
- [70] J. Hahl, R. Haapiainen, J. Ovaska, P. Puolakkainen, and T. Schröder, "Laser-Induced hyperthermia in the treatment of liver tumors," *Lasers Surg. Med.*, vol. 10, no. 4, pp. 319–321, 1990.
- [71] K. Dowlatshahi, A. K. Bhattacharya, B. Silver, T. Matalon, and J. W. Williams, "Percutaneous interstitial laser therapy of a patient with recurrent hepatoma in a transplanted liver.," *Surgery*, vol. 112, no. 3, pp. 603–606, 1992.
- [72] C. P. Nolsøe *et al.*, "Interstitial hyperthermia of colorectal liver metastases with a US-guided Nd-YAG laser with a diffuser tip: a pilot clinical study.," *Radiology*, vol. 187, no. 2, pp. 333–337, 1993.
- [73] S. Natarajan *et al.*, "Focal Laser Ablation of Prostate Cancer: Phase I Clinical Trial.," *J. Urol.*, vol. 196, no. 1, pp. 68–75, 2016.
- [74] K. H. Haraldsdóttir, K. Ivarsson, S. Góttberg, C. Ingvar, U. Stenram, and K. G. Tranberg, "Interstitial laser thermotherapy (ILT) of breast cancer," *Eur. J. Surg. Oncol.*, vol. 34, no. 7, pp. 739–745, 2008.
- [75] E. A. Dick *et al.*, "MR-guided laser thermal ablation of primary and secondary liver tumours," *Clin. Radiol.*, vol. 58, no. 2, pp. 112–120, 2003.
- [76] C. Rosenberg *et al.*, "Laser Ablation of Metastatic Lesions of the Lung: Long-Term Outcome," *Am. J. Roentgenol.*, vol. 192, no. 3, pp. 785–792, 2009.
- [77] A. Carpentier *et al.*, "Real-time magnetic resonance-guided laser thermal therapy for focal metastatic brain tumors," *Neurosurgery*, vol. 63, no. 1 SUPPL., pp. 21–29, 2008.
- [78] F. Izzo, "Other thermal ablation techniques: microwave and interstitial laser ablation of liver tumors," *Ann. Surg. Oncol.*, vol. 10, no. 5, pp. 491–497, 2003.
- [79] J. Civale, R. Clarke, I. Rivens, and G. ter Haar, "The use of a segmented transducer for rib sparing in HIFU treatments," *Ultrasound Med. Biol.*, vol. 32, no. 11, pp. 1753–1761, 2006.
- [80] K. Kajiyama, K. Yoshinaka, S. Takagi, and Y. Matsumoto, "Micro-bubble enhanced HIFU," *Phys.*

- Procedia*, vol. 3, no. 1, pp. 305–314, 2010.
- [81] T. W. Davison, K. L. Ewing, J. Fergason, M. Chapman, A. Can, and C. C. Voorhis, “Detection of breast cancer by liquid crystal thermography. A preliminary report,” *Cancer*, vol. 29, no. 5, pp. 1123–1132, 1972.
- [82] B. C. Wilson and D. R. Wyman, “Optical and thermal dosimetry,” in *Lasers in Medicine*, R. W. Waynant, Ed. Boca Raton: CRC Press, 2002, pp. 47–84.
- [83] J. W. Hand, A. Shaw, N. Sadhoo, S. Rajagopal, R. J. Dickinson, and L. R. Gavrilov, “A random phased array device for delivery of high intensity focused ultrasound,” *Phys. Med. Biol.*, vol. 54, no. 19, pp. 5675–93, 2009.
- [84] K. Ogan *et al.*, “Infrared thermography and thermocouple mapping of radiofrequency renal ablation to assess treatment adequacy and ablation margins,” *Urology*, vol. 62, no. 1, pp. 146–151, 2003.
- [85] V. Zderic, J. Foley, W. Luo, and S. Vaezy, “Prevention of post-focal thermal damage by formation of bubbles at the focus during high intensity focused ultrasound therapy,” *Med. Phys.*, vol. 35, no. 10, pp. 4292–4299, 2008.
- [86] P. R. Patel *et al.*, “In vitro and in vivo evaluations of increased effective beam width for heat deposition using a split focus high intensity ultrasound (HIFU) transducer,” *Int. J. Hyperthermia*, vol. 24, no. 7, pp. 537–549, 2008.
- [87] S. S. Wang *et al.*, “Microwave radiometric thermometry and its potential applicability to ablative therapy,” *J. Interv. Card. Electrophysiol.*, vol. 4, no. 1, pp. 295–300, 2000.
- [88] L. Frich, “Non-invasive thermometry for monitoring hepatic radiofrequency ablation,” *Minim. Invasive Ther. Allied Technol.*, vol. 15, no. 1, pp. 18–25, 2006.
- [89] A. Vander Vorst, A. Rosen, and Y. Kotsuka, *RF/Microwave Interaction with Biological Tissues*. 2006.
- [90] K. Hynynen, C. J. Martin, D. J. Watmough, and J. R. Mallard, “Errors in temperature measurement by thermocouple probes during ultrasound induced hyperthermia,” *Br. J. Radiol.*, vol. 56, no. 672, pp. 969–970, 1983.
- [91] J. J. Langberg *et al.*, “Temperature monitoring during radiofrequency catheter ablation of accessory pathways,” *Circulation*, vol. 86, no. 5, pp. 1469–74, 1992.
- [92] J. Fraden, “Temperature sensors,” in *Handbook of Modern Sensors: Physics, Designs, and Applications*, 4th ed., J. Fraden, Ed. New York: Springer, 2010, pp. 519–569.
- [93] R. Van Hillegersberg, H. J. Van Staveren, W. J. Kort, P. E. Zondervan, and O. T. Terpstra, “Interstitial Nd: YAG laser coagulation with a cylindrical diffusing fiber tip in experimental liver metastases,” *Lasers Surg. Med.*, vol. 14, no. 2, pp. 124–138, 1994.
- [94] B. D. Fornage *et al.*, “Small Breast Cancer Treated with US-guided Radiofrequency Ablation: Feasibility Study,” *Radiology*, vol. 231, no. 11, pp. 215–224, 2004.
- [95] L. Solbiati *et al.*, “Percutaneous radio-frequency ablation of hepatic metastases from colorectal cancer: long-term results in 117 patients,” *Radiology*, vol. 221, no. 1, pp. 159–166, 2001.
- [96] P. Liang, Y. Wang, X. Yu, and B. Dong, “Malignant Liver Tumors: Treatment with Percutaneous Microwave Ablation—Complications among Cohort of 1136 Patients,” *Radiology*, vol. 251, no. 3, pp. 933–940, 2009.
- [97] H. Liu and K. Steinke, “High-powered percutaneous microwave ablation of stage i medically inoperable non-small cell lung cancer: A preliminary study,” *J. Med. Imaging Radiat. Oncol.*, vol. 57, no. 4, pp. 466–474, 2013.
- [98] K. Dowlatshahi, S. Wadhvani, R. Alvarado, C. Valadez, and J. Dieschbourg, “Short communication interstitial laser therapy of breast fibroadenomas with 6 and 8 year follow-up,” *Breast J.*, vol. 16, no. 1, pp. 73–76, 2010.

- [99] G. Tsoumakidou, M.-A. Thénint, J. Garnon, X. Buy, J.-P. Steib, and A. Gangi, "Percutaneous Image-guided Laser Photocoagulation of Spinal Osteoid Osteoma: A Single-Institution Series," *Radiology*, vol. 278, no. 3, p. 150491, 2016.
- [100] F. Hübner, B. Bazrafshan, J. Roland, A. Kickhefel, and T. J. Vogl, "The influence of Nd: YAG laser irradiation on Fluoroptic® temperature measurement: an experimental evaluation," *Lasers Med. Sci.*, vol. 28, no. 2, pp. 487–496, 2013.
- [101] M. Van Den Bosch, B. Daniel, V. Rieke, K. Butts-Pauly, E. Kermit, and S. Jeffrey, "MRI-guided radiofrequency ablation of breast cancer: Preliminary clinical experience," *J. Magn. Reson. Imaging*, vol. 27, no. 1, pp. 204–208, 2008.
- [102] C. Doyle, "Fibre Bragg Grating Sensors-An Introduction to Bragg gratings and interrogation techniques," *Smart Fibres Ltd*, no. 1, pp. 1–5, 2003.
- [103] E. G. Macchi *et al.*, "Optical fiber sensors-based temperature distribution measurement in ex vivo radiofrequency ablation with submillimeter resolution.," *J. Biomed. Opt.*, vol. 19, no. 11, p. 117004, 2014.
- [104] P. Saccomandi, E. Schena, and S. Silvestri, "Techniques for temperature monitoring during laser-induced thermotherapy: an overview.," *Int. J. Hyperthermia*, vol. 29, no. 7, pp. 609–19, 2013.
- [105] I. Rivens, a Shaw, J. Civale, and H. Morris, "Treatment monitoring and thermometry for therapeutic focused ultrasound.," *Int. J. Hyperthermia*, vol. 23, no. 2, pp. 121–139, 2007.
- [106] W. H. Chen, N. T. Sanghvi, R. Carlson, G. Schatzl, and M. Marberger, "Validation of tissue change monitoring (TCM) on the Sonablate 500 during high intensity focused ultrasound (HIFU) treatment of prostate cancer with real-time thermometry," *AIP Conf. Proc.*, vol. 1481, pp. 53–58, 2012.
- [107] F. Bertsch *et al.*, "Non-invasive temperature mapping using MRI: comparison of two methods based on chemical shift and T1-relaxation," *Magn. Reson. Imaging*, vol. 16, no. 4, pp. 393–403, 1998.
- [108] P. Baron *et al.*, "In vivo T2-based MR thermometry in adipose tissue layers for high-intensity focused ultrasound near-field monitoring," *Magn. Reson. Med.*, vol. 72, no. 4, pp. 1057–1064, 2014.
- [109] L. R. Kozak, M. Bango, M. Szabo, G. Rudas, Z. Vidnyanszky, and Z. Nagy, "Using diffusion MRI for measuring the temperature of cerebrospinal fluid within the lateral ventricles," *Acta Paediatr. Int. J. Paediatr.*, vol. 99, no. 2, pp. 237–243, 2010.
- [110] V. Rieke and K. B. Pauly, "MR thermometry," *J. Magn. Reson. Imaging*, vol. 27, pp. 376–390, 2008.
- [111] V. Rieke, K. K. Vigen, G. Sommer, B. L. Daniel, J. M. Pauly, and K. Butts, "Referenceless PRF shift thermometry," *Magn. Reson. Med.*, vol. 51, pp. 1223–1231, 2004.
- [112] A. Kickhefel *et al.*, "A pilot study for clinical feasibility of the near-harmonic 2D referenceless PRFS thermometry in liver under free breathing using MR-guided LITT ablation data," *Int. J. Hyperth.*, vol. 28, no. 3, pp. 250–266, 2012.
- [113] A. B. Holbrook, P. Ghanouni, J. M. Santos, C. Dumoulin, Y. Medan, and K. B. Pauly, "Respiration based steering for high intensity focused ultrasound liver ablation," *Magn. Reson. Med.*, vol. 71, no. 2, pp. 797–806, 2014.
- [114] R. R. Bitton, T. D. Webb, K. B. Pauly, and P. Ghanouni, "Improving thermal dose accuracy in magnetic resonance-guided focused ultrasound surgery: Long-term thermometry using a prior baseline as a reference," *J. Magn. Reson. Imaging*, vol. 43, no. 1, pp. 181–189, 2016.
- [115] L. Winter *et al.*, "Magnetic resonance thermometry: Methodology, pitfalls and practical solutions," *Int. J. Hyperth.*, vol. 32, no. 1, pp. 63–75, 2016.
- [116] T. D. Khokhlova *et al.*, "Magnetic resonance imaging of boiling induced by high intensity focused ultrasound.," *J. Acoust. Soc. Am.*, vol. 125, no. 4, pp. 2420–2431, 2009.

- [117] M. Lepetit-Coiffé *et al.*, “Real-time monitoring of radiofrequency ablation of rabbit liver by respiratory-gated quantitative temperature MRI,” *J. Magn. Reson. Imaging*, vol. 24, no. 1, pp. 152–159, 2006.
- [118] K. Hynynen, “MRI-guided focused ultrasound treatments,” *Ultrasonics*, vol. 50, no. 2, pp. 221–229, 2010.
- [119] G. D. Pandeya *et al.*, “Feasibility of computed tomography based thermometry during interstitial laser heating in bovine liver,” *Eur. Radiol.*, vol. 21, no. 8, pp. 1733–1738, 2011.
- [120] P. Bruners *et al.*, “CT-based temperature monitoring during hepatic RF ablation: Feasibility in an animal model,” *Int. J. Hyperth.*, vol. 28, no. 1, pp. 55–61, 2012.
- [121] F. Fani, E. Schena, P. Saccomandi, and S. Silvestri, “CT-based thermometry: An overview,” *Int. J. Hyperth.*, vol. 30, no. 4, pp. 219–227, 2014.
- [122] F. C. Henriques Jr, “Studies of thermal injury; the predictability and the significance of thermally induced rate processes leading to irreversible epidermal injury.,” *Arch. Pathol.*, vol. 43, no. 5, pp. 489–502, 1947.
- [123] F. C. Henriques Jr and A. R. Moritz, “Studies of thermal injury: I. The conduction of heat to and through skin and the temperatures attained therein. A theoretical and an experimental investigation\*,” *Am. J. Pathol.*, vol. 23, no. 4, p. 530, 1947.
- [124] A. R. Moritz and F. C. Henriques, “Studies of thermal injury II: The relative importance of time and surface temperature in the causation of cutaneous burns.,” *Am J Path*, vol. 23, p. 659, 1947.
- [125] A. R. Moritz, “Studies of thermal injury III: the pathology and pathogenesis of cutaneous burns. an experimental study,” *Am. J. Pathol.*, vol. 23, no. 6, p. 915, 1947.
- [126] W. C. Dewey, “Arrhenius relationships from the molecule and cell to the clinic.,” *Int. J. Hyperthermia*, vol. 25, no. 1, pp. 3–20, 2009.
- [127] S. A. Sapareto and W. C. Dewey, “Thermal dose determination in cancer therapy,” *Int. J. Radiat. Oncol.*, vol. 10, no. 6, pp. 787–800, Apr. 1984.
- [128] M. W. Dewhurst, B. L. Viglianti, M. Lora-Michiels, M. Hanson, and P. J. Hoopes, “Basic principles of thermal dosimetry and thermal thresholds for tissue damage from hyperthermia.,” *Int. J. Hyperthermia*, vol. 19, no. 3, pp. 267–294, 2003.
- [129] X. He, S. Bhowmick, and J. C. Bischof, “Thermal therapy in urologic systems: a comparison of arrhenius and thermal isoeffective dose models in predicting hyperthermic injury.,” *J. Biomech. Eng.*, vol. 131, no. 7, p. 074507, 2009.
- [130] P. Bhowmick *et al.*, “In vitro assessment of the efficacy of thermal therapy in human benign prostatic hyperplasia.,” *Int. J. Hyperthermia*, vol. 20, no. 4, pp. 421–439, 2004.
- [131] C. J. MacLellan *et al.*, “A methodology for thermal dose model parameter development using perioperative MRI,” *Int. J. Hyperth.*, vol. 34, no. 6, pp. 1–10, 2017.
- [132] J. G. R. Bomers *et al.*, “MRI-guided focal laser ablation for prostate cancer followed by radical prostatectomy: correlation of treatment effects with imaging,” *World J. Urol.*, vol. 35, no. 5, pp. 703–711, 2016.
- [133] M. N. Rylander, Y. Feng, K. Zimmermann, and K. R. Diller, “Measurement and mathematical modeling of thermally induced injury and heat shock protein expression kinetics in normal and cancerous prostate cells.,” *Int. J. Hyperthermia*, vol. 26, no. 8, pp. 748–764, 2010.
- [134] X. He and J. C. Bischof, “The kinetics of thermal injury in human renal carcinoma cells,” *Ann. Biomed. Eng.*, vol. 33, no. 4, pp. 502–510, 2005.
- [135] L. P. Walsh *et al.*, “In Vitro Assessment of the Efficacy of Thermal Therapy in Human Renal Cell Carcinoma,” *Urology*, vol. 70, no. 2, pp. 380–384, 2007.
- [136] J. A. Weaver and A. M. Stoll, “Mathematical model of skin exposed to thermal radiation,” *Plast.*

- Reconstr. Surg.*, vol. 44, no. 3, 1969.
- [137] A. Takata, "Development of Criterion for Skin Burns," *Aerosp. Med.*, vol. 45, no. 6, pp. 634–637, Jan. 1974.
- [138] M. A. Lewis, R. M. Staruch, and R. Chopra, "Thermometry and ablation monitoring with ultrasound," *Int. J. Hyperth.*, vol. 31, no. 2, pp. 163–181, 2015.
- [139] F. Y. Liu *et al.*, "Microwave ablation assisted by a real-time virtual navigation system for hepatocellular carcinoma undetectable by conventional ultrasonography," *Eur. J. Radiol.*, vol. 81, no. 7, pp. 1455–1459, 2012.
- [140] Y. Minami *et al.*, "Contrast harmonic sonography-guided radiofrequency ablation therapy versus B-mode sonography in hepatocellular carcinoma: Prospective randomized controlled trial," *Am. J. Roentgenol.*, vol. 188, no. 2, pp. 489–494, 2007.
- [141] Z. Amin, S. G. Bown, and W. R. Lees, "Local treatment of colorectal liver metastases: A comparison of Interstitial Laser Photocoagulation (ILP) and Percutaneous Alcohol Injection (PAI)," *Clin. Radiol.*, vol. 48, no. 3, pp. 166–171, 1993.
- [142] S. Zhang *et al.*, "Feasibility of using Nakagami distribution in evaluating the formation of ultrasound-induced thermal lesions," *J. Acoust. Soc. Am.*, vol. 131, no. 6, pp. 4836–4844, 2012.
- [143] S. Zhang *et al.*, "Feasibility of Using Ultrasonic Nakagami Imaging for Monitoring Microwave-Induced Thermal Lesion in Ex Vivo Porcine Liver," *Ultrasound Med. Biol.*, vol. 43, no. 2, pp. 482–493, 2017.
- [144] Z. Zhou, S. Wu, C. Y. Wang, H. Y. Ma, C. C. Lin, and P. H. Tsui, "Monitoring radiofrequency ablation using real-time ultrasound nakagami imaging combined with frequency and temporal compounding techniques," *PLoS One*, vol. 10, no. 2, 2015.
- [145] M. Wink *et al.*, "Contrast-enhanced ultrasound and prostate cancer; a multicentre European research coordination project," *Eur. Urol.*, vol. 54, no. 5, pp. 982–993, 2008.
- [146] U. Lindner *et al.*, "Focal Laser Ablation for Prostate Cancer Followed by Radical Prostatectomy: Validation of Focal Therapy and Imaging Accuracy," *Eur. Urol.*, vol. 57, no. 6, pp. 1111–1114, 2010.
- [147] Y. Wang, W. Wang, and H. Ye, "Contrast-enhanced ultrasonography assessment of therapeutic efficacy for ultrasound-guided high-intensity focused ultrasound ablation of uterine fibroids: comparison with contrast-enhanced magnetic resonance," *J. Med. Ultrasound*, vol. 22, no. 1, pp. 22–28, 2014.
- [148] F. Liu, X. Yu, P. Liang, Z. Cheng, Z. Han, and B. Dong, "Contrast-enhanced ultrasound-guided microwave ablation for hepatocellular carcinoma inconspicuous on conventional ultrasound," *Int. J. Hyperth.*, vol. 27, no. 6, pp. 555–562, Jul. 2011.
- [149] L. Solbiati, T. Ierace, M. Tonolini, and L. Cova, "Guidance and monitoring of radiofrequency liver tumor ablation with contrast-enhanced ultrasound," *Eur. J. Radiol.*, vol. 51, pp. S19–S23, 2004.
- [150] S. Peng *et al.*, "Intraprocedure contrast enhanced ultrasound: The value in assessing the effect of ultrasound-guided high intensity focused ultrasound ablation for uterine fibroids," *Ultrasonics*, vol. 58, pp. 123–128, 2015.
- [151] J. E. Kennedy *et al.*, "Contrast-enhanced ultrasound assessment of tissue response to high-intensity focused ultrasound," *Ultrasound Med. Biol.*, vol. 30, no. 6, pp. 851–854, 2004.
- [152] M. Frieser *et al.*, "Efficacy of contrast-enhanced US versus CT or MRI for the therapeutic control of percutaneous radiofrequency ablation in the case of hepatic malignancies," *Ultraschall der Medizin*, vol. 32, no. 2, pp. 148–153, 2011.
- [153] D. Shahmirzadi, G. Y. Hou, J. Chen, and E. E. Konofagou, "Ex vivo characterization of canine liver tissue viscoelasticity after high-intensity focused ultrasound ablation," *Ultrasound Med. Biol.*, vol. 40, no. 2, pp. 341–350, 2014.

- [154] E. S. Brosses, M. Pernot, and M. Tanter, "The link between tissue elasticity and thermal dose in vivo.," *Phys. Med. Biol.*, vol. 56, no. 24, pp. 7755–65, 2011.
- [155] J. L. Gennisson, T. Defieux, M. Fink, and M. Tanter, "Ultrasound elastography: Principles and techniques," *Diagn. Interv. Imaging*, vol. 94, no. 5, pp. 487–495, 2013.
- [156] M. Fatemi and J. F. Greenleaf, "Vibro-acoustography: an imaging modality based on ultrasound-stimulated acoustic emission.," *Proc. Natl. Acad. Sci. U. S. A.*, vol. 96, no. 12, pp. 6603–8, 1999.
- [157] J. F. Greenleaf and M. Fatemi, "Ultrasound-Stimulated Vibro-Acoustic Imaging," in *IEEE Ultrasonics Symposium*, 1998, pp. 1635–1638.
- [158] T. Karjalainen, J. S. Thierman, and K. Hynynen, "Ultrasound acoustic stimulated emission for controlling thermal surgery," *1999 IEEE Ultrason. Symp. Proceedings, Vols 1 2*, pp. 1397–1400, 1999.
- [159] F. G. Mitri *et al.*, "Prostate cryotherapy monitoring using vibroacoustography: Preliminary results of an ex vivo study and technical feasibility," *IEEE Trans. Biomed. Eng.*, vol. 55, no. 11, pp. 2584–2592, 2008.
- [160] A. Alizad *et al.*, "Application of vibro-acoustography in prostate tissue imaging.," *Med. Phys.*, vol. 40, no. 2, p. 022902, 2013.
- [161] K. R. Nightingale, M. L. Palmeri, R. W. Nightingale, and G. E. Trahey, "On the feasibility of remote palpation using acoustic radiation force.," *J. Acoust. Soc. Am.*, vol. 110, no. 1, pp. 625–34, 2001.
- [162] K. R. Nightingale, M. S. Soo, R. W. Nightingale, and G. E. Trahey, "Acoustic radiation force impulse imaging: in vivo demonstration of clinical feasibility.," *Ultrasound Med Biol*, vol. 28, no. 2, pp. 227–235, 2002.
- [163] M. L. Palmeri and K. R. Nightingale, "On the thermal effects associated with radiation force imaging of soft tissue," *IEEE Trans. Ultrason. Ferroelectr. Freq. Control*, vol. 51, no. 5, pp. 551–565, 2004.
- [164] B. J. Fahey, K. R. Nightingale, S. A. McAleavey, M. L. Palmeri, P. D. Wolf, and G. E. Trahey, "Acoustic radiation force impulse imaging of myocardial radiofrequency ablation: Initial in vivo results," *IEEE Trans. Ultrason. Ferroelectr. Freq. Control*, vol. 52, no. 4, pp. 631–641, 2005.
- [165] S. A. Eyerly, S. J. Hsu, S. H. Agashe, G. E. Trahey, Y. Li, and P. D. Wolf, "An in vitro assessment of acoustic radiation force impulse imaging for visualizing cardiac radiofrequency ablation lesions," *J. Cardiovasc. Electrophysiol.*, vol. 21, no. 5, pp. 557–563, 2010.
- [166] U. L. Tra, S. Im, and A. G. Ing, "Combined Ultrasonic Thermal Ablation with Interleaved ARFI Image Monitoring Using a Single Diagnostic Curvilinear Array : A Feasibility Study," vol. 232, no. 2011, pp. 217–232, 2012.
- [167] B. J. Fahey, R. C. Nelson, S. J. Hsu, D. P. Bradway, D. M. Dumont, and G. E. Trahey, "In Vivo Guidance and Assessment of Liver Radio-Frequency Ablation with Acoustic Radiation Force Elastography," *Ultrasound Med. Biol.*, vol. 34, no. 10, pp. 1590–1603, 2008.
- [168] H. J. Kwon *et al.*, "Acoustic radiation force impulse elastography for hepatocellular carcinoma-associated radiofrequency ablation," *World J. Gastroenterol.*, vol. 17, no. 14, pp. 1874–1878, 2011.
- [169] J. Bercoff, M. Tanter, and M. Fink, "Supersonic shear imaging: A new technique for soft tissue elasticity mapping," *IEEE Trans. Ultrason. Ferroelectr. Freq. Control*, vol. 51, no. 4, pp. 396–409, 2004.
- [170] A. P. Sarvazyan, O. V Rudenko, S. D. Swanson, J. B. Fowlkes, and S. Y. Emelianov, "Shear Wave Elasticity Imaging : A new ultrasonic technology of medical diagnostic," *Ultrasound Med. Biol.*, vol. 24, no. 9, pp. 1419–1435, 1998.
- [171] J. Bercoff, M. Tanter, and M. Fink, "Sonic boom in soft materials: The elastic Cerenkov effect," *Appl. Phys. Lett.*, vol. 84, no. 12, pp. 2202–2204, 2004.
- [172] A. Mariani *et al.*, "Real time shear waves elastography monitoring of thermal ablation: In vivo

- evaluation in pig livers," *J. Surg. Res.*, vol. 188, no. 1, pp. 37–43, 2014.
- [173] E. E. Konofagou and K. Hynynen, "Localized harmonic motion imaging: Theory, simulations and experiments," *Ultrasound Med. Biol.*, vol. 29, no. 10, pp. 1405–1413, 2003.
- [174] C. Maleke and E. E. Konofagou, "Harmonic motion imaging for focused ultrasound (HMIFU): a fully integrated technique for sonication and monitoring of thermal ablation in tissues.," *Phys. Med. Biol.*, vol. 53, no. 6, pp. 1773–1793, 2008.
- [175] E. E. Konofagou, C. Maleke, and J. Vappou, "Harmonic motion imaging (HMI) for tumor imaging and treatment monitoring," *Curr. Med. Imaging Rev.*, vol. 8, no. 1, p. 16, 2012.
- [176] L. Curiel, R. Chopra, and K. Hynynen, "In vivo monitoring of focused ultrasound surgery using local harmonic motion.," *Ultrasound Med. Biol.*, vol. 35, no. 1, pp. 65–78, 2009.
- [177] C. Maleke and E. E. Konofagou, "In vivo feasibility of real-time monitoring of focused ultrasound surgery (FUS) using harmonic motion imaging (HMI)," *IEEE Trans. Biomed. Eng.*, vol. 57, no. 1, pp. 7–11, 2010.
- [178] Y. Han, S. Wang, T. Payen, and E. Konofagou, "Fast lesion mapping during HIFU treatment using harmonic motion imaging guided focused ultrasound (HMIGFUS) in vitro and in vivo," *Phys. Med. Biol.*, vol. 62, no. 8, pp. 3111–3123, 2017.
- [179] T. Varghese *et al.*, "Elastographic Measurement of the Area and Volume of Thermal Lesions Resulting from Radiofrequency Ablation: Pathologic Correlation," *Am. J. Roentgenol.*, vol. 181, no. 3, pp. 701–707, Sep. 2003.
- [180] Y. Le, K. Glaser, O. Rouviere, R. Ehman, and J. P. Felmlee, "Feasibility of simultaneous temperature and tissue stiffness detection by MRE," *Magn. Reson. Med.*, vol. 55, no. 3, pp. 700–705, 2006.
- [181] J. Chen, D. A. Woodrum, K. J. Glaser, M. C. Murphy, K. Gorny, and R. Ehman, "Assessment of in vivo laser ablation using MR elastography with an inertial driver," *Magn. Reson. Med.*, vol. 72, no. 1, pp. 59–67, 2014.
- [182] C. D. Anderson *et al.*, "Real-time spectroscopic assessment of thermal damage: Implications for radiofrequency ablation," *J. Gastrointest. Surg.*, vol. 8, no. 6, pp. 660–669, 2004.
- [183] C. R. Buttemere, R. S. Chari, C. D. Anderson, M. K. Washington, A. Mahadevan-Jansen, and W.-C. Lin, "In vivo assessment of thermal damage in the liver using optical spectroscopy," *J. Biomed. Opt.*, vol. 9, no. 5, p. 1018, 2004.
- [184] C. P. Hsu, M. K. Razavi, S. K. So, I. H. Parachikov, and D. A. Benaron, "Liver tumor gross margin identification and ablation monitoring during liver radiofrequency treatment," *J. Vasc. Interv. Radiol.*, vol. 16, no. 11, pp. 1473–1478, 2005.
- [185] J. W. Spliethoff, E. Tanis, D. J. Evers, B. H. W. Hendriks, W. Prevoo, and T. J. M. Ruers, "Monitoring of tumor radio frequency ablation using derivative spectroscopy," *J. Biomed. Opt.*, vol. 19, no. 9, p. 097004, 2014.
- [186] E. Tanis *et al.*, "Real-time in vivo assessment of radiofrequency ablation of human colorectal liver metastases using diffuse reflectance spectroscopy," *Eur. J. Surg. Oncol.*, vol. 42, no. 2, pp. 251–259, 2016.
- [187] E. Tanis *et al.*, "Real-time in vivo assessment of radiofrequency ablation of human colorectal liver metastases using diffuse reflectance spectroscopy," *Eur. J. Surg. Oncol.*, vol. 42, no. 2, pp. 251–259, 2016.
- [188] W. M. Whelan, S. R. H. Davidson, L. C. L. Chin, and I. A. Vitkin, "A novel strategy for monitoring laser thermal therapy based on changes in optothermal properties of heated tissues," *Int. J. Thermophys.*, vol. 26, no. 1, pp. 233–241, 2005.
- [189] L. C. Chin, B. C. Wilson, W. M. Whelan, and I. A. Vitkin, "Radiance-based monitoring of the extent of tissue coagulation during laser interstitial thermal therapy," vol. 29, no. 9, pp. 959–961, 2004.

- [190] L. C. L. Chin, W. M. Whelan, and I. A. Vitkin, "Models and measurements of light intensity changes during laser interstitial thermal therapy: implications for optical monitoring of the coagulation boundary location.," *Phys. Med. Biol.*, vol. 48, no. 4, pp. 543–59, 2003.
- [191] L. C. Chin, W. M. Whelan, M. D. Sherar, and I. a Vitkin, "Changes in relative light fluence measured during laser heating: implications for optical monitoring and modelling of interstitial laser photocoagulation.," *Phys. Med. Biol.*, vol. 46, no. 9, pp. 2407–20, 2001.
- [192] S. E. Eggener, A. Yousuf, S. Watson, S. Wang, and A. Oto, "Phase II Evaluation of MRI-Guided Focal Laser Ablation of Prostate Cancer," *J. Urol.*, vol. 196, no. 6, pp. 1670–1675, 2016.
- [193] U. Lindner *et al.*, "Image guided photothermal focal therapy for localized prostate cancer: phase I trial.," *J. Urol.*, vol. 182, no. 4, pp. 1371–1377, 2009.
- [194] S. L. Jacques, M. Motamedi, and S. Rastegar, "Computer simulation of laser coagulation of prostate: a guide to dosimetry," *Lasers Surg. Med.*, vol. 5, p. 64, 1993.
- [195] M. G. Skinner, S. Everts, A. D. Reid, I. A. Vitkin, L. Lilge, and M. D. Sherar, "Changes in optical properties of ex vivo rat prostate due to heating," *Phys. Med. Biol.*, vol. 45, pp. 1375–1386, 2000.
- [196] C. Raulin and S. Karsai, "Laser and IPL technology in dermatology and aesthetic medicine," *Laser IPL Technol. Dermatology Aesthetic Med.*, pp. 1–419, 2011.
- [197] S. C. Jiang and X. X. Zhang, "Dynamic modeling of photothermal interactions for laser-induced interstitial thermotherapy : parameter sensitivity analysis," *Lasers Med. Sci.*, vol. 20, pp. 122–131, 2005.
- [198] A. Roggan, H. J. Albrecht, K. Doerschel, O. Minet, and G. J. Mueller, "Experimental setup and Monte-Carlo model for the determination of optical tissue properties in the wavelength range 330-1100nm," in *Proc. SPIE 2323*, 1995, vol. 2323, pp. 21–36.
- [199] W. H. Nau, R. J. Roselli, and D. F. Milam, "Measurement of thermal effects on the optical properties of prostate tissue at wavelengths of 1,064 and 633\,nm," *Lasers Surg. Med.*, vol. 24, pp. 38–47, 1999.
- [200] W. M. Whelan, S. R. H. Davidson, L. C. L. Chin, and I. a. Vitkin, "A Novel Strategy For Monitoring Laser Thermal Therapy Based on Changes in Optothermal Properties of Heated Tissues," *Int. J. Thermophys.*, vol. 26, no. 1, pp. 233–241, 2005.
- [201] R. D. Peters *et al.*, "Magnetic resonance thermometry for predicting thermal damage: An application of interstitial laser coagulation in an in vivo canine prostate model," *Magn. Reson. Med.*, vol. 44, no. 6, pp. 873–883, 2000.
- [202] R. J. Stafford *et al.*, "Magnetic resonance guided, focal laser induced interstitial thermal therapy in a canine prostate model," *J. Urol.*, vol. 184, no. 4, pp. 1514–1520, 2010.
- [203] S. A. van Nimwegen, H. F. L'Eplattenier, A. I. Rem, J. J. van der Lugt, and J. Kirpensteijn, "Nd:YAG surgical laser effects in canine prostate tissue: temperature and damage distribution.," *Phys. Med. Biol.*, vol. 54, no. 1, pp. 29–44, 2009.
- [204] M. Seitz *et al.*, "High-power diode laser at 980 nm for the treatment of benign prostatic hyperplasia: Ex vivo investigations on porcine kidneys and human cadaver prostates," *Lasers Med. Sci.*, vol. 24, no. 2, pp. 172–178, 2009.
- [205] S. Natarajan *et al.*, "Focal Laser Ablation of Prostate Cancer: Feasibility of Magnetic Resonance Imaging-Ultrasound Fusion for Guidance," *J. Urol.*, vol. 198, no. 4, pp. 839–847, 2017.
- [206] S. Jaywant *et al.*, "Temperature-dependent changes in the optical absorption and scattering spectra of tissues: correlation with ultrastructure," in *Laser-Tissue Interaction IV*, 1993, vol. 1882, pp. 218–229.
- [207] W. H. Nau, R. J. Roselli, and D. F. Milam, "Measurement of thermal effects on the optical properties of prostate tissue at wavelengths of 1,064 and 633 nm," *Lasers Surg. Med.*, vol. 24, no. 1, pp. 38–



- 47, 1999.
- [208] M. Nikfarjam, C. Malcontenti-Wilson, and C. Christophi, "Comparison of 980- and 1064-nm Wavelengths for Interstitial Laser Thermotherapy of the Liver," *Photomed. Laser Surg.*, vol. 23, no. 3, pp. 284–288, 2005.
- [209] A. H. Negussie *et al.*, "Thermochromic tissue-mimicking phantom for optimisation of thermal tumour ablation.," *Int. J. Hyperthermia*, vol. 32, no. 3, pp. 239–243, 2016.
- [210] Z. Bu-Lin, H. Bing, K. Sheng-Li, Y. Huang, W. Rong, and L. Jia, "A polyacrylamide gel phantom for radiofrequency ablation.," *Int. J. Hyperthermia*, vol. 24, no. 7, pp. 568–576, 2008.
- [211] M. McDonald, S. Lochhead, R. Chopra, and M. J. Bronskill, "Multi-modality tissue-mimicking phantom for thermal therapy.," *Phys. Med. Biol.*, vol. 49, no. 13, pp. 2767–2778, 2004.
- [212] L. S. Bouchard and M. J. Bronskill, "Magnetic resonance imaging of thermal coagulation effects in a phantom for calibrating thermal therapy devices.," *Med. Phys.*, vol. 27, no. 5, pp. 1141–1145, 2000.
- [213] B. P. Hills, S. F. Takacs, and P. S. Belton, "The effects of proteins on the proton N.M.R. transverse relaxation time of water II. Protein aggregation," *Mol. Phys.*, vol. 67, no. 4, pp. 919–937, 1989.
- [214] M. N. Iizuka, M. D. Sherar, and I. A. Vitkin, "Optical phantom materials for near infrared laser photocoagulation studies," *Lasers Surg. Med.*, vol. 25, no. 2, pp. 159–169, 1999.
- [215] J. Takada, N. Honda, H. Hazama, and K. Awazu, "Ex vivo evaluation of safety and efficacy of vaporization of the prostate using a 300 W high-power laser diode with the wavelength of 980 nm," *Laser Ther.*, vol. 23, no. 3, pp. 165–172, 2014.
- [216] S. T. Flock, S. L. Jacques, B. C. Wilson, W. M. Star, and M. J. C. Van Gemert, "Optical properties of intralipid: A phantom medium for light propagation studies," *Lasers Surg. Med.*, vol. 12, no. 5, pp. 510–519, 1992.
- [217] H. J. van Staveren, C. J. M. Moes, J. van Marie, S. A. Prahl, and M. J. C. van Gemert, "Light scattering in Intralipid-10% in the wavelength range of 400–1100 nm," *Appl. Opt.*, vol. 30, no. 31, pp. 4507–4514, 1991.
- [218] A. J. Welch, M. J. C. van Gemert, and M. J. C. Van Gemert, *Optical-thermal response of laser-irradiated tissue*, vol. 2. New York: Springer, 2011.
- [219] A. Shrake and P. D. Ross, "Origins and consequences of ligand-induced multiphasic thermal protein denaturation," *Biopolymers*, vol. 32, no. 8, pp. 925–940, 1992.
- [220] N. Ahmad and M. A. Qasim, "Fatty Acid Binding to Bovine Serum Albumin Prevents Formation of Intermediate During Denaturation," *Eur. J. Biochem.*, vol. 227, no. 1–2, pp. 563–565, 1995.
- [221] R. Cubeddu, A. Pifferi, P. Taroni, A. Torricelli, and G. Valentini, "A solid tissue phantom for photon migration studies," *Phys. Med. Biol.*, vol. 42, pp. 1971–1979, 1997.
- [222] P. Di Ninni, F. Martelli, and G. Zaccanti, "Effect of dependent scattering on the optical properties of Intralipid tissue phantoms," *Biomed. Opt. Express*, vol. 2, no. 8, pp. 2265–2278, 2011.
- [223] D. D. Royston, R. S. Poston, and S. A. Prahl, "Optical Properties of Scattering and Absorbing Materials Used in the Development of Optical Phantoms at 1064nm," *Biomed. Opt. Express*, vol. 1, no. 1, pp. 110–116, 1996.
- [224] S. A. Prahl, "Everything I think you should know about inverse adding-doubling," *Oregon Med. Laser Center, St. Vincent Hosp.*, no. March, pp. 1–74, 2011.
- [225] R. Geoghegan *et al.*, "Determining Optimal Exposure Duration for Focal Laser Ablation of the Prostate," in *Proceedings of the 31st Annual Meeting of the Engineering & Urology Society*, 2016.
- [226] S. C. Jiang and X. X. Zhang, "Effects of dynamic changes of tissue properties during laser-induced interstitial thermotherapy (LITT)," *Lasers Med. Sci.*, vol. 19, no. 4, pp. 197–202, 2005.
- [227] A. Dabbagh, B. J. J. Abdullah, N. H. A. Kasim, and C. Ramasindarum, "Reusable heat-sensitive

- phantom for precise estimation of thermal profile in hyperthermia application," *Int. J. Hyperth.*, vol. 30, no. 1, pp. 66–74, 2014.
- [228] R. J. McNichols, A. Gowda, M. Kangasniemi, J. a. Bankson, R. E. Price, and J. D. Hazle, "MR Thermometry-Based Feedback Control of Laser Interstitial Thermal Therapy at 980 nm," *Lasers Surg. Med.*, vol. 34, no. October 2003, pp. 48–55, 2004.
- [229] S. E. Eggener, A. Yousuf, S. Watson, S. Wang, and A. Oto, "Phase II Evaluation of Magnetic Resonance Imaging Guided Focal Laser Ablation of Prostate Cancer," *J. Urol.*, no. September, pp. 3–8, 2016.
- [230] L. C. L. Chin, W. M. Whelan, and I. A. Vitkin, "Models and measurements of light intensity changes during laser interstitial thermal therapy: implications for optical monitoring of the coagulation boundary location.," *Phys. Med. Biol.*, vol. 48, no. 4, pp. 543–59, 2003.
- [231] T. Wu, J. P. Felmlee, J. F. Greenleaf, S. J. Riederer, and R. L. Ehman, "Assessment of Thermal Tissue Ablation With MR Elastography," *Magn. Reson. Med.*, vol. 45, no. 1, pp. 80–87, 2001.